UC Irvine
UC Irvine Electronic Theses and Dissertations

Title

Computational and Image Analysis Techniques for Quantitative Evaluation of Striated Muscle Tissue Architecture

Permalink

https://escholarship.org/uc/item/8x5538b1

Author

Morris, Tessa Altair

Publication Date

2021

Copyright Information

Peer reviewed|Thesis/dissertation

UNIVERSITY OF CALIFORNIA,
IRVINE

Computational and Image Analysis Techniques for Quantitative Evaluation of Striated
Muscle Tissue Architecture

DISSERTATION

submitted in partial satisfaction of the requirements
for the degree of

DOCTOR OF PHILOSOPHY

in Mathematical, Computational, and Systems Biology

by

Tessa Altair Morris

Dissertation Committee:
Associate Professor Anna Grosberg, Chair
Professor Elliot Botvinick
Professor Charless Fowlkes

2021

TABLE OF CONTENTS

LIST OF FIGURES

LIST OF TABLES

ACKNOWLEDGMENTS

First, I would like to thank my adviser, Prof. Anna Grosberg, for her support and mentorship throughout my PhD.

I would like to acknowledge the current and past members of my lab that gathered the experimental data used in this work. I would especially like to thank Jasmine Naik, Richard Tran, and Mehrsa Mehrabi for their experimental and intellectual contributions to this work.

I would also like to thank my colleagues and collaborators at UCI, Qingda Hu, Alvaro Fletcher, and Navied Akhtar for their enthusiasm and creativity.

I would like to extend a thank you to the MCSB, CCBS, and CMCF leadership and administrative staff for all of their support throughout graduate school.

I would like to thank the entire MCSB community, especially the founders and organizers of the Biophysics and Systems Biology Seminar Series - Prof. Jun Allard, Kerrigan Blake, Matt Bovyn, Nick Pervolarakis, and Sohyeon Park - for both their support and their candor.

Thank you to my colleagues and collaborators at institutions outside UCI, Anicca Harriot and Prof. Chris Ward at the University of Maryland, as well as Avraham Moriel, Prof. Eran Bouchbinder, and Prof. Samuel Safran from the Weizmann Institute of Science, Israel.

I would also like to give special thanks to my committee members, Prof. Elliot Botvinick and Prof. Charless Fowlkes, and my advancement committee members, Prof. Timothy Downing, Prof. Edwin Monuki, and Prof. Wendy Liu for their time and consideration.

I would like to acknowledge the publishers of PLoS Computational Biology. The text and figures of Chapter 2 is a reprint of the material as it appears in PLoS Computational Biology.

VITA

Tessa Altair Morris

EDUCATION

Ph.D., Mathematical, Computational, and Systems Biology **2021**
University of California, Irvine *Irvine, California*
B.S., Biomathematics **2016**
Loyola Marymount University *Los Angeles, California*

RESEARCH EXPERIENCE

Graduate Student Researcher **2017 - 2021**
University of California, Irvine *Irvine, California*
Mathematical and Computational Biology Trainee **2016 - 2017**
University of California, Irvine *Irvine, California*
Undergraduate Researcher **2015-2016**
Loyola Marymount University *Los Angeles, California*
Research Assistant **2014**
University of California, San Diego *San Diego, California*

TEACHING EXPERIENCE

Teaching Assistant, Biotransport Phenomena **2021**
University of California, Irvine *Irvine, California*
Teaching Assistant, Engineering Analysis/Design: Data Analysis **2020**
University of California, Irvine *Irvine, California*
Instructor, Complex Data Preparation & LaTeX **2019**
University of California, Irvine *Irvine, California*
Teaching Assistant, Fitting Models to Data **2019**
University of California, Irvine *Irvine, California*
Instructor, Introduction to Programming Using Matlab **2019**
University of California, Irvine *Irvine, California*
Teaching Assistant, Physical Chemistry Laboratory **2015**
Loyola Marymount University *Los Angeles, California*
Teaching Assistant, General Chemistry Laboratory **2014**
Loyola Marymount University *Los Angeles, California*

PUBLICATIONS

1. **Morris TA**, Naik J, Fibben KS, Kong X, Kiyono T, Yokomori K, Grosberg A (2020). Striated myocyte structural integrity: automated analysis of sarcomeric z-discs. *PLOS Computational Biology.*

2. **Morris TA**, Tran RDH, Grosberg A. A Comprehensive Review of Computational and Image Analysis Techniques for Quantitative Evaluation of Striated Muscle Tissue Architecture. *Submitted 2021.*

3. Mehrabi M, **Morris TA**, Cang Z, Nguyen CHH, Sha Y, Asad MN, Khachikyan N, Greene TL, Becker DM, Nie Q, Zaragoza MV, Grosberg A. *In Vitro* Modeling of Variable Heart Diseases due to LMNA Mutation via Patient iPSC-derived Cardiomyocytes. *Submitted 2021.*

4. Hu Q, **Morris TA**, Grosberg A, Levine AJ, Botvinick EL (2021). Actively driven fluctuations in a fibrin network. *Frontiers in Physics.*

5. Oh A, **Morris TA**, Yoshii IT, Morris TA (2017). Flow Decay: A Novel Spirometric Index to Quantify Dynamic Airway Resistance. *Respiratory Care.*

ARTICLES IN PREPARATION

1. Tran RDH*, **Morris TA***, Grosberg A. Quantitative Evaluation of Cardiac Cell Interactions and Responses to Cyclic Strain.

2. Harriot A*, **Morris TA***, Grosberg A, Ward CW. An Experimental and Computational Framework for Profiling Myofibrillar Deformations in Skeletal Muscle.

ABSTRACT OF THE DISSERTATION

Computational and Image Analysis Techniques for Quantitative Evaluation of Striated
Muscle Tissue Architecture

By

Tessa Altair Morris

Doctor of Philosophy in Mathematical, Computational, and Systems Biology

University of California, Irvine, 2021

Associate Professor Anna Grosberg, Chair

Quantitative evaluation of cellular morphology is crucial to understanding development and
pathology of striated muscle tissues, including skeletal and cardiac myocytes. Striated my-
ocytes are composed of parallel myofibrils, which are spanned by repeating sarcomere units
that produce a contractile force parallel to the thick myosin filaments as they slide past the
thin actin filaments. As sarcomeres produce the force necessary for contraction, assessment
of sarcomere order is paramount in characterization of cardiac and skeletal myocytes. The
uniaxial force produced by sarcomeres is ideally perpendicular to their z-lines, which couple
parallel myofibrils and give cardiac and skeletal myocytes their distinct striated appearance.
Accordingly, sarcomere structure is often evaluated by staining for z-line proteins such as
α-actinin and titin, as well as actin. Despite their importance, challenges such as isolating
z-lines from regions of off-target staining that occur along immature stress fibers and cell
boundaries, a lack of metrics that summarize important and relevant aspects of sarcom-
eric architecture, and quantitatively studying striated myocytes in the presence of other cell
types, have gone largely unaddressed. While an expert can qualitatively appraise tissues,
these challenges leave researchers without robust, repeatable tools to assess striated myocyte
morphology and behavior across different labs and experiments. Furthermore, the criteria
used by experts to evaluate sarcomeric architecture have not been well-defined. We address

these challenges by developing image processing pipelines to isolate structures of interest and providing metrics that summarize distinct aspects of cellular architecture in multiple different striated muscle tissues, imaged with various modalities. Characterization of striated myocyte morphology using the metrics discussed and implemented in this work can quantitatively evaluate striated muscle tissues and contribute to a robust understanding of the development and mechanics of striated muscles.

CHAPTER 1

Introduction

Quantification of cellular morphology and structure from images is fundamental to the study of tissues, especially striated muscles. It has been used to characterize the developmental stage[2–4], engineered tissues[5–9], effects of disease[10–13] or injury[14–17], and treatment with pharmacological agents[18] as well as to predict reduction in contractile function[19–21]. This is in large part due to the unique link between structure and function in striated myocytes, as their ability to contract is dependent on the nearly crystalline order of its cytoskeletal components[22,23]. While many of the hypotheses about the aspects of striated myocytes morphology that impact function may come from qualitative assessment of images, it is essential to use quantitative techniques to ensure reproducibility and reliability across labs. In this chapter, we present an overview of different metrics and software for quantitative assessment of striated myocytes from images and their impact in order to facilitate future striated myocyte biology research.

1.1   Striated Myocyte Cellular Morphology

Muscle tissue function is reliant on organization that spans multiple spatial-scales[23], and connecting and choosing which scale to focus on presents its own challenges. In evaluating pathology of the heart or efficacy of stem-cell derived cells, it can be useful to measure aspects of gross cell geometry such as area, volume, and aspect ratio[24–27]. For example, in the ventricular myocardium, cellular aspect ratio is tightly regulated (approximately 7:1)[28–30], but increases[29,30] or decreases[31,32] in some types of heart disease. Additionally, in cell culture experiments, Kuo et al.[27] established both a correlation between contractility and cardiomy-

ocyte aspect ratio, as well as between cardiomyocyte aspect ratio and changes to cytoskeletal architecture. However, evaluating only cell or tissue scale architecture is insufficient to fully characterize striated muscle tissues.

1.2 Striated Myocyte Cytoskeleton Architecture

Organization of the striated myocyte cytoskeleton is integral to the efficiency of force production[20,33,34]. Striated myocytes are composed of parallel myofibrils, which are spanned by repeating sarcomere units that produce a contractile force parallel to the thick myosin filaments as they slide past the thin actin filaments[35,36]. The uniaxial force generated by muscle tissues is maximized when all sarcomeres within a cell are aligned and all cells in a tissue are aligned[23]. Consequently, myofilament disorganization has been shown to have a critical role in contractile impairment[37,38]. Furthermore, the organization of myofibrils and their sarcomeres may guide the position, shape, or organization of other organelles, in particular the mitochondria and nuclei[39–41]. Organizational guidance and changes to morphology caused by the cytoskeleton may impact gene expression and have other downstream functional consequences[42–45]. In order to address the need to evaluate cytoskeletal architecture, many metrics and image processing tools have been developed.

1.2.1 Metrics to Evaluate Cytoskeleton Architecture: Organization

Quantifying organization of cytoskeletal proteins such as actin and sarcomeric α-actinin is an extremely useful tool for characterization of striated muscle. One popular metric for measuring global construct organization is the orientational order parameter (OOP)[19,20,46–51]. Using the OOP to summarize both the sarcomeric α-actinin and actin organization has shown a

positive and predictive relationship between cytoskeletal alignment and contractile stresses in engineered cardiac tissues[19,20]. The OOP of sarcomeric α-actinin has also been used to phenotype stem cell derived cardiomyocytes, and compare them with primary cardiomyocytes[4,7]. Local organization has been measured by quantifying the OOP of a construct at shorter length scales[9], the correlation between the orientation of cellular constructs relative to other components[6], and by the Sarcomere Organization Score developed by Sutcliffe et al.[24]. Both experimentally and theoretically, cytoskeletal organization has been shown to impact contraction[19,20], underscoring the importance of quantifying this property of striated myocyte architecture. One important caveat to these metrics is that they require accurate segmentation of the construct of interest in order to accurately capture the organization of that construct.

1.2.2 Metrics to Evaluate Cytoskeleton Architecture: Sarcomere Length

Another important characteristic of striated myocytes is the sarcomere length[52,53], which increases during myofibril development[54]. Accordingly, it has been commonly used to characterize the immaturity of stem-cell derived cardiomyocytes, which have shorter sarcomere lengths than that of primary cardiomyocytes[4]. Because measuring the sarcomere length cannot be done efficiently by hand, multiple pieces of software have been developed to measures sarcomere length in images, many of which use it to characterize contractile function[1,4,17,55]. Due to the morphological changes of striated myocytes during development, the sarcomere length is an essential metric that should be included in analysis pipelines. However, depending on the pathology or maturity of the tissue, it may be necessary to measure more subtle changes in sarcomere architecture.

1.2.3 Metrics to Evaluate Cytoskeleton Architecture: Sarcomere Registration and Continuity

A metric that may capture more subtle differences between striated myocytes is that lateral alignment of sarcomeric z-lines in neighboring myofibrils (i.e. z-line registration) has also been considered an important metric to assess striated myocytes[21,27,38,56–61]. When the sarcomere are well organized with the same sarcomere length, it has been hypothesized that sarcomeric z-line registration influences contractile function and is an important characteristic of well-formed myofibrils[21,27,56–61]. This hypothesis has been supported by the observation of a disruption in z-line registration between adjacent myofibrils in the ventricles of failing hearts[38]. The significance of z-line registration has been investigated using both theoretical and experimental approaches[21,27,56–60,62], which often required measuring z-line registration in images of striated muscle. Using an experimentally observable metric - the length over which z-lines of neighboring myofibrils are registered - to approximate z-line registration, a correlation between high z-line registration and coherent, strong contractions was demonstrated in single cells[27,58–60]. However, further investigation into z-line registration has been hindered by the reliance on experts to manually or semi-manually measure the registration length in images.

1.3 Nuclear Morphology

The striated myocyte nucleus is mechanically connected to the cell membrane through the cytoskeleton, which has been shown to influence nuclear morphology[42–45]. Because changes in nuclear morphology are often accompanied by altered function, fully understanding the functional and genomic consequences of striated myocytes in pathology, aging, or in response to stimuli, requires recognizing changes to nuclear morphology[42,45,63,64]. As the characteriza-

tion of nuclear morphology is important part of many biological fields, there is an abundance of software designed to segment nuclei in images using a large variety of image processing and deep learning approaches[65,65,66,66–70,70–82]. Once nuclei have been segmented, there is also a need for robust, quantitative metrics to compare and classify their morphology as normal or containing defects[69,79]. One important challenge is that segmentation tools in biology generally yield nontrivial amounts of segmentation error due to assumptions in the computational design and variability in biological phenotypes[66]. Another important challenge is selecting the correct metrics to characterize the nuclei, including geometry as well as relative location both of which are important to tissue function. Mouse models of muscle laminopathies showed nuclear migration during skeletal muscle maturation that correlated with disease severity[83]. Regarding the nuclear geometry, there is evidence of changes in size and eccentricity, as well as the presence of nuclear blebs or invaginations in pathological conditions such as cardiomyopathies and laminopathies[84–89]. However, defining which geometric properties should be used to characterize striated myocyte nuclei, requires further investigation into the mechanisms by which their morphology impacts their function, as well as understanding these mechanisms in the context of changes to the cytoskeleton[42,90,91].

1.4 Muscle Tissue with Multiple Cell-Types

Studying interactions between morphologically or phenotypically distinct cells is a vital aspect of understanding biological processes[92], such as the role of smooth and skeletal muscle in esophageal function[93], the cardiac remodeling response of cardiomyocytes and cardiac fibroblasts[94–96], and the variability in the cell types and functionality produced from cardiac differentiation from induced pluripotent stem cells[7,24,97]. Therefore, in order to study interactions or differences between morphologically distinct cells, it is necessary to accurately and reliably separate them in images, which can be extremely challenging to do by hand in a high-throughput manner, particularly in confluent tissues. To combat this issue,

image-based cell profiling commonly makes use of machine learning classifiers and feature extraction, as well as deep learning approaches[75,77,92,98–105]. Once the cell type or cell state segmentation has been achieved it can be combined with other analysis to unlock even more biological information, including studying interactions between different cells[26]. However, it is extremely difficult to create a classifier that can correctly account for the large spread of biological and experimental variability, especially while considering the unique morphology of striated myocytes.

1.5   Conclusion

In this chapter, we presented an overview of image processing and analysis techniques for assessment of striated myocytes. The unique nature of these cells necessitates the use of advanced image analysis techniques. While there have been many advances in computer vision and biological image analysis[106], many tools are not suitable to use on striated myocytes without further modification. The specialized pipelines designed for striated myocytes have yielded great insight into the structure-function relationship and changes during pathology. As this chapter demonstrates, widespread adaptation and additional development of these computational techniques will enable further advances in the field of striated myocyte morphology.

1.6   Thesis Introduction

In this dissertation, we present our contribution to quantitative evaluation of striated muscle, through establishing image processing pipelines to segment structures in striated myocytes and developing metrics to summarize aspects of their architecture and morphology. In Chapter 2 (Morris et al.[107]), we discuss development of novel metrics to characterize the z-lines of

striated myocytes, the z-line fraction and the z-line length. We present extensions of these and other metrics to skeletal myofibers in Chapter 3 and to immature, multilayer cardiac tissues in Chapter 4. Additionally, in Chapter 5 we provide a framework for quantifying the organization of distinct cardiac cell types that are present in the same images.

CHAPTER 2

Striated myocyte structural integrity: Automated analysis of sarcomeric z-discs[1]

2.1   Abstract

As sarcomeres produce the force necessary for contraction, assessment of sarcomere order is paramount in evaluation of cardiac and skeletal myocytes. The uniaxial force produced by sarcomeres is ideally perpendicular to their z-lines, which couple parallel myofibrils and give cardiac and skeletal myocytes their distinct striated appearance. Accordingly, sarcomere structure is often evaluated by staining for z-line proteins such as α-actinin. However, due to limitations of current analysis methods, which require manual or semi-manual handling of images, the mechanism by which sarcomere and by extension z-line architecture can impact contraction and which characteristics of z-line architecture should be used to assess striated myocytes has not been fully explored. Challenges such as isolating z-lines from regions of off-target staining that occur along immature stress fibers and cell boundaries and choosing metrics to summarize overall z-line architecture have gone largely unaddressed in previous work. While an expert can qualitatively appraise tissues, these challenges leave researchers without robust, repeatable tools to assess z-line architecture across different labs and experiments. Additionally, the criteria used by experts to evaluate sarcomeric architecture have not been well-defined. We address these challenges by providing metrics that summarize different aspects of z-line architecture that correspond to expert tissue quality assessment and demonstrate their efficacy through an examination of engineered tissues and single cells. In

---

[1]Morris, Tessa Altair, et al. (2020) *PLoS Computational Biology*

doing so, we have elucidated a mechanism by which highly elongated cardiomyocytes become inefficient at producing force. Unlike previous manual or semi-manual methods, characterization of z-line architecture using the metrics discussed and implemented in this work can quantitatively evaluate engineered tissues and contribute to a robust understanding of the development and mechanics of striated muscles.

2.2 Author summary

Structural evaluation of sarcomeres is fundamental to the study of striated muscle. However, due to limitations of current analysis methods, the mechanisms by which sarcomere order can impact contraction and the characteristics of sarcomere architecture that should be used to assess striated myocytes have not been fully explored. Furthermore, it is not clear what aspects of sarcomere architecture are considered by the experts when qualitatively evaluating striated muscle tissues. Therefore, we developed a computational structural assay in MAT-LAB, `ZlineDetection`, to evaluate sarcomere architecture by both extracting sarcomeric z-lines from images and providing metrics that encapsulate different aspects of z-line architecture that an expert would evaluate when judging the quality of the tissue. The sarcomere structure of both patient-specific skeletal muscle and rat cardiomyocytes were evaluated with differences among engineered cells and tissues quantified using novel and established metrics. As a result, a mechanism by which highly elongated cardiomyocytes become inefficient at producing force was elucidated. `ZlineDetection` identifies and quantifies the characteristics used by experts for evaluation and thus it will lead to more rigorous differentiation methods and tissue comparison across labs and contribute a robust understanding of how structure affects mechanical function.

2.3   Introduction

Assessment of cellular morphology and structure is fundamental to the study of striated muscles. It has been used to characterize the developmental stage[2–4], engineered tissues[5–9], effects of disease[10–13] or injury[14–17], and treatment with pharmacological agents[18] as well as used to predict function[19–21]. Indeed, the ability of striated muscle cells to contract is dependent on the nearly crystalline order of its cytoskeletal components[22,23], which makes evaluation of structure paramount. Skeletal and cardiac myocytes are composed of parallel myofibrils, which are spanned by repeating sarcomere units that produce a contractile force parallel to the thick myosin filaments as they slide past the thin actin filaments[35,36]. Consequently, myofilament disorganization has been shown to have a critical role in contractile impairment[37,38]. The uniaxial force produced by sarcomeres is ideally perpendicular to their z-lines, which couple parallel myofibrils and give cardiac and skeletal myocytes their distinct striated appearance[108]. Accordingly, sarcomere structure is often evaluated by staining for z-line proteins such as α-actinin[2,6–9,19–21,27,35,36,46,54,59,60,109–111]. A disruption in alignment or registration of z-lines across neighboring myofibrils has been observed in the ventricles of failing hearts[38]. However, the mechanism by which sarcomere and by extension z-line architecture can impact contraction and which characteristics of z-line architecture should be used to assess striated myocytes has not been fully explored.

Certain aspects of z-line architecture quantifiable from flourescently stained images have been used to evaluate engineered tissues and to predict function. In particular, because the uniaxial force of sarcomeres is maximized when they are all oriented in the same direction, the orientational order of the z-line protein α-actinin has been used extensively as a metric[4,7,19,46,112]. Similarly, the correlation between the orientational order of z-lines and actin fibrils is also an important metric because the relative orientation of these structures transitions from parallel to perpendicular during development[6,9,113,114]. The relative location

and lateral alignment of z-lines in neighboring myofibrils is also hypothesized to influence contractile function and to be an important metric to assess myofibril formation[21,27,56–61]. In particular, theoretical models have been established to explain why z-lines of neighboring myofibrils tend to register during development[57] and the impact of z-line registration on contractile function[21,56]. While theoretical models and experiments have provided insight into which facets of z-line architecture are important to characterize striated myocytes, research has been hindered due to limitations of current analysis methods to quantify z-line architecture, which require manual or semi-manual handling of images[4,6,7,9,19–21,27,36,46,58–60].

Quantification of z-line architecture involves accurately extracting z-lines from an image. Although researchers experienced with striated myocytes have the skill to manually trace and extract z-lines, it is a low throughput method and highly susceptible to variability between observers. Previous work has utilized techniques from the field of image analysis such as topology-preserving thinning and edge detection to extract features, such as z-lines, from an image[115–117]. However, these methods have not been optimized for striated myocytes because they include regions of off-target staining, which would be ignored by an expert tracing the z-lines. Once the z-lines have been automatically or manually identified in an image, there is an additional challenge of choosing metrics to summarize overall z-line architecture[4,6]. Although experts can qualitatively score tissue quality, it is ambiguous which aspects of sarcomere architecture are being considered and why those elements are important. Auxiliary hurdles include biological variability, as well as variability in staining and image quality. These challenges have gone largely unaddressed in previous work, which leave researchers without robust, repeatable tools to assess z-line architecture.

In this work, we investigated which aspects of sarcomere architecture experts use to evaluate the quality of striated tissue, including those implicated in existing theoretical models of muscle fiber contraction. To do this, we developed `ZlineDetection` in MATLAB, the first fully automatic computational protocol to both isolate z-lines and characterize z-line archi-

11

tecture. Isolating z-lines involved constructing a biologically motivated approach to segment (i.e. remove) off-target staining without the need for user input. Along with reporting existing metrics such as z-line orientational order, `ZlineDetection` was used to calculate the fraction of α-actinin staining that composes well-formed z-lines and find the location and length of z-lines of neighboring myofibrils that are both registered and continuous. Additionally, analysis of isolated cardiomyocytes with variable aspect ratios were compared with published results[27]. Finally, `ZlineDetection` was used to differentiate among tissues engineered to be anisotropically or isotropically organized, but well-formed, and those engineered to be malformed. By building on previous image analysis methods and establishing new metrics, `ZlineDetection` automatically and quantitatively assesses sarcomere architecture, and can be used by researchers imaging z-lines with fluorescent staining.

2.4   Materials and methods

2.4.1   Ethics Statement

All animals were treated according to the Institutional Animal Care and Use Committee of UCI guidelines (IACUC Protocol No. 2013-3093). It also followed recommendations of the NIH Guide for the Care and Use of Laboratory Animals and was in accordance with existing federal (9 CFR Parts 1, 2, & 3), state, and city laws and regulations governing the use of animals in research and teaching. The adult Sprague-Dawley rat was euthanized by CO_2 inhalation followed by cervical dislocation at a ULAR facility. Dam's euthanasia was done prior to pup sacrifice in order to minimize the stress the dams experience when their pups are taken. The rat pups were then immediately taken to our core lab where each 2 day old neonatal rat pup was euthanized by decapitation. This euthanasia method adheres to the current most humane standards, which maintain scientific validity of the cell cultures as stated in the "AVMA Guidelines for the Euthanasia of Animals: 2013 Edition" (published

by the American Veterinary Medical Association).

2.4.2 Substrate Preparation and Extracellular Matrix Patterning

Substrates were fabricated for structural studies as described previously[6,9,20,36,69]. Briefly, large cover glass (Brain Research Laboratories, Newton, MA) was cleaned by sonicating, then spin coated with 10:1 Polydimethylsiloxane (PDMS; Ellsworth Adhesives, Germantown, WI). The PDMS coated cover glass was then placed in a 60°C oven to cure overnight (12 h). The cover glass was then cut into smaller individual coverslips to fit in a 12 well plate. Fibronectin (FN; Fischer Scientific Company, Hanover Park, IL) was patterned onto the coverslips in lines 20 µm wide with 5 µm gaps or islands of various aspect ratios using microcontact printing[118]. The PDMS stamps were then sonicated in ethanol and coated with 0.1 mg/mL drops of FN. After being incubated for 1 h and dried using compressed nitrogen, FN was printed onto the PDMS coated coverslips that were previously exposed to UV light (Jelight Company, Irvine, CA) for 8 min. Finally, the stamped coverslips were submerged in a solution of 5 g Pluronics F-127 (Sigma Aldrich, St. Louis, MO) dissolved in 0.5 L sterile water for 5 min and then rinsed three times with room temperature phosphate-buffered saline (PBS; Life Technologies, Carlsbad, CA). Isotropic tissue samples were made by coating coverslips with a uniform layer of FN[6].

2.4.3 Cardiomyocyte Culture

Ventricular myocardium was extracted from two day old neonatal Sprague Dawly rats (Charles River Laboratories Wilmington, MA) under sterile conditions and in accordance with the guidelines of the Institutional Animal Care and Use Committee of University of California, Irvine (Protocol No. 2013-3093). Cardiomyocytes were then isolated from the ventricular myocardium as described previously[6,9,20,36]. Briefly, after rinsing the ventricular

tissue in Hanks' balanced salt solution buffer (HBSS; Life Technologies, Carlsbad, CA), the tissues were incubated overnight (12 h) at 4℃ in a 1 mg/mL trypsin solution (Sigma Aldrich, Inc., Saint Louis, MO) dissolved in HBSS. After neutralizing the trypsin in warmed 10% fetal bovine serum (FBS; ThermoFisher, Grand Island, NY) M199 culture media (Invitrogen, Carlsbad, CA), the tissue was washed four times with 1 mg/mL collagenase (Worthington Biochemical Corporation, Lakewood, NJ) dissolved in HBSS. Isolated cells were centrifuged at 1200 rpm for 10 min and re-suspended in chilled HBSS, before being centrifuged again at 1200 rpm for 10 min. The cells were then re-suspended in warm 10% FBS M199 culture media and purified through three consecutive preplates. Cells were then counted and seeded onto FN coated coverslips. The seeding density used to produce confluent monolayers was 1400 cells/mm^2, the density for sparse tissue was 350 cells/mm^2, and the density for isolated cardiomyocytes was 200 cells/mm^2. At 24 h post-seeding, dead cells were washed away with PBS and the remaining cells were incubated in 10% FBS M199 media. After 24 h, the 10% FBS media was replaced with 2% FBS M199 media. As described previously[109], for cells treated with 2,3-butanedione 2-monoxime (BDM; Sigma Aldrich, Inc., St. Louis, MO), the culture media containing 10 mM BDM was prepared by adding 1/500 volume 5 mol/L BDM dissolved in dimethylsulfoxide (DMSO; Sigma Aldrich, Inc., St. Louis, MO) and stored at -20℃. BDM was left to interact with cells for two days before fixing.

2.4.4 Skeletal Muscle Preparation

Human primary cultured healthy control myoblasts were immortalized using hTERT with p16^{INK4a}-resistant R24C mutant CDK4 and cyclin D1 as previously described[119]. After immortalization, CD56-positive cells were selected by magnetic-activated cell sorting conjugated with anti-CD56 antibody (130-050-401, Miltenyi Biotec). Myoblast differentiation was induced as previously described[120]. Briefly, CD56-positive cells were plated onto coverslips at a seeding density of ~2.5 x 10^5 cells/mL in 2 mL of growth medium (high glucose DMEM

(11965, Gibco) supplemented with 20% FBS (FB-02, Omega Scientific, Inc.), 1% Pen-Strep
(15140122, Gibco) and 2% Ultrasor G (67042, Crescent Chemical Co.)) in each well of a
12-well dish. Approximately 12-16 h later, differentiation was induced using high glucose
DMEM medium supplemented with 2% FBS and ITS supplement (insulin 0.1%, 0.000067%
sodium selenite, 0.055% transferrin, 51300044 Invitrogen). Fresh differentiation media was
changed every day.

2.4.5   Fixing, Immunostaining, and Imaging

After 72 h (cardiomyocytes) or 14 days (skeletal muscle) in culture, cells were fixed in warm
4% paraformaldehyde (Fisher Scientific, Hanover Park, IL) supplemented with 0.001% Triton
X-100 (Sigma-Aldrich, Inc., St. Louis, MO) in PBS for 10 min. Cells were rinsed three times
in room temperature PBS for 5 min and then stained for actin (Alex Fluor 488 Phalloidin;
Life Technologies, Carlsbad, CA), sarcomeric α-actinin (Mouse Monoclonal Anti-α-actinin;
Sigma Aldrich, Inc., St. Louis, MO), nuclei (4',6'-diaminodino-2-phenlyinodol (DAPI; Life
Technologies, Carlsbad, CA), and FN (polyclonal rabbit anti-human fibronectin; Sigma
Aldrich, Inc., St. Louis, MO). Secondary staining was applied using tetramethylrhodamine-
conjugated goat anti-mouse IgG antibodies (Alexa Fluor 633 Goat anti-mouse or Alexa Fluor
750 Goat anti-mouse; Life Technologies, Carlsbad, CA) and goat anti-rabbit IgG antibodies
(Alexa Fluor 750 goat anti-rabbit or Alexa Fluor 633 Goat anti-rabbit; Life Technologies,
Carlsbad, CA) for a 1-2 h incubation. The coverslips containing the immunostained cells
were then mounted onto a microscope slide preserved with prolong gold antifade reagent
(Life Technologies, Carlsbad, CA). The images were collected using an IX-83 inverted mo-
torized microscope (Olympus America, Center Valley, PA) with an UPLFLN 40x oil immer-
sion objective (Olympus America, Center Valley, PA) and a digital CCD camera ORCA-R2
C10600-10B (Hamamatsu Photonics, Shizuoka Prefecture, Japan). The resolution of the
images taken with the 40x oil objective was ~6 pixels/µm. Ten to fifteen fields of view were

randomly acquired for every sample. Raw images and other data have been deposited in the
Dryad repository: `https://doi.org/10.7280/D12Q2X`[121].

2.4.6 Statistical Analysis

To determine statistical significance, one-way analysis of variance (ANOVA) with Tukey's
Test was performed in R version 3.5.2 using RStudio Version 1.1.463. A p-value less than
0.05 was considered significant. Sample size calculations were also performed using R with
a power of 0.95.

2.4.7 Image Processing

We developed the following analysis procedure, we named `ZlineDetection`, which we made
available on Github (`https://github.com/Cardiovascular-Modeling-Laboratory/`
`zlineDetection`). `ZlineDetection` was implemented in MATLAB version 9.5.0.1033004
(R2018b) (MathWorks, Natick, MA). Parameters are listed and described in Table A.1 and
the user guide can be found in the Github repository for `ZlineDetection`.

Extraction of α-actinin Skeleton and Orientation

The z-line architecture was analyzed after extracting the binary skeleton and orientation
vectors of the z-lines in images of α-actinin stained cardiac tissue. The process of extracting
the α-actinin binary skeleton (Fig A.1) was adapted from an image analysis protocol estab-
lished for fibrillar materials in MATLAB[122]. Briefly, gray-scale images were smoothed using
coherence enhancing anisotropic diffusion filtering, which calculates the eigenvectors of the
image Hessian to direct diffusion and uses a finite difference scheme to perform the diffu-
sion, repeating until diffusion time was reached[123–125]. The diffusion time and smoothing

parameters were selected by choosing parameters that resulted in skeletons with the highest
similarity[126] to manually traced sections of cardiac tissue (Fig A.2). The parameters selected
minimized the following equation:

$$E_p = \frac{1}{n} \sum_i^n \left(S_{i,p} - S_{i,\mathrm{max}} \right)^2 . \tag{2.1}$$

In Eq 2.1, the error (E_p) for parameter set p is the squared difference between the similarity
of image i for the current parameter set ($S_{i,p}$) and the maximum similarity for image i
($S_{i,\mathrm{max}}$), divided by the number of images (n). After contrast enhancement using top hat
filtering[127], the background was removed using a surface interpolation[128] and then binarized
by adaptive thresholding. Finally, the binarized images were thinned to one pixel width and
trimmed in order to obtain the α-actinin skeleton. Local orientation was estimated from the
diffusion filtered image using a least mean square orientation estimation algorithm[129,130].

Actin Orientation Detection

The orientation of actin at each pixel was calculated as described previously[19,46]. Briefly,
images were filtered with a Gaussian kernel and then normalized to have zero mean and
unit standard deviation[130]. The orientation was then estimated using a least mean square
orientation estimation algorithm[129,130].

Actin Guided Segmentation

In order to obtain the z-line skeleton, off-target α-actinin staining was segmented by using
the local orientation of actin. Local orientation of actin was computed by breaking images
into grids and computing the structural tensor for the orientation vectors $\vec{r}(x, y)$ in each
grid. Local orientation was defined as the director in each grid, which is the eigenvector

17

corresponding to the maximum eigenvalue of tensor $\mathbb{T}$:

$$\mathbb{T} = \left\langle 2 \begin{bmatrix} r_{i,x}r_{i,x} & r_{i,x}r_{i,y} \\ r_{i,x}r_{i,y} & r_{i,y}r_{i,y} \end{bmatrix} - \begin{bmatrix} 1 & 0 \\ 0 & 1 \end{bmatrix} \right\rangle. \tag{2.2}$$

The α-actinin orientation vectors were compared to the local orientation of actin by taking
the dot product:

$$\gamma = \vec{p}_{\text{actin}} \cdot \vec{q}_{\alpha\text{-actinin}}. \tag{2.3}$$

An α-actinin pixel was considered off-target staining when γ in Eq 2.3 was greater than a
threshold, indicating $\vec{p}_{\text{actin}}$ and $\vec{q}_{\alpha\text{-actinin}}$ were too close to parallel.

Orientational Order Parameter

As described previously[36,131], the orientational order of constructs in an image was quantified
by the maximum eigenvalue of the structural tensor $\mathbb{T}$ (Eq 2.2), termed the Orientational
Order Parameter (OOP).

2.4.8   Continuous Z-line Detection

The continuous z-lines were detected in images of α-actinin stained cardiac tissue after
generation of the z-line binary skeleton and corresponding orientation vectors. We created
and implemented the following method in MATLAB to group z-line orientation vectors based
on their location and direction. Briefly, each orientation vector ($\vec{v}_i$), with the exception of
those located at the edges of the image, have eight neighboring pixels that surround it. Six
"candidate neighbors" were chosen by excluding the neighboring pixels that were positioned

in the directions perpendicular to the angle ($\pm\theta_0$) corresponding to $\vec{v}_i$. These "candidate

neighbors" were then narrowed down to two by selecting one neighbor in each direction that

had the highest dot product value, meaning that the orientation vector at that position

is the most parallel to $\vec{v}_i$. These sets of orientation vectors and their neighbors were then

iteratively grouped into continuous z-lines.

2.4.9 Nuclei Counting

The nuclei per area was computed by summing the number of nuclei across all fields of view

of a coverslip and then dividing by the total area in square millimeters.

2.5 Results

2.5.1 Automating Isolation of Z-lines

Accurately extracting z-lines from images of striated myocytes, including primary cardiomy-

ocytes (Fig 2.1Ai) and patient-specific skeletal muscles (Fig 2.1Aii), is essential to evaluating

their z-line architecture. In images of striated muscle cells stained for α-actinin, a pro-

tein within the sarcomeric z-lines (Fig 2.1A), α-actinin appears as striations approximately

perpendicular to actin fibrils (Fig 2.1A, *green*). However, in addition to the sarcomeric

z-lines (Fig 2.1Ai, *red vertical striations in region outlined in yellow*), α-actinin tends to

be present at the cell boundaries and along immature stress fibers that do not have fully

developed z-lines[3] (Fig 2.1Ai, *white outline*). In contrast to z-lines, regions of off-target α-

actinin staining are often oriented along the direction of actin (Fig 2.1A, *green*), rather than

perpendicular[6,113]. Consequently, when α-actinin images are condensed into their binary

skeletons[122,129,130] (Fig 2.1B), off-target α-actinin staining appears as long line segments ori-

ented perpendicular to the z-lines and parallel to the orientation of actin fibrils, represented
by green arrows (Fig 2.1B). Including regions of off-target α-actinin staining in quantitative evaluation of z-line architecture, in particular assessment of orientational order, causes results to be less accurate.
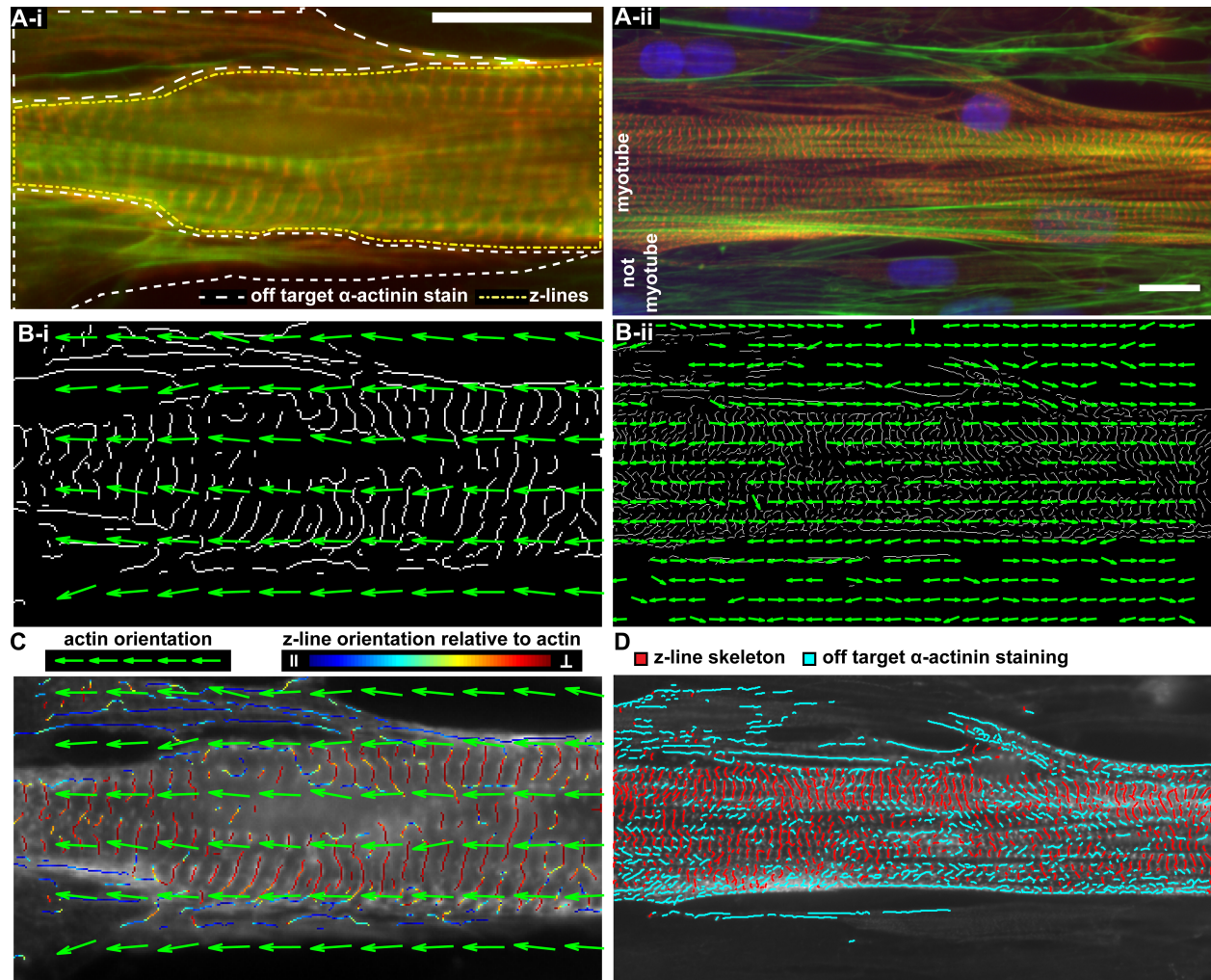
Figure 2.1: **Actin orientation guided segmentation of the α-actinin skeleton. A**,
Images of cardiac **(Ai)** and skeletal muscle **(Aii)** stained for actin fibrils (green), α-actinin
(red), and nuclei (blue). In **Ai**, off-target α-actinin stain is outlined in white and the region
containing z-lines is outlined with a yellow dashed-dotted line. **B**, The orientation of the
actin fibrils in **(A)**, represented by green arrows, plotted on top of the α-actinin skeleton.
C, Actin orientation vectors (green) overlaid on α-actinin stained cardiac tissue **(Ai)** where
each pixel in the α-actinin binary skeleton **(Bi)** is colored according to its orientation relative
to local actin orientation from parallel (dark blue) to perpendicular (red) as indicated by
the colorbar. **D**, Skeletal muscle shown in **Aii** with off-target α-actinin staining (blue) and
z-lines (red). Scale bars: 15 μm.

While image processing procedures such as anisotropic diffusion filtering provided a solution to remove imaging noise[122,123], it was not capable of excluding off-target α-actinin staining. However, it is possible to classify α-actinin positive pixels as either off-target staining or z-lines according to their orientation relative to their local actin fibrils. Therefore, the orientation of each pixel in the α-actinin skeleton was compared to the local orientation of actin (Eq 2.3), where local actin orientation was defined as the director in a region that fits the z-lines of two sarcomeres in cardiomyocytes (~5µm x 5µm). Using this method, pixels in the z-line skeleton that had an orientation more parallel to the local direction of actin ($\gamma \geq 0.7$, Eq 2.3), were classified as off-target α-actinin staining and eliminated from the z-line binary skeleton (Fig 2.1C, *dark blue*), and pixels with an orientation more perpendicular to actin were classified as z-lines (Fig 2.1C, *red*). The orientation of actin fibrils can then be used to remove off-target staining from the α-actinin binary skeleton (Fig 2.1D).

2.5.2 Metrics to Quantify Z-line Architecture

With the z-lines automatically isolated from α-actinin stained images, it was possible to explore how to summarize other facets of z-line architecture. The sarcomere orientational order parameter (OOP) has been used to indirectly evaluate z-line architecture[4,7,9,19,46,112]. However, because the sarcomere OOP included regions of off-target staining, the OOP would be lower in tissues with more off-target staining regardless of the z-line organization. Therefore, the OOP of the isolated z-lines more accurately captures the sarcomere organization. Mathematically, the OOP is calculated the same way regardless of the construct (Eq 2.2), thus the OOP will better represent z-line orientational order when it is calculated from only the z-lines (Figs 2.1C and 2.1D).

In addition to more accurately extracting z-lines, actin guided segmentation provides a metric for how much off-target staining is present in images of striated muscles. The amount of

the original α-actinin skeleton that remains after actin orientation guided segmentation (Fig 2.1D, *red*), or the *z-line fraction* quantifies the amount of off-target staining in an image:

$$\text{z-line fraction} = \frac{N_z}{N_\alpha}. \tag{2.4}$$

In Eq 2.4, N_α is the number of pixels in the α-actinin skeleton, and N_z is the number of pixels in the α-actinin skeleton after actin orientation guided segmentation, also referred to as the z-line skeleton. When every pixel in the α-actinin skeleton is approximately perpendicular to its local actin fibrils, the z-line fraction will be 1, and if no pixel in the skeleton is approximately perpendicular, the z-line fraction will be 0.

Another metric of interest was the distribution of continuous z-line lengths. We developed an algorithm to detect and measure the lengths of continuous z-lines, which was validated using synthetic data created to simulate perfectly (Fig 2.2A) and variably continuous z-lines (Fig 2.2B). Each segment consisted of 7 pixels, where a shift of one pixel between segments was considered continuous (Fig 2.2Ai) and a shift of two or more was not considered continuous (Fig 2.2Bi). As z-lines are not always oriented perpendicular to the image, the synthetic data included segments with variable orientations (Figs 2.2Ai and 2.2Bi, *right*). Continuous lines were measured (in pixels) and represented by distinct colors plotted on top of the synthetic data (Figs 2.2Aii and 2.2Bii), with the corresponding lengths color-coded in Fig 2.2C. Measurement of the continuous lines was sensitive to rotation and variation between segments, as indicated by the difference in lengths (Fig 2.2C) between the red, dark blue, and yellow lines in Fig 2.2Aii. The automated protocol accurately reported the position and length of synthetic data that was generated to mimic the appearance of perfectly and non-continuous z-lines in images of α-actinin stained cardiac tissues (Fig 2.2).
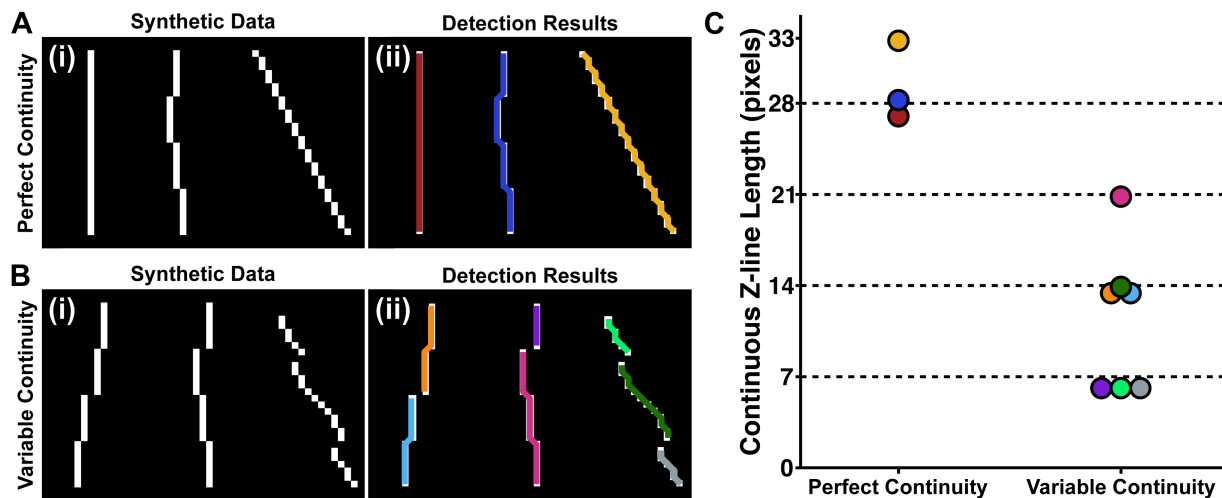
Figure 2.2: **Automatic detection of continuous z-line lengths.** Perfectly **(A)** and variably **(B)** continuous synthetic data. **Ai** and **Bi**, Synthetic data composed of four registered and continuous segments that were each seven pixels long. Segments that were shifted over by one pixel were treated as continuous. **Aii** and **Bii**, Continuous lines plotted as distinct colors on top of the synthetic data. **C**, The length of each continuous line detected in **Aii** and **Bii**, with the colors corresponding to those in **Aii** and **Bii**. The dashed lines indicate the number of pixels that composed continuous segments.

2.5.3 Evaluation of Single Cells with Variable Aspect Ratios

In evaluating the automated method to isolate z-lines from α-actinin stains and measuring continuous z-lines, it is useful to understand how the results relate to other aspects of z-line architecture that can be quantified. For example, in investigating the relationship between maximal traction force and cardiomyocyte aspect ratio, Kuo et al. measured the median z-line registration length in order to summarize lateral registration[27]. Cellular aspect ratio is tightly regulated (~7:1) in healthy ventricles[28–30], but increases[29,30] or decreases[31,32] in some types of heart disease. While related to continuous z-line length, the z-line registration length will invariably be longer, as z-lines that are not continuous can be registered. However, because Kuo et al. found that both lateral registration of z-lines and maximal traction force varied with cellular aspect ratio, it was interesting to evaluate if aspect ratio impacts other facets of z-line architecture accessible with `ZlineDetection`. Thus, the analysis was completed for cardiomyocytes with constant area (2500 µm^2) and variable as-

pect ratios (Fig 2.3A), which were created previously[6]. Because there was variability in the spread of the cells and the maturity of myofibrils within cardiomyocytes of the same area and aspect ratio, prior to running the analysis, we manually classified cells as having good z-line architecture (Figs 2.3A and 2.3Bi), good z-line architecture with bad spread (Fig 2.3Bii), intermediate z-line architecture (Fig 2.3Biii), or immature, underdeveloped (bad) z-line architecture (Fig 2.3Biv). In manual analysis, cells that are not well spread or fully mature are usually eliminated, however our automated analysis made it possible to analyze these cells in addition to cells with good z-line architecture and cell spread. Indeed, the z-line fraction was significantly different between cells with z-line architecture that was good and those classified as intermediate or bad (Fig 2.3C), indicating, unsurprisingly, cells with good z-line architecture contain less off-target α-actinin staining. Thus, the z-line fraction can be used to filter out single cells with unsatisfactory sarcomeric architecture.

For each of the classifications, cardiomyocytes exhibited a skewed distribution of continuous z-line lengths, with shorter continuous z-lines dominating the distribution (Fig A.3), similar to the distribution of z-line registration lengths reported by Kuo et al.[27]. Therefore, the median continuous z-line length was selected as the metric to compare conditions, which captured the differences between cells with good z-line architecture and cells with intermediate or bad z-line architecture (Fig 2.3D). When comparing continuous z-line lengths between cells of different aspect ratios, as expected, the median continuous z-line length was lower than the median z-line registration length reported by Kuo et al. (Fig A.3). `ZlineDetection` can also output the total z-line pixels identified, which can be especially useful when comparing cells of the same area (Fig 2.3E).

In order to compare our results with the maximal traction forces measured by Kuo et al., we estimated the expected stress generated along the major axis of a cell based on sarcomere architecture[20]. Each z-line orientation vector was represented by its angle (θ_i). Because sarcomeres produce a force approximately perpendicular to their z-lines, we assumed that at
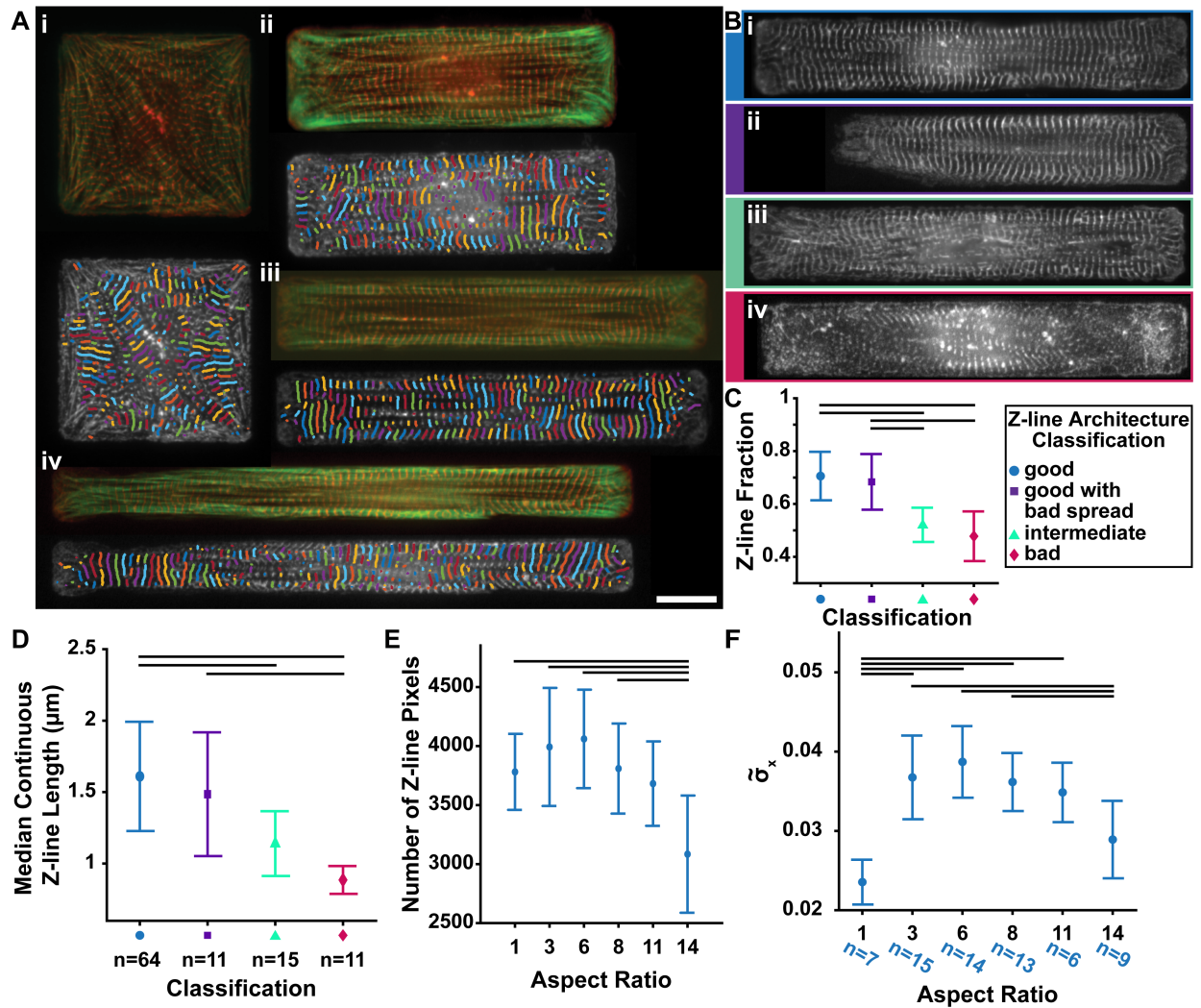
Figure 2.3: **Analysis of cardiomyocytes with variable aspect ratios. A, (top)** Images of single cells with area 2500 µm^2, but variable aspect ratios (**(Ai)** 1:1, **(Aii)** 3:1 **(Aiii)** 6:1 **(Aiv)** 11:1) stained for actin (green) and α-actinin (red) and their corresponding continuous z-lines **(bottom)**. **B**, Representative α-actinin stained cardiomyocytes (extracellular matrix (ECM) island ~6:1 aspect ratio) for each z-line architecture classification: **(Bi)** good z-line architecture, **(Bii)** good z-line architecture with bad spread in ECM island, **(Biii)** intermediate z-line architecture, and **(Biv)** immature, underdeveloped (bad) z-line architecture. **C**, Average z-line fraction for cells. **D**, Average median continuous z-line length for cells (n = 101) within each classification of z-line architecture as described in **C**. **E**, Mean and standard deviation of the number of z-line pixels for the good cells of each aspect ratio. **F**, Mean and standard deviation of the estimated force for the good cells of each aspect ratio. Groups were compared using ANOVA with Tukey's test p <0.05 (black bars in **C**, **E**, and **F**). Scale bar: 15 µm.

each z-line pixel, the force produced by a sarcomere was proportional to the vector perpendicular $(\theta_i + \frac{\pi}{2})$ to the z-line orientation pseudo-vector (θ_i). Thus the stress generated along

25

the major axis of cells with the same area was proportional to the sum of the x-component of the force produced by a sarcomere at each z-line pixel divided by the total number of pixels in the cell area (Eq 2.5):

$$T_x \propto \tilde{\sigma}_x = \frac{\sum_{i=1}^{N_z} \sqrt{\left(\cos\left(\theta_i + \frac{\pi}{2}\right)\right)^2}}{N_T}.$$

(2.5)

In Eq 2.5, the normalized stress, $\tilde{\sigma}_x$, is proportional to the maximal traction force (T_x) along the major axis of the cell, N_z is the number of z-line pixels, N_T is the total number of pixels in the cell area, and θ_i is the orientation of the ith z-line orientation vector. Consistent with published results[27], the theoretical model captures the lower stresses produced by square cells (1:1), which have low z-line orientational order (Fig 2.3Ai and Fig A.3 D). Additionally, consonant with experimental measurements, highly elongated cells (14:1) were predicted to produce a weaker force (Fig 2.3F). Although every cell was engineered to have the same area, highly elongated cells contained fewer z-lines (Fig 2.3E), indicating disrupted myofibril formation at this aspect ratio. However, this force estimate does not capture the strong peak stress that occurs in cells with an aspect ratio of ~7:1 (6:1 or 8:1), which could be due to the large biological variability between cells within each aspect ratio. However, it is also likely the assumption that each z-line pixel is independent, meaning that $\tilde{\sigma}_x$ does not account for either continuity or registration, could account for the lack of a maximum at the ~7:1 aspect ratio.

2.5.4 Z-line Architecture in Engineered Tissues

A motivation for developing this automated analysis protocol was to quantify and compare z-line architecture in tissues using unbiased, quantitative metrics. Previously, characterizing z-line architecture in tissues required manual removal of off-target staining[4,6,9,19,27,46], however, with `ZlineDetection` it is now possible to quantify changes to z-line architecture without the need for user input. The contractile force of engineered tissues is influenced by ECM pattern, where cardiomyocytes seeded on a substrate coated with a uniform layer of FN (Fig 2.4A) produce a weaker contractile force than those seeded on FN lines 20 µm wide with 5 µm gaps between lines (Fig 2.4B)[20]. In addition to FN pattern, there are other experimental conditions that can impact the quality of tissue architecture. For example, seeding cardiomyocytes at a low density (Fig 2.4C) produces sparse tissues that have less developed myofibrils[132]. Similarly, BDM, which inhibits myosin ATPase, disrupting the actin-myosin interaction, has been qualitatively noted to disrupt z-line registration in cardiac and skeletal muscle cells[109,110] and shown to cause a decrease in contractile force[133]. Therefore, the z-line architecture was compared between isotropic (Fig 2.4A), anisotropic (Fig 2.4B), sparse anisotropic (Fig 2.4C), and BDM treated anisotropic (Fig 2.4D) tissues.

As expected, the orientational order of the z-lines was significantly different between isotropic and anisotropic tissues (Fig 2.4E). While the sparse anisotropic and BDM treated anisotropic tissues tended to follow the orientation of the FN pattern and had higher orientational order than isotropic tissues (Fig 2.4E), the tissues contained malformed myofibrils and therefore had a lower orientational order than anisotropic tissues. However, the value of the orientational order parameter by itself does not indicate the degree of malformation of tissues or the impact on z-line continuity. In contrast, the z-line fraction was significantly lower in the sparse anisotropic and BDM treated anisotropic tissues than in the isotropic and anisotropic tissues (Fig 2.4F), which was expected because of off-target α-actinin staining
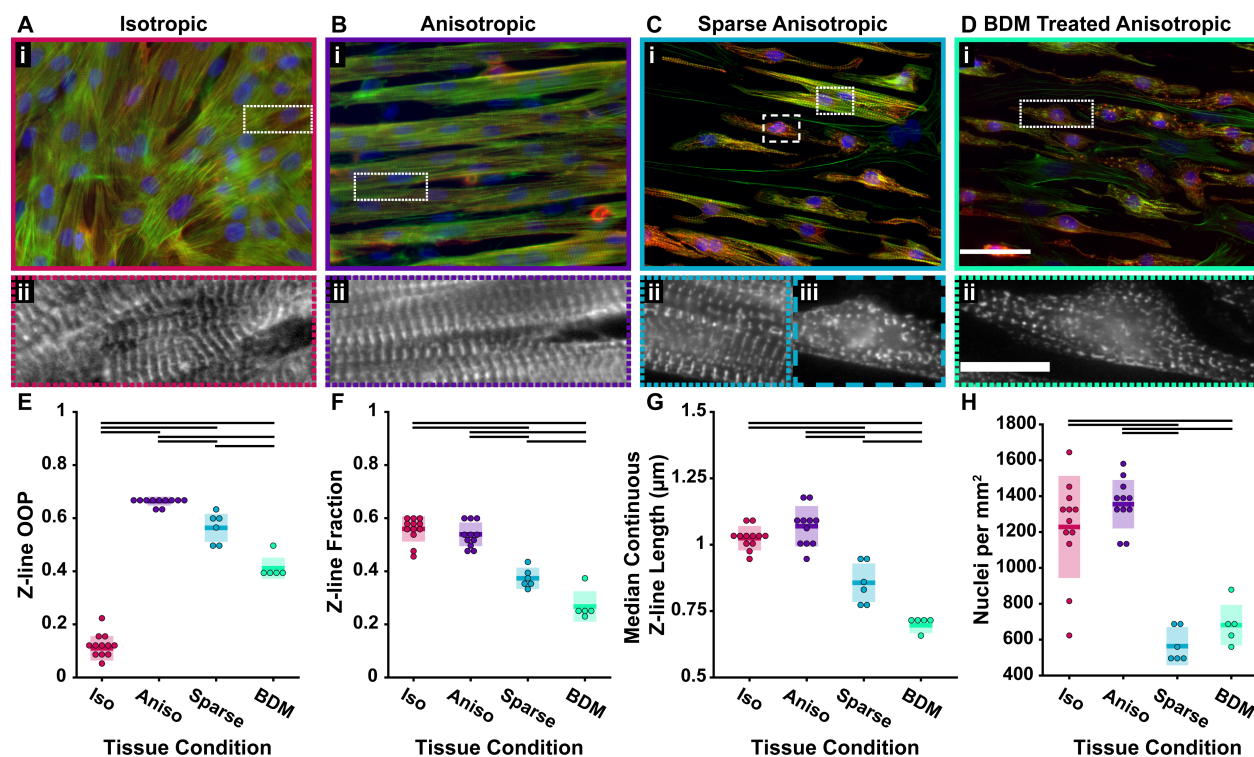
Figure 2.4: **Comparison of cardiac tissues. A-D**, Cardiac tissue stained for actin (green), α-actinin (red), and nuclei (blue) on a uniform layer of FN **(A)**, FN in lines **(B)**, FN in lines with sparsely seeded cardiomyocytes **(C)**, and FN in lines with cardiomyocytes treated with BDM **(D)**. **E**, Z-line OOP. **F**, Z-line fractions. **G,** Median continuous z-line lengths. **H**, Nuclei per area. In **E-H** Each dot represents a coverslip. In **E-H**, each dot represents a single coverslip, colored bars represent the mean, and colored boxes represent the standard deviation. Groups were compared using ANOVA with Tukey's test p <0.05 (black bars in **E**, **F**, **G** and **H**). Number of coverslips (cs) for each condition: isotropic cs = 12, anisotropic cs = 11, sparse anisotropic cs = 6, BDM treated cs = 5. Scale bars: **(A-Di)** 50 µm; **(A-D ii)** 15 µm.

along immature stress fibers and cell boundaries[3] (Figs 2.4Ciii and 2.4Dii). The z-line fraction was sensitive enough to be able distinguish between anisotropic tissues and either sparse anisotropic or BDM treated anisotropic tissues with as few as 2-3 coverslips of each tissue. Additionally, the median continuous z-line length was significantly lower in both the sparse anisotropic and BDM treated anisotropic tissues than the isotropic and anisotropic (Fig 2.4G, Fig A.4). While the z-line architecture of the single cells was expertly classified as good, intermediate, or bad, it was impractical to classify individual cells within whole tissues. Therefore, the z-line fraction of the anisotropic and isotropic tissues falling between

the z-line fraction of good and intermediate single cells (Fig 2.3C) indicated that these tissues contain cells with both good and intermediate z-line architecture. Similarly, the median continuous z-line length for the anisotropic and isotropic tissues was lower than the median continuous z-line length for single cells with good z-line architecture and closer to that of cells with intermediate z-line architecture (Fig 2.3D).

Both sparse seeding and treatment with BDM produced tissues with poor z-line architecture, which was quantified by the z-line fraction and median continuous z-line length. However, sparse anisotropic tissue contained regions that appeared more developed (Fig 2.4Cii) and looked similar to well-formed anisotropic tissues (Fig 2.4Bii), as well as regions with z-line architecture that appeared similar to tissues treated with BDM (Figs 2.4Ciii and 2.4Dii). Although the sparse anisotropic and BDM treated anisotropic tissues contained a similar number of cells in a given field of view, as indicated by the number of nuclei (Fig 2.4H), both the z-line fraction and median continuous z-line length were significantly higher in the sparse anisotropic than the BDM treated anisotropic (Figs 2.4F and 2.4G). These results indicate that treating tissues with BDM produced tissue with more disrupted z-line architecture than was produced by seeding at a low density.

2.6 Discussion

In this work, we developed `ZlineDetection`, an image analysis protocol to characterize z-line architecture in α-actinin stained striated muscle tissues. Using improved z-line extraction and a biologically motivated approach to segmenting off-target staining, we were able to automatically and accurately isolate z-lines. We also designed and implemented an algorithm to measure the length of continuous z-lines, which is physically related to z-line registration[27,58,59,134,135]. Improved z-line extraction coupled with a variety of metrics allowed `ZlineDetection` to capture differences in z-line architecture among standard engineered

cardiac tissues (Fig 2.4).

A major achievement of this work was automating z-line isolation, making analysis of z-line architecture in single cells, engineered tissues, and tissue sections[111] possible without the need for experts to trace z-lines[27] or manually segment off-target staining[6,9,19,46,111]. Segmentation guided by local actin orientation eliminates pixels that correspond to off-target staining, where in manual segmentation it is only possible to eliminate large regions of off-target staining. Consequently, subsequent analysis of the orientational order of z-lines in anisotropic tissues (Fig 2.4E) resulted in a higher OOP than previously reported when segmentation was done manually[19]. This quantitatively demonstrates the advantages of the `ZlineDetection` algorithm even if only the previously explored metrics are used. Although there are many different approaches to segmentation of biological images[75,77], in addition to not requiring user training, the actin guided segmentation also provides additional information about the amount of off-target staining, which occurs along immature stress fibers and cell boundaries[3]. Accordingly, the z-line fraction captured differences in the architecture quality between expertly classified single cells (Fig 2.3C). Furthermore, the z-line fraction was able to successfully distinguish between malformed and well-formed tissues, as we showed that malformed tissues contained more off-target staining than well-formed anisotropic and isotropic tissues (Fig 2.4G). Without the use of actin guided segmentation, the orientational order parameter of α-actinin combined organization of z-lines and the amount of off-target staining, while the z-line fraction and z-line OOP quantified both aspects of architecture separately. Decoupling these two metrics is essential, as although an expert would consider both the isotropic (Fig 2.4A) and anisotropic (Fig 2.4B) tissues to be well-formed, the α-actinin OOP alone would indicate that the isotropic tissues were both disorganized and low quality, rather than only disorganized.

In the absence of the actin co-stain, α-actinin pixels can no longer be classified as z-lines or off-target staining, and `ZlineDetection` can no longer decouple these two metrics and

instead reports the simple α-actinin OOP that has been used previously[6,19,27,46]. Existing algorithms that quantify sarcomere architecture from only a z-line stain, isolate z-lines from off-target staining by using signal processing to identify double wavelets in an image[1], quantify local, micron-scale organization[24], or manually remove off-target staining[6,19,27,46]. These previous works have used a range of metrics to then classify tissue or cell architecture, many of which describe similar properties to those provided by `ZlineDetection`. For example, the local sarcomere organization algorithm developed by Sutcliffe et al.[24] scored isolated cells without actin co-staining (Figs 4 and 6d in Sutcliffe et al.[24]) with a sarcomere organization index, which ranges from 0-2. The sarcomere organization index[24] was ~0.1 for a primary cell they qualitatively classified as "disorganized", but ~0.4 for both a "well-organized" primary cell and a reprogrammed cardiomyocyte, even though the latter had disorganized myofibrils and some α-actinin punctate patterns indicative of premyofibrils. By contrast, the α-actinin OOP, which measures organization globally, was 0.2, 0.52, 0.17 for the three cell types, respectively. As such, the cell-tissue scale OOP and the sarcomere scale organization index[24] provide qualitatively different measurements, but the key difference is in the scale at which the measurement is happening. Because tissue level organization influences the strength of tissue contraction[20], we believe a global metric is essential. Nevertheless, the main advantage of using the actin co-stain to isolate z-lines is the ability to quantify the amount of off-target staining based on the additional biological information. This can be especially useful in analyzing noisy stem cell derived cardiomyocytes. For example, a square stem cell derived cardiomyocyte shown in a previous publication[136] was easily analyzed with `ZlineDetection` (z-line OOP = 0.17, z-line fraction = 0.48, median continuous z-line length = 0.87 μm). While not an interesting metric in primary cardiomyocytes, `ZlineDetection` also reports the distance between z-lines (i.e. sarcomere length), which is often used to quantify cardiomyocyte maturity[52,137] and disease state[138].

In addition to the orientational order, the relative spatial location of z-lines in neighboring myofibrils (e.g. continuity or registration of z-lines) has been used to evaluate striated

myocytes[58,59,134,135]. In this work, we created and automated an algorithm to measure con-
tinuous z-lines by grouping z-line pixels based on relative orientation and location. Con-
sistent with the observation that BDM disrupts the formation of z-lines[109,110], the median
continuous z-line length was significantly lower in BDM treated anisotropic tissues than the
malformed tissues that were created by seeding cardiomyocytes at a lower density (Fig 2.4G).
This demonstrates one of the utilities of `ZlineDetection` is its ability to evaluate the qual-
ity of cardiac tissues or other striated muscle without introducing user bias. The median
continuous z-line length was not significantly different between isotropic and anisotropic tis-
sues, which suggests that z-line continuity is not impacted by FN pattern. However, because
isotropic tissues are weaker than expected based on OOP alone[20], it is worth investigating
if differences in z-line registration[21,56,57,61] rather than continuity could be accounting for
the difference in contractile strength. Further, although the orientational order and num-
ber of z-lines accounts for the low stresses produced by single cells at aspect ratio 1:1 and
14:1[27](Fig 2.3F), z-line registration might account for the peak in contractile strength at the
aspect ratio ~7:1 compared to other aspect ratios which have similar orientational order and
number of z-lines. The suggestion that z-line registration influences contractile strength only
in the presence of high orientational order aligns with the liquid crystal view that smectic
order (i.e. registration) has no meaning in the absence of high nematic order (i.e. high
orientational order).

While `ZlineDetection` is a significant step forward in automating sarcomere architecture,
as with any analysis method, it is not without limitations. Although using local actin ori-
entation to classify α-actinin staining as off-target effectively captured differences between
well-formed and malformed tissues as well as more accurately isolated z-lines, actin guided
segmentation falters in cases where tissues are not organized in a pure myocyte monolayer as
fibroblasts can sit on top of or under myocytes (Fig 2.1D). Therefore, future work involves
adapting our analysis protocol to confocal z-stacks and eliminating the actin of non-myocytes.
Additionally, the image analysis pipeline and corresponding parameters were optimized for

a resolution ~6 pixels/µm. However, if the images are of particularly bad quality (i.e. dominated by background fluorescence) the suggested parameters might need to be adjusted, but we caution users against using images of poor quality (Fig A.5) as information is invariably lost. Another consideration in choosing parameters is that the continuous z-line lengths in particular are sensitive to the amount and duration of smoothing in the anisotropic diffusion filtering step. Although there has been work on calculating the parameters for anisotropic diffusion filtering based on the statistics of the images[139–141], there is not an emphasis on preserving edges and continuity of line segments, which is how we selected our parameters (Fig A.2). Therefore, we made `ZlineDetection` open source and adaptable to improvements and advancements in image analysis and quantitative parameter selection. It is worth noting that `ZlineDetetion` can be used with other stains or methods of visualizing cardiac striations. For example, it is possible to analyze videos previously published by Sharma et al.[142] of unfixed cells that express florescent proteins. Such an analysis in the absence of a co-stain would result in OOP of the expressed protein labeled structures and the striation lengths as a function of time (Fig A.6). While the median is a useful metric to summarize a skewed distribution and the median continuous z-line length was significantly different between malformed and well-formed tissues (Fig 2.4G), it is possible that the relative location and distribution of continuous z-lines are important predictors of stress generation. Therefore, future work includes creating a method to measure registration and examining its relationship with z-line continuity and contractile function. Further, the ability to measure and quantify registration could be impactful in other fields, because registration of cellular structures may be important in different cell types[57,61].

2.6.1 Conclusion

Our image analysis protocol and implementation can be used as a tool to quantitatively compare z-line architecture in single cells and tissues under different conditions and between

labs. This would increase the scientific rigor in the field by eliminating qualitative and/or manual analysis that introduces lab/user specific bias. Indeed, one of the key achievements of `ZlineDetection` is the ability to segment off-target staining automatically. An additional advantage of the biologically motivated segmentation approach was that the amount of off-target staining can be used to compare quality of tissue formation. A second key achievement was identifying experts' criteria for evaluating the quality of striated tissues, as the z-line orientational order, intact z-line fraction, and the relative spatial alignment of z-lines. A third key achievement of this capability was elucidating the mechanism by which cardiomyocytes with an elongated aspect ratio become inefficient at producing force. Having the ability to measure continuous z-lines can pave the way to predicting force measurements as it relates to z-line architecture in cardiac tissues through the use of experimental and mathematical modeling approaches. Finally, in the future these computational methods can be used as a quality control to analyze z-line architecture in stem cell derived myocytes, engineered tissues, diseased tissues, and tissues subjected to injury and treatment with pharmacological agents.

2.7   Acknowledgments

CHAPTER 3

A Computational Framework for Profiling Myofibrillar Deformations in Skeletal Muscle

3.1 Introduction

In skeletal muscle, muscle fiber defects and myofibrillar malformations have been linked to decreased force production and increased injury susceptibility in both aging and disease, such as Duchenne muscular dystrophy[143–147]. While these deformations may be an important predictor of altered function, injury susceptibility, and disease progression, their occurrence has not been quantitatively characterized. Furthermore, qualitative evidence that myofibrillar changes progress with disease severity suggests that they may underlay loss of function in disease and aging skeletal muscle[146]. In order to test this hypothesis and to also determine if the frequency and severity of myofibrillar malformation increase with age, it is necessary to profile myofibrillar malformations.

Because the sarcomere is the contractile unit of striated muscle, evaluation of myofibril structure often involves characterizing the architecture of sarcomere striations, such as z-lines or m-lines[1,24,107]. One important aspect of sarcomere architecture is its orientational order, as the uniaxial force generated by sarcomeres is maximized when they are all oriented in the same direction[4,7,19,46,107,112]. In addition to the orientational order of sarcomeres, the lateral alignment of sarcomeres from neighboring myofibrils has been hypothesized to influence striated myocyte function and has therefore been incorporated into theoretical models of contractile function as well as used to evaluate damage to striated myocytes[21,27,56–61,107]. Quantifying characteristics of sarcomere order requires imaging striated myocytes that have

been labeled for sarcomere structures, processing the images to segment the structures of interest, and then incorporating or developing intuitive metrics.

In this Chapter, we will illustrate how the striation continuity metric established in Chapter 2 can be adapted and applied to z-stacks of skeletal muscle labeled with actin in collaboration with Anicca Harriot and Christopher Ward, Ph.D. at the University of Maryland.

3.2 Methods

3.2.1 Experimental Data

All experimental data was generated by Anicca Harriot in the laboratory of Christopher Ward, Ph.D. at the University of Maryland.

3.2.2 Myofiber Detection

The myofiber was segmented by smoothing either the maximum intensity projection of a z-stack (Figure 3.1A) or the 2D image, with a Gaussian filter and then the smoothed image was binarized using Otsu's method[148]. The binary image (Figure 3.1B) was evaluated by determining the area of the image taken up by the myofiber, as well as the number of objects in the binary image. If there were multiple binary objects in the image, only the largest binary object was included in analysis. The orientation of the myofiber was calculated using a least mean square orientation estimation algorithm (Figure 3.2K)[129,130]. The minor axis of the myofiber was calculated by first finding the boundary (i.e. outline) of the myofiber from the binary image (Figure 3.1C,D, magenta). The width of myofiber was determined by calculating the distance from the longest continuous boundary line to the closest perpendicular boundary (Figure 3.1C, purple). The longest continuous line along the myofiber

boundary (Figure 3.1C, blue) was determined using the continuous line detected described in Chapter 2 and Morris et al.[107]. The width of the myofiber was calculated for boundary points spaced 20 pixels apart (Figure 3.1C, purple). The minor axis length was set to the median myofiber width (Figure 3.1D, cyan).
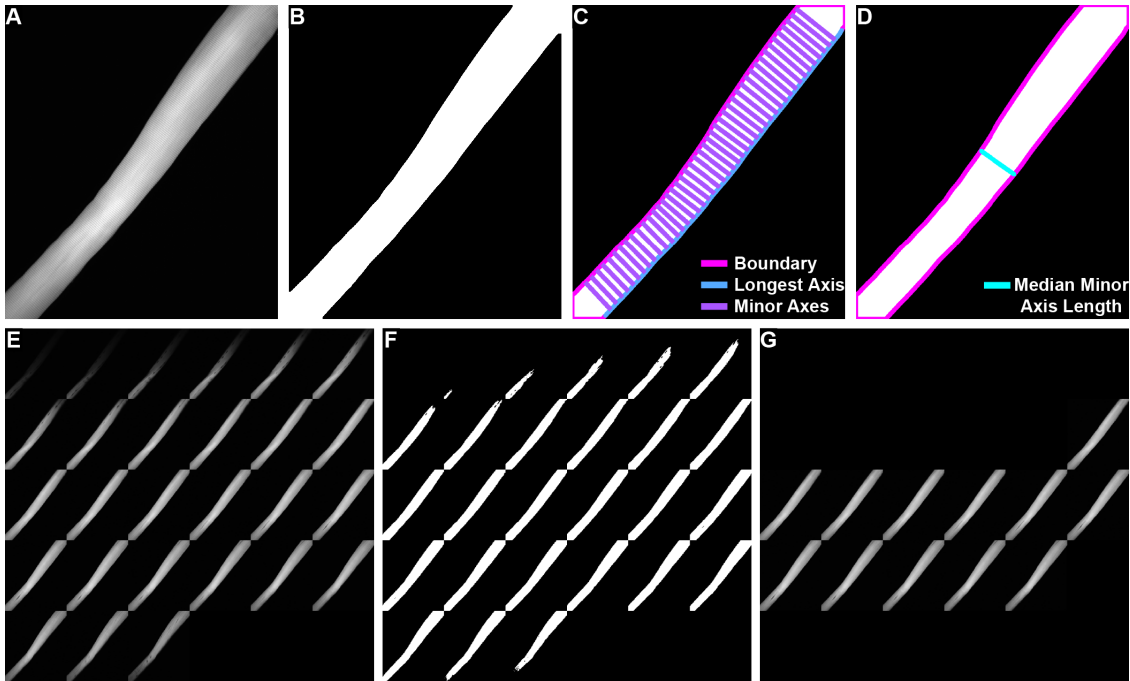
Figure 3.1: **Myofiber Analysis**. **A.** All z-slices in the z-stack. **B.** Binarized z-slices shown in A. **C.** Z-slices selected to be analyzed. **D.** Maximum intensity projection. **E.** Binarized maximum intensity projection shown in D. **F.** The boundary (magenta), longest axis (blue), and minor axes (purple) plotted on top of the binarized maximum intensity projection shown in E. **G.** The boundary (magenta) and the median minor axis length (cyan).

3.2.3   Z-Slice Selection

To determine which z-slices in a z-stack contained a complete section of the myofiber and should therefore be included in the myofiber striation analysis, each z-slice (Figure 3.1E) was binarized (Figure 3.1F) and then compared with the binarized maximum intensity projection (MIP) (Figure 3.1B). In order to compare these binary images, the number of `true` pixels in the binary image generated from the current z-slice (BW_{zi}) was compared with the number

of `true` pixels in the binarized maximum intensity projection (BW_{mip}):

$$N_{zi} = \frac{\text{Number of } \texttt{true} \text{ pixels in } BW_{zi}}{\text{Number of } \texttt{true} \text{ pixels in } BW_{mip}}. \tag{3.1}$$

If there was a sufficient amount of the myofiber in the z-slice, i.e. if N_{zi} from Equation 3.1 was greater than the threshold, n_{thresh}, the current z-slice (z_i) was included in analysis, otherwise z_i was not analyzed. If the minimum number of z-slices in the z-stack did not meet the condition $N_{zi} > n_{thresh}$, the threshold, n_{thresh}, was reduced by Δ_{thresh} until at least the minimum number of z-slices was included in analysis. The parameter values used were $n_{thresh} = 0.6$, $\Delta_{thresh} = 0.025$, and minimum number of z-slices $= 1$.

3.2.4 Striation Detection

The process of creating a binary skeleton of the actin sarcomere striations was adapted from the image analysis protocol `ZlineDetection`, developed for α-actinin striations. Briefly, gray-scale images (Figure 3.2A,B) were smoothed using coherence enhancing anisotropic diffusion filtering (Figure 3.2C), which calculates the eigenvectors of the image Hessian to direct diffusion and uses a finite difference scheme to perform the diffusion, repeating until diffusion time is reached[122–125]. The diffusion time and smoothing parameters were set according to Morris et al.[107]. After contrast enhancement using top hat filtering[127] (Figure 3.2D), bottom hat filtering was used to remove the striations present in between m-lines, at the z-lines (Figure 3.2E,F). Finally, the images were binarized by global thresholding (Figure 3.2G) and then thinned to one pixel width and trimmed in order to obtain the striation skeleton (Figure 3.2H). Local orientation was estimated from the diffusion filtered image using a least mean square orientation estimation algorithm[129,130] (Figure 3.2J).

3.2.5 Striation Continuity

After generation of the binary skeleton and corresponding orientation vectors, the continuous striations were detected using the method developed and implemented by Morris et al.[107] in `ZlineDetection`. In order to quantify the striation continuity, the striation lengths were then divided by the minor axis length of the myofiber (Figure 3.2I)

$$\text{striation continuity fraction} = \frac{\text{striation length}}{\text{minor axis length}}. \tag{3.2}$$
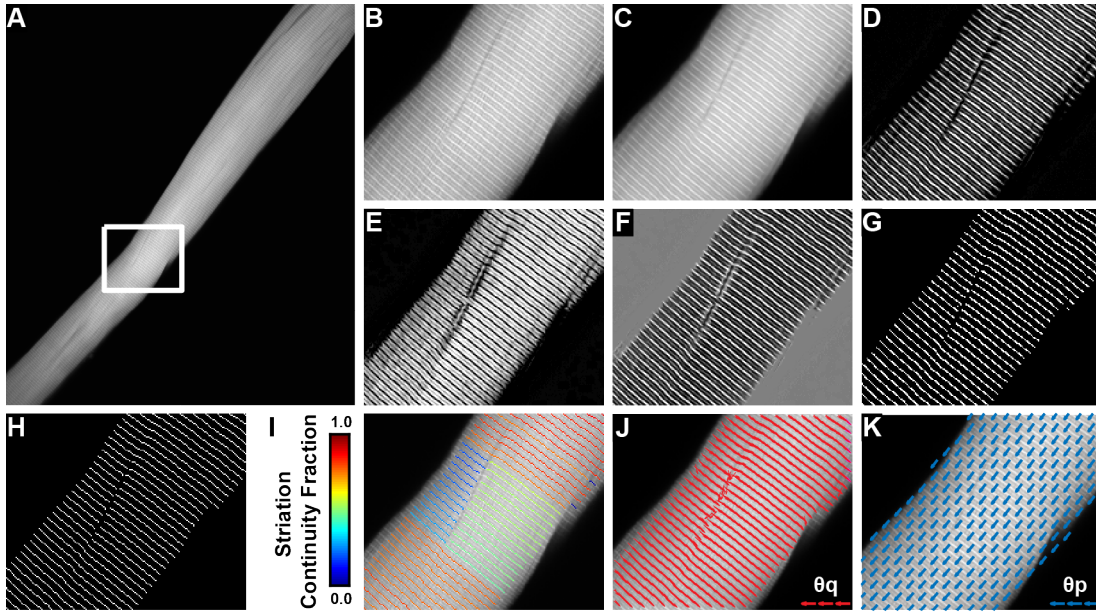
Figure 3.2: **Image Processing. A.** Example z-slices with the section shown in B-K plotted in white. **B.** Zoom in section of the myofiber. **C.** Anisotropic diffusion filtered image. **D.** Top-hat filtered image. **E.** Bottom-hat filtered image. **F.** Top-hat minus bottom hat-filtered image. **G.** Binarized image. **H.** Skeletonized image. **I.** Continuous striations plotted based on the striation continuity fraction. **J.** Striation orientation vectors (θ_q). **K.** Myofiber orientation vectors (θ_p).

3.2.6 Striation Organization: Co-orientational Order Parameter

The co-orientational order parameter (COOP) developed by Drew et al.[6] was used to quantify the orientational order (i.e. organization) of the striations. The COOP was designed to evaluate the correlation of the orientation of coupled constructs, in this case, the striations (Figure 3.2J) and the myofiber (Figure 3.2K). Briefly, the COOP is defined as the maximum eigenvalue of the structure tensor $\mathbb{T}_{PQ}$:

$$\mathbb{T}_{PQ} = \left\langle 2 \begin{bmatrix} f_{i,x}f_{i,x} & f_{i,x}f_{i,y} \\ f_{i,x}f_{i,y} & f_{i,y}f_{i,y} \end{bmatrix} - \mathbb{I} \right\rangle. \tag{3.3}$$

The field F is defined as a set of pseudo vectors $\overrightarrow{f_i}$:

$$f_{i,x} = \overrightarrow{p_i} \cdot \overrightarrow{q_i} = p_{i,x}q_{i,x} + p_{i,y}q_{i,y} = \cos(\theta) \ , \tag{3.4}$$

$$f_{i,y} = \left| \overrightarrow{p_i} \times \overrightarrow{q_i} \right| = p_{i,x}q_{i,y} - p_{i,y}q_{i,x} = \sin(\theta), \tag{3.5}$$

and it represents the angle (θ) between the two biological constructs, $\overrightarrow{p_i}$ and $\overrightarrow{q_i}$. In this case, P is defined as a set of pseudo vectors $\overrightarrow{p_i}$ corresponding to the myofiber (Figure 3.2K), and Q as a set of pseudo vectors $\overrightarrow{q_i}$ corresponding to the striations (Figure 3.2J). The COOP ranges from zero to one, where a value of zero indicates no correlation and one indicates perfect correlation between the orientations of the striations and the myofiber.

3.3 Results

In order to quantify the occurrence and severity of myofibrillar deformations in striated muscle, we first developed an image processing program to isolate sarcomeric striations. The pipeline was adapted from the work done in Morris et al.[107] and described in Chapter 2. In

the data discussed in this chapter, the sarcomere striations are reliably distinguishable in actin labeled images, which was not the case for the majority of striated myocytes presented in Chapters 2,4, and 5. Therefore the computational protocol established for α-actinin z-lines could be applied to these actin labeled images, with an important biological and therefore computational distinction. In these actin stained images, it is the m-line, not the z-line that appears as a bright striation. The z-line, which does not contain any actin, is occasionally also visible, but appears as a thin line in between m-lines. Thus the image processing protocol was adapted to isolate only the bright m-line striation and ignore the dark z-line striation (Fig 3.2).

Once the sarcomere striations were extracted from the images, aspects of their architecture could be quantified and used to profile myofibrillar deformations in skeletal muscle. As the orientation of the myofibrils was qualitatively described as "chaotic" in aged or diseased myofibers, as opposed to organized in healthy, young myofibers, the orientational order of sarcomeres was quantified. In order to ignore changes in sarcomere orientation that were purely due to changes in the gross myofiber orientation, the Co-Orientational Order Parameter (COOP) was used to describe sarcomere organization with respect to the myofiber direction[6]. However, the COOP did not capture more subtle alterations in myofibrillar architecture (Fig 3.3A). Therefore, an alternative metric, the continuity of sarcomere striations among neighboring myofibrils was utilized. In previous work (Chapter 2, Morris et al.[107]), the distribution and median continuous z-line length was used to evaluate engineered tissues. However, it lacked some interpretability, as there was not an unbiased, objective "ideal" or standard continuity length for muscle tissues. This issue was circumvented in the images of skeletal muscle by quantifying the continuity fraction (Equation 3.2), which we define as the striation length divided by the width of the myofiber (i.e. minor axis length) (Fig 3.1). Using this metric, a striation that spanned the entire width of the myofiber would have a value of 1. Furthermore, if a myofiber has sarcomere striations that all span the entire width of the myofiber, the striation continuity fraction would be 1 for each of the striations. The median

continuity fraction was chosen as a metric to describe the distribution of continuity fractions
(Fig 3.3B). Preliminary results suggest that the median continuity fraction can distinguish
among myofibers from young, aged, and diseased mice (Fig 3.3C).
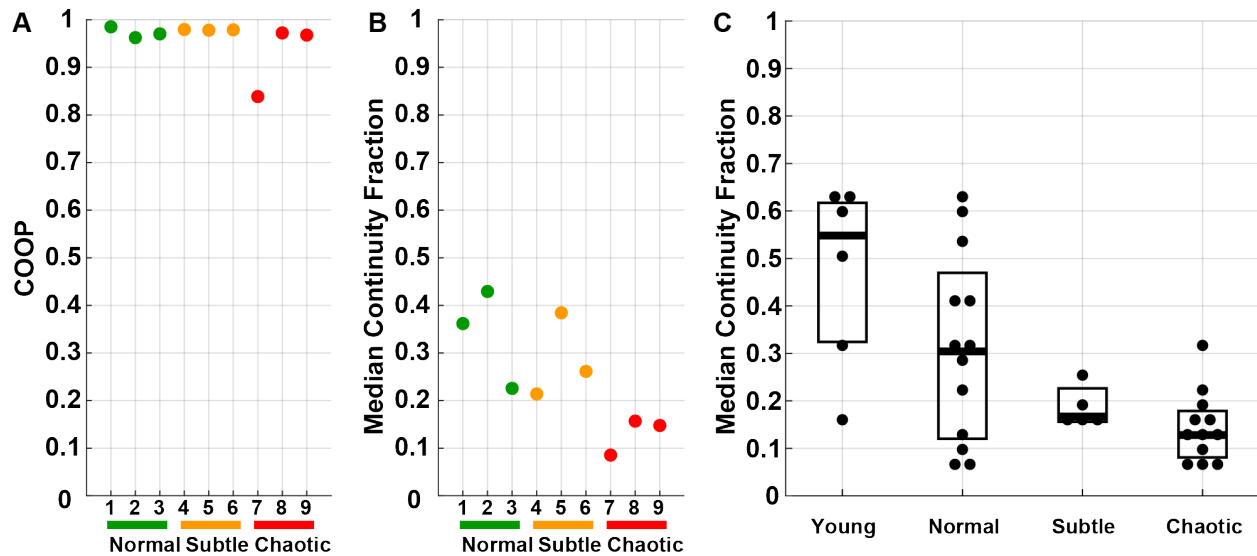
Figure 3.3: **Preliminary Results of Analyzing Skeletal Myofibers**. **A.** COOP of
representative images, colored by the expert classification. **B.** Median continuity fraction of
representative images, colored by the expert classification.**C.** Box plots showing the median
continuity fraction for z-stacks of different experimental conditions and expert classifications.
Each point represents the median continuity fraction of an individual z-stack.

3.4 Discussion and Conclusion

In this work, we developed a framework for characterizing myofibrillar deformations in skele-
tal muscle. Automated myofiber and striation segmentation and customized metrics provides
a comprehensive tool for evaluating skeletal myofibers in an unbiased manner. Previous
approaches for profiling myofibrillar deformations in skeletal muscle relied on qualitative
expert classification. The computational approach discussed in this chapter quantitatively
summarizes morphological alterations and can be used for further study into how aging and
pathology impacts morphology and how morphology influences function.

While this image analysis pipeline is being used to characterize differences among aged, dis-

eased, and healthy myofibers, it is not without its limitations. The first is how to summarize the differences between myofibril formation at different depths of the myofiber (i.e. differences between z-slices) in a biologically meaningful manner. The analysis would also benefit from incorporating other labeled constructs, such as nuclei, and reporting how the presence or absence of these constructs influences the striation continuity. This collaborative effort between experimental and computational groups will result in a deeper understanding of myofibrillar architecture and its correlation with aging and disease.

CHAPTER 4

Characterization of Cellular Architecture in Immature, Multi-Layer Cardiac Tissues

4.1 Introduction

Induced pluripotent stem cells (iPSCs)[149,150] provide a powerful platform for basic research, disease modeling, drug development, and regenerative medicine because they can be differentiated into otherwise inaccessible patient-specific cell types, such as cardiomyocytes[97,151–153]. For example, in Mehrabi et al., *Submitted 2021*, patient specific iPSC-derived cardiomyocytes were used to investigate the pathological effects of mutations in the Lamin A/C (*LMNA*) gene, which causes inherited heart disease in patients[85]. While iPSC-derived cardiomyocytes have been used to model many diseases[13,154–158], the heterogeneity and variability of the resulting cellular populations make it difficult to interpret the results of any single experiment[97]. Much of the heterogeneity in iPSC-derived cardiomyocytes is attributed to their immaturity, which influences fundamental cardiomyocyte properties including cell morphology, gene expression, contractility, electrophysiology, calcium handling, metabolism, and proliferation[97,159,160]. An additional challenge is that when iPSC-derived cardiomyocytes are used in engineered tissues, they often appear in multiple layers, rather than in 2D laminar sheets as observed in primary cardiac tissue. With these challenges in mind, we developed an approach to quantitatively evaluate the architecture of immature, multi-layer cardiac tissues in each serial optical section (z-slice).

4.2 Methods

4.2.1 Experimental Data

All experimental data was generated by Mehrsa Mehrabi, Ph.D., while in the laboratory of Anna Grosberg, Ph.D. at University of California, Irvine.

4.2.2 Actin Orientation Detection

Each actin stained z-slice was enhanced using contrast-limited adaptive histogram equalization[161]. After enhancing the contrast of each actin stained z-slice, the orientation of actin at each pixel was calculated as described previously[19,46]. Briefly, each image was filtered with a Gaussian kernel and then normalized to have zero mean and unit standard deviation[130]. The orientation was estimated using a least mean square orientation estimation algorithm[129,130]. The orientation vectors for each z-slice were concatenated for the entire z-stack (field of view), and the orientation vectors of each field of view were concatenated for the entire coverslip. Therefore, the total number of actin orientation vectors for a coverslip was calculated by summing the number of orientation vectors contained in each field of view. The orientational order of the actin contained in a coverslip was quantified by the the Orientational Order Parameter (OOP), which has been described previously[36,131].

4.2.3 Sarcomere Length & Orientation

After the contrast of each α-actinin stained z-slice was enhanced[161], the entire z-stack was median filtered[162]. The sarcomeres in each z-slice were detected by first using the "Sarc-Track" algorithm which identifies double wavelets in an image[1]. The angle of each detected

double-wavelet was then compared to the local orientation of actin to remove false sarcomeres, as described in "ZlineDetection"[107]. The average sarcomere length, sarcomere OOP, and total number of sarcomeres for each coverslip was calculated after combining all of the z-stacks for that coverslip, as described for actin.

4.2.4   Nuclei Detection & Evaluation

Nuclei in DAPI stained z-stacks were detected by first segmenting each z-slice and then grouping nuclei that appeared in multiple z-slices. The two-dimensional segmentation was done by first binarizing each z-slice using the "CARE" algorithm[68]. After removing small objects, the watershed transform was performed on the distance transform, which had been modified to filter out tiny local minima[163–166]. Individual nuclei that appeared in multiple z-slices were grouped by comparing the segmentation results for each neighboring z-slice. Finally, the maximum projection of each individual nucleus was saved after being approved by the user. The maximum projection of each nucleus was then evaluated by calculating the area, perimeter, eccentricity, maximum negative curvature, mean negative curvature, and relative concavity, as well as classified as normal or dysmorphic, as described previously[69].

4.3   Results

4.3.1   Characterization of Sarcomere Architecture

In order to better interpret patient-specific experiments using iPSC-derived cardiac tissue and compare iPSC-derived with primary cardiac tissue, it is necessary to fully evaluate their sarcomere architecture. Characterizing sarcomere architecture in iPSC-derived cardiac tissue and other multi-layer tissues requires the development of a platform that quantifies

sarcomere or z-line architecture in images that capture the 3D structure, such as serial optical sections (z-stacks). Therefore, we developed a computational method to evaluate sarcomere architecture in z-stacks of striated tissues by using the information contained in each serial optical section (z-slice). Although taking the maximum intensity projection of a z-stack is a common way to present and process the images, in multiple layer tissues, constructs belonging to different cells will often overlap in the z-axis making it impossible to detect and distinguish between them (Fig 4.1C). Further, in order to properly visualize multiple layer cardiac tissues, the spacing between each z-slice is usually small enough such that myofibrils will appear in multiple z-slices. Thus, a z-line will be visible in multiple z-slices, but will have diminished or irregular fluorescence intensity in a single z-slice, making it difficult for the 2D approach presented in Chapter 2 to accurately segment the z-lines of immature iPSC-derived cardiomyocytes. However a pipeline developed by Toepfer et al.[1], `SarcTrack`, was able to detect the majority of sarcomeres in a z-slice of iPSC-derived cardiac tissue. `SarcTrack`[1] identifies sarcomeres in a 2D image of a tissue with fluorescent z-lines by convolving an image with a bank of "double-wavelets" (Fig 4.1C). As part of this work, we improved `SarcTrack`[1] by comparing the angle of each detected double-wavelet to the local orientation of actin to remove false sarcomeres, as established in Chapter 2.4.7[107]. The combination of these two techniques allowed for considerably better detection of sarcomeres than either technique by itself. Using this combination approach made it possible to report and compare the sarcomere lengths and sarcomere OOP[36,131] of iPSC-derived cardiomyocytes from patients with mutations in the *LMNA* gene (Mehrabi et al., *Submitted 2021*).
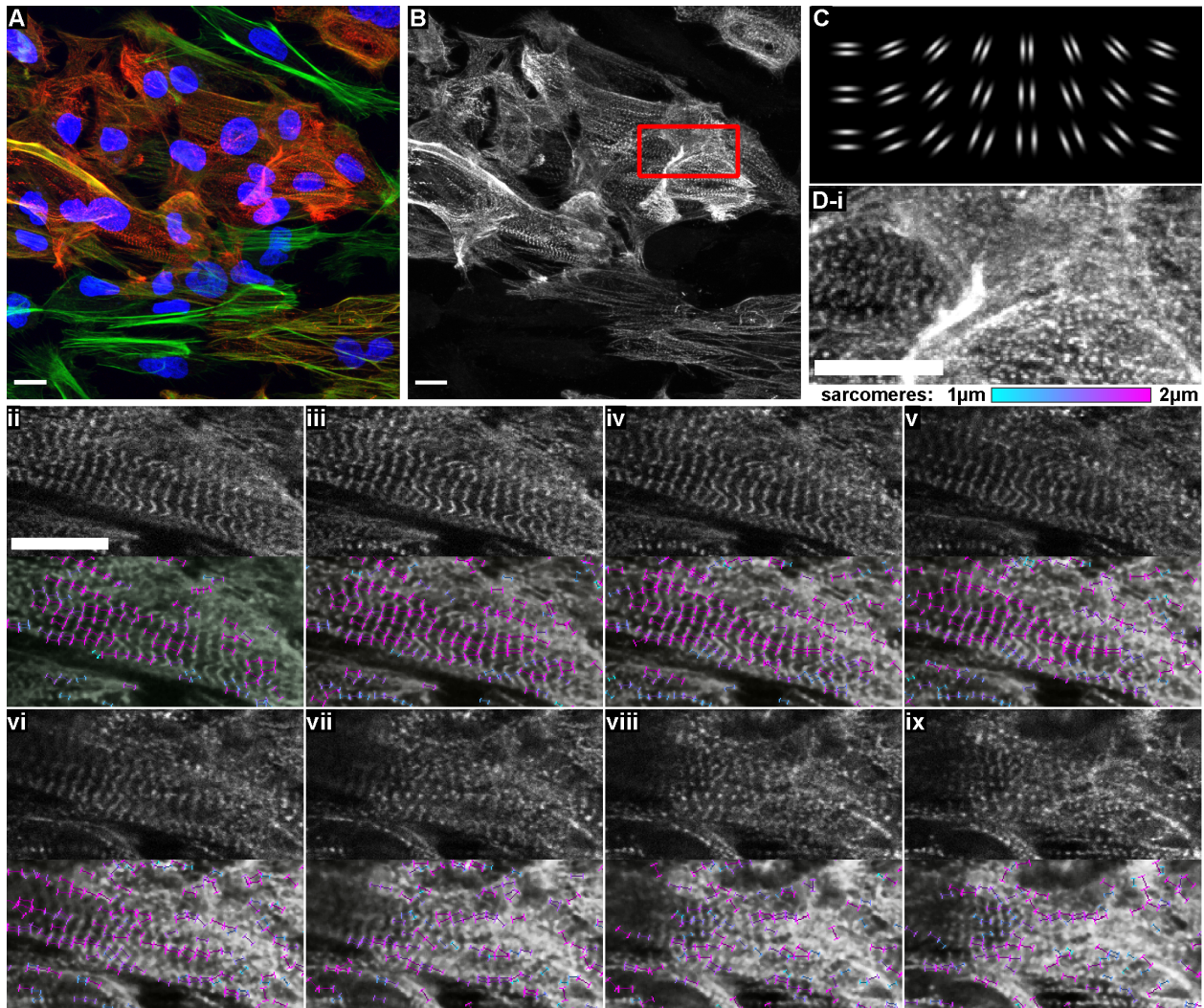
Figure 4.1: **Sarcomere analysis in z-stacks of iPSC-derived cardiac tissue.** **A**, Maximum projection of iPSC-derived cardiac tissue stained for actin fibrils (green), α-actinin (red), and nuclei (blue). **B**, Maximum projection of α-actinin. **C**, Double wavelets[1] that are convolved with each image to detect sarcomeres. **D**, (**i**) Maximum projection and (**ii-ix**) individual z-slices (**top**) with sarcomere detection results (**bottom**) of the red outlined section in **B**. The color in **ii-ix, bottom** indicates the length of the sarcomere. Scale bars: 15 μm.

4.3.2 Nuclear Segmentation

Although there is an abundance of software designed to segment nuclei in DAPI stained images[65,68–77], segmentation tools in biology generally yield nontrivial amounts of segmentation error due to assumptions in the computational design and variability in biological pheno-

types[66]. One assumption that is widespread in nuclear segmentation software, even those
designed for z-stacks, is that the nuclei will appear in a monolayer, or will not overlap in the
z-projection. This assumption does not hold and is particularly detrimental in the evalua-
tion of iPSC-derived cardiomyocytes. Therefore, we developed a computational technique to
isolate nuclei that overlap in the maximum projection of a z-stack by first segmenting each
z-slice and then grouping nuclei that appeared in multiple z-slices (Fig 4.2). The distin-
guishing aspect of this analysis was that individual nuclei that appeared in multiple z-slices
were grouped by comparing the segmentation results for each neighboring z-slice. Finally,
the maximum projection of each individual nucleus (Fig 4.2B, *bottom*) was saved after being
approved by the user. The user was required to approve the segmentation results because
it was difficult for even an expert to distinguish between highly dysmorphic, heart-shaped
nuclei and nuclei that were extremely close in the x,y, and z planes. This approach was used
by Mehrabi et al., *Submitted 2021* to evaluate the nuclei of patient specific iPSC-derived
cardiomyocytes with *LMNA* mutations.
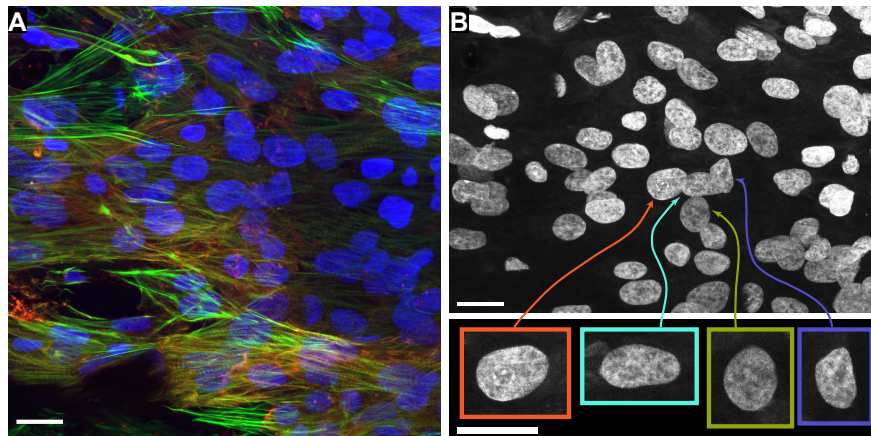
Figure 4.2: **Detection of nuclei in z-stacks of iPSC-derived cardiomyocytes. A**,
Maximum intensity projection of a z-stack stained for actin fibrils (green), α-actinin (red),
and nuclei (blue). **B**, Maximum projection of nuclei (DAPI) showing multiple overlaid nuclei
(**top**) with segmentation results (**bottom**). Scale bars: 20 µm.

4.4   Discussion and Conclusion

In this work, we designed analysis techniques to evaluate z-stacks of immature, multi-layer striated muscle tissues. Developing this analysis required overcoming two major challenges. The first was accounting for the morphology of the immature tissues, in particular, their underdeveloped sarcomeres. The occurrence of immature stress fiber and undeveloped sarcomeres was overwhelming compared to the amount of well-formed sarcomeres, which resulted in a high degree of inaccuracy in the metrics described in Chapter 1, such as sarcomere length and organization. To solve this problem we used the orientation of the actin fibrils to remove "off-target" staining, as was done in Chapter 2. The second challenge was designing a segmentation approach for multi-layer tissues, which often had overlapping cells and consequently, nuclei. Previous approaches for segmenting nuclei in stem-cell derived cardiomyocytes and other cell types was not designed for multi-layer tissues. Properly utilizing the 2.5/3D information provided by the z-slices allowed for more comprehensive segmentation results, in which nuclei that overlapped in the z-, but not x- and y- planes could be segmented. Through a combination of approaches, we were able to successfully measure sarcomere organization and the number of sarcomeres, as well as segment a majority of nuclei.

Undoubtedly, this computational approach yielded more quantitative data than was previously accessible, however there are several limitations of this analysis method, which should be addressed. First, the modified SarcTrack[1] results cannot be used to evaluate aspects of z-line architecture, such as registration, continuity, or amount of well-formed z-lines[107]. Another important limitation, is that each sarcomere is detected in a variable number of z-slices because each z-slice is analyzed independently (Fig 4.1D). To address these limitations, further aspects of SarcTrack[1] and ZlineDetection[107] could be combined in order to summarize both z-line and sarcomere architecture. Additionally, each sarcomere in the

z-stack could be reconstructed so that each sarcomere is only detected once, rather than a variable number of times.

While the nuclei segmentation circumvented the issue described for sarcomeric z-lines, and each nuclei was only detected once, the nuclear characterization is highly limited by the requirement of the user to approve or reject each grouped nucleus. However, circumventing the user-dependence will require determining how to reliably distinguish between highly dysmorphic, heart-shaped nuclei and nuclei that were extremely close in the x,y, and z planes. This could be made possible by co-staining for nuclear lamina proteins, such as lamin B[167]. In addition to removing the user dependence of the 3D nuclear segmentation, it may also be useful to expand upon the characterization of nuclear morphology developed by Core et al.[69] by adding additional shape descriptors[168]. Despite these limitations, the analysis described in this chapter is a significant step forward in quantitatively summarizing properties of cellular architecture in immature, multi-layer striated muscle tissues.

CHAPTER 5

Quantitative Evaluation of Cardiac Cell Interactions and Responses to Cyclic Strain [2]

5.1 Introduction

The ventricular myocardium is primarily composed of highly aligned cardiomyocytes, which generate the contractile force necessary for heart function[23,169]. The other predominant cell type in the myocardium is the cardiac fibroblast, which occupies space between layers of the myocardium and between cardiomyocytes, orienting along the prevailing direction of the cardiomyocytes (i.e. along the direction of contraction)[170]. In the event of myocardial infarction or cardiac diseases, there is increased migration of fibroblasts into the regions of damaged tissue as well as changes in the morphology and viability of the myocytes[171–176]. The alterations in cellular composition and structure results in disorganization and loss of efficient heart function[177–179]. In order to create accurate *in vitro* models of infarcted or diseased hearts, propose new pathways for treatment, and improve tissue engineering approaches such as cardiac patches, it is imperative to investigate the mechanisms responsible for organization in the heart, specifically the mechanisms that drive the organization of cardiomyocytes and fibroblasts and how they influence each other, which are not fully understood.

Image-based assays are a powerful experimental tool to study interactions or behavioral differences between distinct cardiac cell types[77,92,98,99,101,102,104,105,180,181]. These assays often require the development of new image processing pipelines to extract information from the images that is relevant to answering the research question[181]. Studying confluent tissues

---

[2]This work is part of a co-first author manuscript in preparation with Richard Tran.

with multiple cell types, requires analysis that accurately and reliably distinguish between the different cell types in the same image. Thus it is necessary to generate semantic segmentations of images, where each pixel or region in an image is associated with a classification corresponding to the cell type[98]. Many existing cell classification pipelines separate regions in an image based on differences in intensity and commonly make use of machine learning classifiers[77,92,98,99,101,105]. However, many of the existing classifiers do not include image features that could be used to identify striated myocytes in images. Therefore, existing computational techniques for cellular classification often cannot reliably classify which cells are striated myocyte or which image regions belong to striated myocytes.

In this chapter, we present a computational framework to automatically identify and distinguish between the two predominant cardiac cell types in images of cardiac tissues by taking advantage of the unique morphology of striated myocytes. Additionally, we demonstrate how the integration of this classifier with previously developed image-based structural assays can be used to quantify cell type specific structure to yield insights into the mechanisms underlying cellular organization in the heart.

5.2 Methods

5.2.1 Experimental Data

All experimental data was generated by Richard Tran, while in the laboratory of Anna Grosberg, Ph.D. at the University of California, Irvine.

5.2.2   Foreground/Background Segmentation

In order to distinguish between the background and foreground, manually labeled α-actinin images were entropy filtered (Fig 5.2B), standard deviation filtered (Fig 5.2C), range filtered (Fig 5.2D), and Gaussian filtered with $\sigma = 5$ (Fig 5.2E). The filtered and labels were subsampled, such that each class (i.e. "Background" and "Foreground") were equally represented in the training data, and approximately 2.5% of each image was included in training. The MATLAB function, `fitctree`, with the hyperparameters automatically optimized was used to create the classifier that had an accuracy of 95.87% for the training data.

5.2.3   Striated Myocyte Identification

Each α-actinin image was broken up into 200 "super pixels," which are groups of pixels with similar values, determined using a simple linear iterative clustering algorithm[182]. The orientation of the foreground objects was then computed after smoothing the images with a Gaussian kernel with $\sigma = 5$. Striations in the images were identified by top hat filtering the anisotropic diffusion filtered images as in Morris et al.[107][122–125]. The top hat filtered image was then binarized using adaptive thresholding. In order to isolate sarcomeric z-line striations, the orientation of the striations was compared with the object orientation, using an approach similar to that described in Morris et al.[107]. The orientation of the striations was compared with the principal orientation of the object at each super pixel by taking the dot product, and identifying striations that had a dot product value less than 0.8. Super pixel regions that were at least 10% covered in perpendicular striations were considered candidate striated myocyte regions. Additionally, to remove super pixel regions that did not contain enough striations, the top hat filtered image was binarized using global thresholding, and super pixels that consisted of less than 5% positive pixels were not considered striated myocyte regions.

5.2.4   Nuclei Segmentation and Cell Type Classification

Nuclei in DAPI stained images were segmented using the ImageJ/FIJI plugin for "StarDist"[183].
The segmented nuclei images were loaded into MATLAB and compared with the classification
labels generated for the α-actinin images. The α-actinin classification label associated
with each individual nucleus was determined based on most common (i.e. mode) classification
label that occurred within the boundary of the individual nucleus. If the most common
classification label did not account for at least a threshold proportion of the nuclear boundary, the nucleus was not considered associated with a classification label. In this analysis,
the threshold proportion was set to 0.6.

5.2.5   Cell Type Orientation Analysis

The orientation of actin at each pixel was calculated as described previously[19,46]. Briefly,
images were filtered with a Gaussian kernel and then standardized to have zero mean and
unit standard deviation[130]. The orientation was then estimated using a least mean square
orientation estimation algorithm[129,130]. Once the orientation vectors were computed for each
pixel, the results of the classifier were used to separate the actin belonging to cardiomyocytes
and fibroblasts. As described previously[36,107,131], the Orientational Order Parameter (OOP)
and principal direction (director)[184,185] of the orientation vectors, $\vec{r}(x, y)$, were quantified
from the structure tensor $\mathbb{T}$,

$$\widehat{\mathbb{T}}_i = \begin{bmatrix} r_{i,x}r_{i,x} & r_{i,x}r_{i,y} \\ r_{i,x}r_{i,y} & r_{i,y}r_{i,y} \end{bmatrix}. \tag{5.1}$$

The OOP is the maximum eigenvalue of $\mathbb{T}$ and the director is the eigenvector corresponding
to the maximum eigenvalue of tensor $\mathbb{T}$. The angle (θ) between two unit vectors, $\vec{p}$ and $\vec{q}$,

(e.g. the stretch direction and the director of either the cardiomyocye actin or the fibroblast actin) was computed by taking the inverse cosine of the dot product between the two unit vectors

$$\theta = \cos^{-1}\left(\vec{p} \cdot \vec{q}\right).$$
(5.2)

5.3 Results

The ability to quantify cell type specific structural properties required developing an image processing pipeline that accurately and reliably distinguishes between cell types that exist in the same image. The objective of this work was to separate the two dominant cell types in the ventricular myocardium, striated myocytes (Fig 5.1A-C, red outline) and fibroblasts (Fig 5.1D-F, green outline). The tissues analyzed were labeled with actin (Fig 5.1C,F), which appears in both cell types, as well as α-actinin, which only occurs in striated myocytes (Fig 5.1B,E). However, identifying mature or well-formed striated myocytes required not only recognizing the presence of a striated myocyte-specific stain (e.g. α-actinin), but also examining the structures (i.e. sarcomeres) visualized by that stain (Fig 5.1A-C, red outline). This was further complicated by qualitative observations of cells that were positive for the sarcomeric protein, α-actinin, but did not have any sarcomere striations (Fig 5.1A-C, cyan outline). As the phenotype of the cells with α-actinin, but no sarcomeric striations could not be clearly identified as fibroblasts or striated myocytes, we designated three semantic classes, "Fibroblast", "Striated Myocyte", and "Other" (Table 5.1), in addition to the background.

Table 5.1: Description of semantic classes.

Class	α-actinin Description	Actin Description
Fibroblast	no α-actinin	actin fibrils
Striated Myocyte	α-actinin sarcomere striations	actin fibrils
Other	α-actinin, but no sarcomere striations	actin fibrils
Background	no α-actinin	no actin fibrils
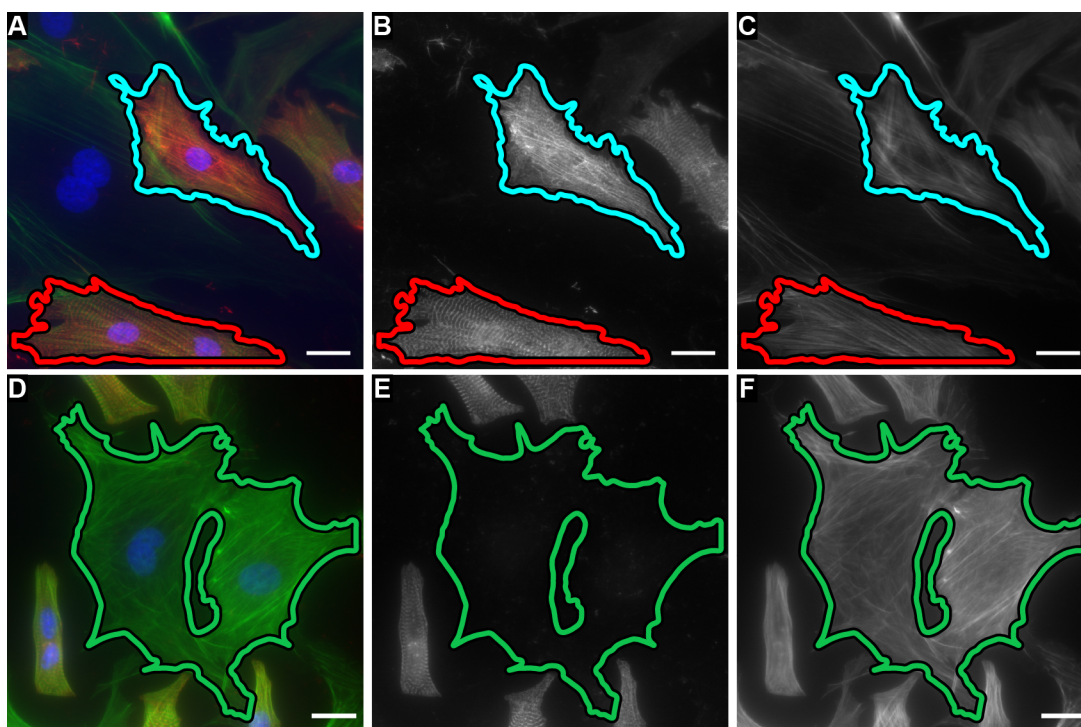
Figure 5.1: **Distinct Cardiac Cell Types. A**, Image stained for actin fibrils (green), α-actinin (red), and nuclei (blue) with the "Striated Myocyte" outlined in red and "Other" outlined in cyan. **B**, Grayscale α-actinin image as in A with "Striated Myocyte" outlined in red and "Other" outlined in cyan. **C**, Grayscale actin image as in A with "Striated Myocyte" outlined in red and "Other" outlined in cyan. **D**, Image stained for actin fibrils (green), α-actinin (red), and nuclei (blue) with the "Fibroblast" outlined in green. **E**, Grayscale α-actinin image as in D with the "Fibroblast" outlined in green. **F**, Grayscale actin image as in D with the "Fibroblast" outlined in green. Scale bars: 20 µm.

The first step of the image classification was distinguishing objects from the background, which was challenging due to the amount imaging artifacts visible in the background. Thus, we segmented cells from the background in α-actinin labeled images (Fig 5.2A) by classifying each pixel as "background" or "foreground" based on their entropy filtered (Fig 5.2B), standard deviation filtered (Fig 5.2C), range filtered (Fig 5.2D), and Gaussian filtered (Fig 5.2E) features using a trained classification decision tree. The result of the foreground / background segmentation (Fig 5.2F) served two purposes. Because fibroblasts do not contain any α-actinin (Fig 5.1E), only actin that was classified as "background" in the α-actinin image classification could be attributed to fibroblasts. Subsequently, the regions that were classified as "foreground" needed to be classified as either "Striated Myocyte" or "Other"

(Table 5.1).
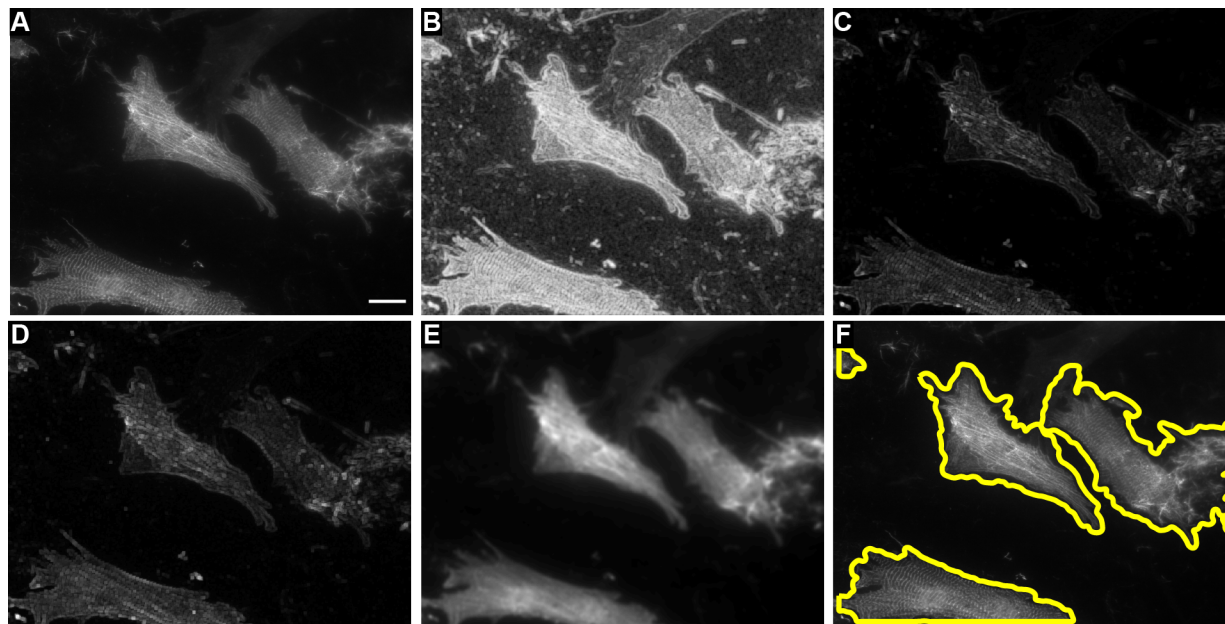
Figure 5.2: **Foreground / Background Segmentation. A**, Image stained for α-actinin.
Entropy filtered (**B**), standard deviation filtered (**C**), range filtered (**D**), and Gaussian filtered
(**E**) α-actinin image as in A. **F**, Segmented cells plotted in yellow on top of the image stained
for α-actinin Scale bar: 20 μm.

One facet of distinguishing between 'Striated Myocytes" and "Other" is the spatial or statis-
tical distribution of their intensity (i.e. image texture)[100], as striated myocytes are charac-
terized by distinct striations, where the "Other" cells had more uniform intensity. However,
this was not always the case, as many of the "Other" cells appeared to be composed entirely
of stress fibers, and thus also had bright continuous, linear structures (Fig 5.1B, cyan). The
key difference between α-actinin sarcomeric striations and the α-actinin structures belonging
to stress fibers, is their length and orientation relative to the orientation of the cell, or more
accurately, the orientation relative to the stress or myofibrils of the cells. Thus, attempts
at using only the image texture to distinguish between "Striated Myocytes" and "Other"
using both supervised and unsupervised[77,181] classification, yielded a non-trivial amount of
misclassification.

Classification of foreground image regions as either "Striated Myocyte" or "Other" was
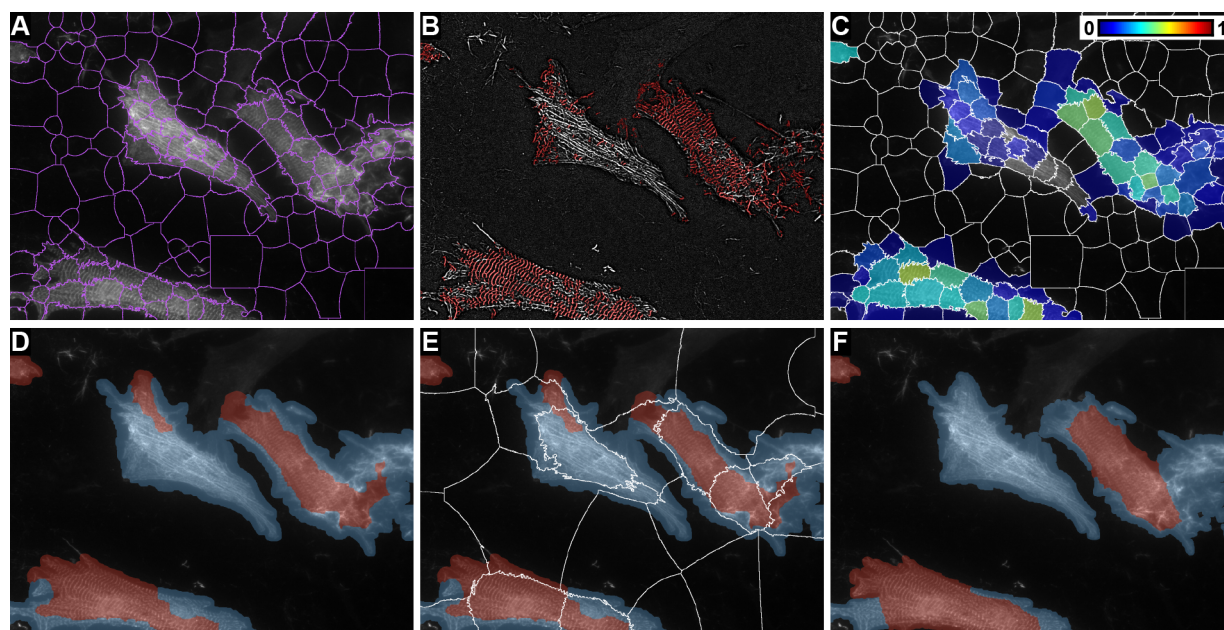
Figure 5.3: Identification of Cardiomyocyte Regions. **A**, Image stained for α-actinin overlaid with the super pixel regions in purple. **B**, Anisotropic diffusion and top hat filtered α-actinin images, with perpendicular striations shaded in red. **C**, Number of perpendicular striations divided by the total number of pixels in each super pixel region **A**,. Super pixels are outlined in white, **D**, Regions in C that are above a threshold are colored red and considered "Striated Myocytes." Cyan regions do not meet this threshold and are considered "Other." **E**, Re-clustered super pixel regions are overlayed in white on top of the α-actinin image. **F**, The final "Striated Myocyte" (red) and "Other" (cyan) classification.

achieved through a combination of multiple image processing approaches. First, the images were broken up into "super pixels", which are groups of pixels that have similar values[182] (Fig 5.3A). Using this approach reduced the complexity of the classification problem, as 200 "super pixels" rather than over one million pixels needed to be correctly classified. In order to correctly classify image regions, we defined the aspects of cellular morphology that experts use to identify striated myocytes. One of the most important considerations in this context, is that striated myocytes in α-actinin stained images will have sarcomeric z-lines that are oriented parallel to at least one other z-line approximately 2 µm away, as well as oriented perpendicular to the direction of the myofibril[54]. Additionally at the imaging resolution of this data, regions belonging to striated myocytes will have bright striations that are approximately 1-3 pixels wide and surrounded by other bright striations that are orientated

along the same direction. These biological and experimental features were incorporated into a processing pipeline that first enhances and detects edges using anisotropic diffusion and top hat filtering (Fig 5.3B) as was done in Chapters 2, 3. The direction of the myofibril or stress fibrils was approximate by the principal direction of the cell, which was calculated once the images were convolved with a Gaussian kernel that sufficiently blurred 1-3 pixel wide striations. Subsequently, the edges (i.e. bright striations) that were approximately perpendicular to the principal direction of the cell in a super pixel region were identified (Fig 5.3B, red). In order to account for the striated myocyte attribute that a sarcomeric z-line should be parallel to at least one other z-line, the total number of perpendicular edges in each super pixel region were counted and those below a threshold were not considered "Striated Myocyte" (Fig 5.3C). This approach successfully captured many of the image regions that contained sarcomeric z-lines (Fig 5.3D). In order to avoid isolated regions of classification, the images were re-clustered with a smaller number of super pixels, and the class of each super pixel was set to the most common label in that region (Fig 5.3E,F).

To demonstrate the utility of this work, the classified α-actinin images (Fig 5.4A) are being used in ongoing research to distinguish actin belonging to fibroblasts from that belonging to cardiomyocytes in order to measure their individual responses to induced mechanical stimulation. Once the actin orientation vectors are grouped according to their classification (Fig 5.4F), the principal direction (i.e. director) and the spread in the distribution of the orientation vectors, also known as the orientational order parameter (OOP), were quantified (See Methods Section 5.2.5 for more information). Thus, with the cell type specific director and the OOP, the predominant orientation of each cell type and the alignment between different cell types can be quantified (Table 5.2).
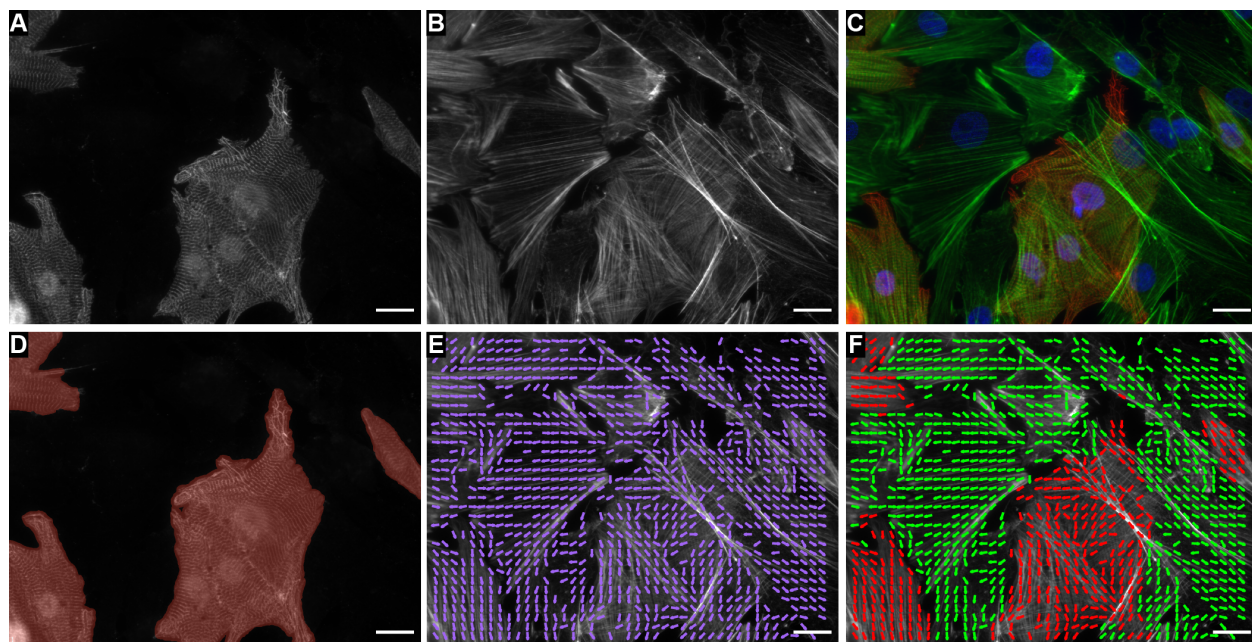
Figure 5.4: Co-culture of cardiomyocytes and fibroblasts labeled with (A) α-actinin, (B) actin, and (C) α-actinin (red), actin (green), and DAPI (blue). **D**, Cells classified as mature cardiomyocytes are shaded red in the α-actinin labeled image shown in A. **E**, The orientation of actin at each pixel is plotted as a purple arrow on top of the actin labeled image shown in B. **F**, The orientation of actin at each pixel as shown in B, but colored red for cardiomyocytes and green for fibroblasts. Scale bars: 20 µm.

Table 5.2: Cell type specific actin organization for the image in Fig 5.4.

Actin Label	Director	OOP
All Actin	24 °	0.20
Cardiomyocyte Only	72 °	0.27
Fibroblast Only	12 °	0.34

5.4   Discussion and Conclusion

In this work, we developed a computational approach to classify image regions according to their cell type. A significant challenge in this work was determining how to identify and classify regions that contained a sarcomere specific protein, α-actinin, but did not have any sarcomeric striations. We approached this problem by performing image processing that emphasized the differences between sarcomeric and non-sarcomeric regions, such as the relative occurrence and orientation of the striations. Through amalgamating the classification

with existing analysis pipelines, it is now possible to compare structural properties among different cell types. One important application is the quantification of cell type organization, which has provided insight into the mechanisms underlying cellular organization in the heart.

While this analysis protocol can be used to quantify cell type specific morphology in tissues comprised of multiple cell types, there are several limitations and opportunities for improvement. A significant limitation is the simplification of the semantic classes for the α-actinin images (i.e. "Striated Myocyte" or "Other"). One hypothesis is that the cells with α-actinin, but no identifiable sarcomeric striations may be myocytes in an earlier stage of myofibrillogenesis. Therefore, it would be interesting to integrate cellular morphological information and gene expression data to more fully characterize the developmental stage or state of the cells as was done by Gerbin et al.[186] in stem cell derived cardiomyocytes. A separate limitation is that in regions where cells overlap, it is not possible to accurately distinguish between them. Appropriately rectifying overlapping cells would require imaging using a 3D imaging modality, such as acquiring serial optical sections. Similarly, without the use of membrane stains, it is not possible to isolate individual cells. Therefore, image regions were classified rather than segmenting individual cells and then classifying them. A potential drawback of this approach is that the classifier is prone to partitioning what appears to be the same cell into regions with different labels. While possible that these are misclassifications caused by imaging noise or the simplistic nature of the classifier, in many cases it is also possible that the classifier is correctly identifying variability in the sarcomere formation within the same cell. Through the use of additional stains, such as a cell membrane stain, it may be possible to segment individual cells and assign each cell with a semantic class. However, it is vital to balance accounting for true biological variability within a cell as well as noise and variability in image quality. Lastly, the image classification could be improved by using a more sophisticated classification approach, such as incorporating additional experimental information and deep learning. Notwithstanding these limitations, this approach to cardiac cell type classification will bolster work that involves cardiac tissues with multiple cell types.

CHAPTER 6

Future Directions and Conclusion

This dissertation was devoted to discussing and addressing some of the unique challenges and importance of characterizing the morphology of striated myocytes. A computational image analysis approach was utilized to overcome these challenges, while prioritizing the specific biological and physiological considerations of striated myocytes. While multiple novel computational tools and metrics that more fully characterize striated myocytes were developed as a part of this work, there are a variety of ways in which the work can be expanded upon and improved.

6.1 Additional Metrics

6.1.1 Z-line Registration

While the computational methods we developed in Chapter 2 to measure continuous sarcomere striation lengths successfully characterized skeletal myofibers from mice in Chapter 3, the applicability of striation continuity as a metric in engineered tissue is limited (Chapter 2). A difference in striation continuity length could not account for functional differences between engineered isotropic and anisotropic tissues or single cells with constant area, but variable aspect ratios[107]. In order to more successfully predicted contractile stresses in engineered tissues, it may be necessary to incorporate a metric that captures the degree of z-line registration, rather than z-line continuity, into existing models of contractile function[21]. Adaptation of the smectic order parameter from liquid crystals[21] or measuring the decay of the Haralick Correlation as a function of offset distance[24,187] could be used to quantify z-line registration,

which may be crucial in producing more accurate predictions of engineered tissue contractile function.

6.1.2 Nuclear Shape Descriptors and Cell Type

A significant contribution of the work discussed in Chapter 4 was the development of a nuclear segmentation approach that utilized multiple z-slices. The nuclear segmentation was a means to investigate the pathological effects of mutations in the Lamin A/C (*LMNA*) gene in patient-specific iPSC-derived cardiomyocytes. Mehrabi et al., *Submitted 2021* demonstrated that it may be important to not only identify nuclear defects as was done by Core et al. [69], but also determine the severity of the deformation. Expanding nuclear morphology assessment to better characterize malformations through the use of additional shape descriptors[79–81,188,189] could yield more insight into the morphological changes in cardiomyocytes from patients with *LMNA* mutations. Additionally, to more fully characterize nuclear morphology, it may be beneficial to evaluate the cytoskeletal architecture surrounding each nuclei and determine the cell type or cell state to which a nucleus belongs by adapting the classifier discussed in Chapter 5 to nuclei and z-stacks.

6.1.3 3D Actin Orientational Order Parameter

In Chapter 4, the orientational order of actin in z-stacks was calculated by pooling the 2D actin orientation vectors in each z-slice and calculating the OOP of the pooled data. However, because the actin cytoskeleton ensures the structural and mechanical integrity of cells[190] and is essential to the mechanosensitivity and mechanical response of adhering cells to their environment[191–194], it may be important to characterize 3D actin organization. Actin organization in 3D could be measured by computing a 3D orientation vector for each pixel, and then using the 3D nematic order parameter (3D OOP) to quantify the organization.

6.2 Improved Segmentation

A crucial component of the work described in Chapters 2, 3, and 4 was segmentation of cellular constructs, such as sarcomeric striations and nuclei. The image processing pipelines utilized biological information about the constructs in order to overcome limitations in image resolution and quality as well as the availability or specificity of fluorescent stains. For example, in Chapter 2, the α-actinin belonging to z-lines was isolated from that belonging to immature stress fibers by comparing the orientation of α-actinin relative to actin. In this example, the segmentation falters when cells are not organized in a mono-layer and actin from different cells overlaps. Therefore, to improve segmentation, it is necessary to image multi-layer tissues using 3D imaging modalities as was done in Chapter 4.

A significant challenge in the analysis of z-stacks, is reconciling constructs that appear in multiple slices, especially when the constructs have immature or irregular morphology. Segmentation of the extremely dysmorphic and overlapping nuclei described in Chapter 4, could be greatly improved through staining for and comparing multiple different structures, such as DAPI and lamin b. Similarly, in addition to incorporating different image processing techniques or deep learning, segmentation of sarcomeric z-lines in z-stacks could be improved by comparing co-localization of multiple sarcomeric proteins, such as titin and α-actinin or α-actinin and myosin. Incorporating of additional biological information could also be used to improve the cell type classifier described in Chapter 5.

6.3 Increased Accessibility

A final improvement would be increased accessibility of this work. One of the issues plaguing bio-image analysis is the lack of code maintenance, public accessibility, and ease of use to new users[106,195]. While much of the software described in this work is publicly available on a

software hosting website, Github, it was developed in MATLAB, which is a paid software and thus not accessible to everyone. Additionally, it is not currently compatible with popular bio-image analysis software, such as ImageJ[196–198] and CellProfiler[75,76,199], which many research groups have incorporated into their analysis routines. While we dedicated a lot of energy into writing comprehensive documentation and making the software user-friendly through graphical user interfaces, these limitations hinder widespread adaption of the metrics and image processing pipelines presented in this work.

6.4 Conclusion

The totality of this dissertation is a suite of metrics and image processing pipelines that have and will contribute to a deeper understanding of the biology of striated myocytes. In Chapter 2, we were able to determine that highly elongated striated myocytes have less sarcomeric z-lines, which may account for the diminished contractile function at this aspect ratio. The approaches described in Chapters 3 and 4, are actively being used to investigate pathological and developmental differences in mouse skeletal myofibers and patient-specific stem-cell derived cardiomyocytes, respectively. Additionally, the classifier in Chapter 5 is currently being used to quantify the interactions and responses of different cardiac cell types to mechanical stimulation. We believe that these and future insights into striated myocyte biology made possible through the use of computational techniques, will positively impact our ability to build better engineered tissues, as well as models of aging and disease.

Bibliography

[1] Christopher N Toepfer, Arun Sharma, Marcelo Cicconet, Amanda C Garfinkel, Michael Mücke, Meraj Neyazi, Jon AL Willcox, Radhika Agarwal, Manuel Schmid, Jyoti Rao, et al. Sarctrack: an adaptable software tool for efficient large-scale analysis of sarcomere function in hipsc-cardiomyocytes. *Circulation research*, 124(8):1172–1183, 2019.

[2] E. Ehler, B.M. Rothen, S.P. Hammerle, M. Komiyama, and J.C. Perriard. Myofibrillogenesis in the developing chicken heart: assembly of z-disk, m-line and the thick filaments. *Journal of Cell Science*, 112(10):1529–1539, 1999. ISSN 0021-9533. doi: 10/1529.

[3] Joseph W Sanger, Joseph C Ayoob, Prokash Chowrashi, Daniel Zurawski, and Jean M Sanger. Assembly of myofibrils in cardiac muscle cells. In *Elastic Filaments of the Cell*, pages 89–110. Springer, 2000.

[4] Sean P Sheehy, Francesco Pasqualini, Anna Grosberg, Sung Jin Park, Yvonne Aratyn-Schaus, and Kevin Kit Parker. Quality metrics for stem cell-derived cardiac myocytes. *Stem cell reports*, 2(3):282–294, 2014.

[5] Lisa M Larkin, Sarah Calve, Tatiana Y Kostrominova, and Ellen M Arruda. Structure and functional evaluation of tendon–skeletal muscle constructs engineered in vitro. *Tissue engineering*, 12(11):3149–3158, 2006.

[6] Nancy K Drew, Mackenzie A Eagleson, Danny B Baldo Jr, Kevin Kit Parker, and Anna Grosberg. Metrics for assessing cytoskeletal orientational correlations and consistency. *PLoS computational biology*, 11(4):e1004190, 2015.

[7] Francesco Silvio Pasqualini, Sean Paul Sheehy, Ashutosh Agarwal, Yvonne Aratyn-Schaus, and Kevin Kit Parker. Structural phenotyping of stem cell-derived cardiomyocytes. *Stem cell reports*, 4(3):340–347, 2015.

[8] Alexandre JS Ribeiro, Yen-Sin Ang, Ji-Dong Fu, Renee N Rivas, Tamer MA Mohamed, Gadryn C Higgs, Deepak Srivastava, and Beth L Pruitt. Contractility of single cardiomyocytes differentiated from pluripotent stem cells depends on physiological shape and substrate stiffness. *Proceedings of the National Academy of Sciences*, 112(41): 12705–12710, 2015.

[9] Nancy K Drew, Nicholas E Johnsen, Jason Q Core, and Anna Grosberg. Multiscale characterization of engineered cardiac tissue architecture. *Journal of biomechanical engineering*, 138(11):111003, 2016.

[10] Jutta Schaper, R Froede, A Buck, and N Bleese. Impaired myocardial ultrastructure and cytoskeleton in cardiomyopathic human myocardium. In *New concepts in viral heart disease*, pages 295–302. Springer, 1988.

[11] Gloria M Conover, Syerra N Henderson, and Carol C Gregorio. A myopathy-linked desmin mutation perturbs striated muscle actin filament architecture. *Molecular biology of the cell*, 20(3):834–845, 2009.

[12] Anasuya Gupta, Sudhiranjan Gupta, David Young, Biswajit Das, James McMahon, and Subha Sen. Impairment of ultrastructure and cytoskeleton during progression of cardiac hypertrophy to heart failure. *Laboratory Investigation*, 90(4):520, 2010.

[13] Gang Wang, Megan L McCain, Luhan Yang, Aibin He, Francesco Silvio Pasqualini, Ashutosh Agarwal, Hongyan Yuan, Dawei Jiang, Donghui Zhang, Lior Zangi, et al. Modeling the mitochondrial cardiomyopathy of Barth syndrome with induced pluripotent stem cell and heart-on-chip technologies. *Nature medicine*, 20(6):616, 2014.

[14] RB Armstrong, RW Ogilvie, and JA Schwane. Eccentric exercise-induced injury to rat skeletal muscle. *Journal of Applied Physiology*, 54(1):80–93, 1983.

[15] J Friden, M Sjöström, and B Ekblom. Myofibrillar damage following intense eccentric exercise in man. *International journal of sports medicine*, 4(03):170–176, 1983.

[16] SA Wood, DL Morgan, and U Proske. Effects of repeated eccentric contractions on structure and mechanical properties of toad sartorius muscle. *American Journal of Physiology-Cell Physiology*, 265(3):C792–C800, 1993.

[17] CD Balnave, DF Davey, and DG Allen. Distribution of sarcomere length and intracellular calcium in mouse skeletal muscle following stretch-induced injury. *The Journal of Physiology*, 502(3):649–659, 1997.

[18] Kimberly R Doherty, Dominique R Talbert, Patricia B Trusk, Diarmuid M Moran, Scott A Shell, and Sarah Bacus. Structural and functional screening in human induced-pluripotent stem cell-derived cardiomyocytes accurately identifies cardiotoxicity of multiple drug types. *Toxicology and applied pharmacology*, 285(1):51–60, 2015.

[19] Adam W Feinberg, Patrick W Alford, Hongwei Jin, Crystal M Ripplinger, Andreas A Werdich, Sean P Sheehy, Anna Grosberg, and Kevin Kit Parker. Controlling the contractile strength of engineered cardiac muscle by hierarchal tissue architecture. *Biomaterials*, 33(23):5732–5741, 2012.

[20] Meghan B Knight, Nancy K Drew, Linda A McCarthy, and Anna Grosberg. Emergent global contractile force in cardiac tissues. *Biophysical journal*, 110(7):1615–1624, 2016.

[21] K Dasbiswas, S Majkut, DE Discher, and Samuel A Safran. Substrate stiffness-modulated registry phase correlations in cardiomyocytes map structural order to coherent beating. *Nature communications*, 6:6085, 2015.

[22] Kathleen A Clark, Abigail S McElhinny, Mary C Beckerle, and Carol C Gregorio. Striated muscle cytoarchitecture: an intricate web of form and function. *Annual review of cell and developmental biology*, 18(1):637–706, 2002.

[23] Meghan B Knight, Anna Grosberg, and Megan L McCain. In vitro tools for quantifying structure–function relationships in cardiac myocyte cells and tissues. In *Cardiac Cytoarchitecture*, pages 15–39. Springer, 2015.

[24] Matthew D Sutcliffe, Philip M Tan, Antonio Fernandez-Perez, Young-Jae Nam, Nikhil V Munshi, and Jeffrey J Saucerman. High content analysis identifies unique morphological features of reprogrammed cardiomyocytes. *Scientific reports*, 8(1):1258, 2018.

[25] Jonathan Guy Bensley, Robert De Matteo, Richard Harding, and Mary Jane Black. Three-dimensional direct measurement of cardiomyocyte volume, nuclearity, and ploidy in thick histological sections. *Scientific reports*, 6(1):1–10, 2016.

[26] Antoni Oliver-Gelabert, Laura García-Mendívil, José María Vallejo-Gil, Pedro Carlos Fresneda-Roldán, Katarína Andelová, Javier Fañanás-Mastral, Manuel Vázquez-Sancho, Marta Matamala-Adell, Fernando Sorribas-Berjón, Carlos Ballester-Cuenca, et al. Automatic quantification of cardiomyocyte dimensions and connexin 43 lateralization in fluorescence images. *Biomolecules*, 10(9):1334, 2020.

[27] Po-Ling Kuo, Hyungsuk Lee, Mark-Anthony Bray, Nicholas A Geisse, Yen-Tsung Huang, William J Adams, Sean P Sheehy, and Kevin K Parker. Myocyte shape regulates lateral registry of sarcomeres and contractility. *The American journal of pathology*, 181(6):2030–2037, 2012.

[28] A Martin Gerdes. Cardiac myocyte remodeling in hypertrophy and progression to failure. *Journal of cardiac failure*, 8(6):S264–S268, 2002.

[29] A Martin Gerdes and Joseph M Capasso. Structural remodeling and mechanical dysfunction of cardiac myocytes in heart failure. *Journal of molecular and cellular cardiology*, 27(3):849–856, 1995.

[30] A Martin Gerdes, Scott E Kellerman, Jo Ann Moore, Karl E Muffly, Linda C Clark, Phyllis Y Reaves, Krystyna B Malec, Peter P McKeown, and Douglas D Schocken. Structural remodeling of cardiac myocytes in patients with ischemic cardiomyopathy. *Circulation*, 86(2):426–430, 1992.

[31] Zoe Anne McCrossan, Rudolf Billeter, and Ed White. Transmural changes in size, contractile and electrical properties of SHR left ventricular myocytes during compensated hypertrophy. *Cardiovascular research*, 63(2):283–292, 2004.

[32] Ken-ichi Sawada and Keishiro Kawamura. Architecture of myocardial cells in human cardiac ventricles with concentric and eccentric hypertrophy as demonstrated by quantitative scanning electron microscopy. *Heart and vessels*, 6(3):129–142, 1991.

[33] J Robbins. Diseases of the cytoskeleton: The desminopathies. *Cardioskeletal Myopathies in Children and Young Adults*, pages 173–192, 2017.

[34] MH Stromer. The cytoskeleton in skeletal, cardiac and smooth muscle cells. 1998.

[35] Joseph W Sanger, Jushuo Wang, Yingli Fan, Jennifer White, and Jean M Sanger. Assembly and dynamics of myofibrils. *BioMed Research International*, 2010, 2010.

[36] Anna Grosberg, Po-Ling Kuo, Chin-Lin Guo, Nicholas A Geisse, Mark-Anthony Bray, William J Adams, Sean P Sheehy, and Kevin Kit Parker. Self-organization of muscle cell structure and function. *PLoS computational biology*, 7(2):e1001088, 2011.

[37] N Gustavo Pérez, Katsuji Hashimoto, Sylvia McCune, Ruth A Altschuld, and Eduardo Marbán. Origin of contractile dysfunction in heart failure: calcium cycling versus myofilaments. *Circulation*, 99(8):1077–1083, 1999.

[38] Jutta Schaper, R Froede, ST Hein, A Buck, H Hashizume, B Speiser, A Friedl, and N Bleese. Impairment of the myocardial ultrastructure and changes of the cytoskeleton in dilated cardiomyopathy. *Circulation*, 83(2):504–514, 1991.

[39] Giovanni Benard, Benjamin Faustin, Emilie Passerieux, Anne Galinier, Christophe Rocher, Nadege Bellance, J-P Delage, Louis Casteilla, Thierry Letellier, and Rodrigue Rossignol. Physiological diversity of mitochondrial oxidative phosphorylation. *American Journal of Physiology-Cell Physiology*, 291(6):C1172–C1182, 2006.

[40] Nisha M Ramdas and GV Shivashankar. Cytoskeletal control of nuclear morphology and chromatin organization. *Journal of molecular biology*, 427(3):695–706, 2015.

[41] Faqian Li, Xuejun Wang, and A Martin Gerdes. Formation of binucleated cardiac myocytes in rat heart: Ii. cytoskeletal organisation. *Journal of molecular and cellular cardiology*, 29(6):1553–1565, 1997.

[42] Mark-Anthony P Bray, William J Adams, Nicholas A Geisse, Adam W Feinberg, Sean P Sheehy, and Kevin K Parker. Nuclear morphology and deformation in engineered cardiac myocytes and tissues. *Biomaterials*, 31(19):5143–5150, 2010.

[43] Jan Lammerding. Mechanics of the nucleus. *Comprehensive physiology*, 1(2):783–807, 2011.

[44] Renu Vishavkarma, Swetavalli Raghavan, Chandrashekar Kuyyamudi, Abhijit Majumder, Jyotsna Dhawan, and Pramod A Pullarkat. Role of actin filaments in correlating nuclear shape and cell spreading. *PloS one*, 9(9):e107895, 2014.

[45] Nikhil Jain, K Venkatesan Iyer, Abhishek Kumar, and GV Shivashankar. Cell geometric constraints induce modular gene-expression patterns via redistribution of hdac3 regulated by actomyosin contractility. *Proceedings of the National Academy of Sciences*, 110(28):11349–11354, 2013.

[46] Anna Grosberg, Patrick W Alford, Megan L McCain, and Kevin Kit Parker. Ensembles of engineered cardiac tissues for physiological and pharmacological study: heart on a chip. *Lab on a chip*, 11(24):4165–4173, 2011.

[47] JianGuo Sun, Jian Tang, and JianDong Ding. Cell orientation on a stripe-micropatterned surface. *Chinese Science Bulletin*, 54(18):3154–3159, 2009.

[48] Akinori Umeno and Shoogo Ueno. Quantitative analysis of adherent cell orientation influenced by strong magnetic fields. *IEEE transactions on nanobioscience*, 2(1):26–28, 2003.

[49] Dmitri Volfson, Scott Cookson, Jeff Hasty, and Lev S Tsimring. Biomechanical ordering of dense cell populations. *Proceedings of the National Academy of Sciences*, 105(40): 15346–15351, 2008.

[50] Ian W Hamley. *Introduction to soft matter: synthetic and biological self-assembling materials.* John Wiley & Sons, 2013.

[51] Qingda Hu, Tessa Altair Morris, Anna Grosberg, Alex J Levine, and Elliot L Botvinick. Actively driven fluctuations in a fibrin network. *Frontiers in Physics*, 8:653, 2021.

[52] Pieter P de Tombe and Henk EDJ ter Keurs. Cardiac muscle mechanics: sarcomere length matters. *Journal of molecular and cellular cardiology*, 91:148–150, 2016.

[53] Daria Amiad Pavlov and Amir Landesberg. The cross-bridge dynamics is determined by two length-independent kinetics: Implications on muscle economy and frank–starling law. *Journal of molecular and cellular cardiology*, 90:94–101, 2016.

[54] Joseph W Sanger, Jushuo Wang, Beth Holloway, Aiping Du, and Jean M Sanger. Myofibrillogenesis in skeletal muscle cells in zebrafish. *Cell motility and the cytoskeleton*, 66(8):556–566, 2009.

[55] Côme Pasqualin, François Gannier, Angèle Yu, Claire O Malécot, Pierre Bredeloux, and Véronique Maupoil. Sarcoptim for imagej: high-frequency online sarcomere length computing on stimulated cardiomyocytes. *American Journal of Physiology-Cell Physiology*, 311(2):C277–C283, 2016.

[56] Kenneth S Campbell. Interactions between connected half-sarcomeres produce emergent mechanical behavior in a mathematical model of muscle. *PLoS computational biology*, 5(11):e1000560, 2009.

[57] Benjamin M Friedrich, Amnon Buxboim, Dennis E Discher, and Samuel A Safran. Striated acto-myosin fibers can reorganize and register in response to elastic interactions with the matrix. *Biophysical journal*, 100(11):2706–2715, 2011.

[58] Anthony G Rodriguez, Sangyoon J Han, Michael Regnier, and Nathan J Sniadecki. Substrate stiffness increases twitch power of neonatal cardiomyocytes in correlation with changes in myofibril structure and intracellular calcium. *Biophysical journal*, 101 (10):2455–2464, 2011.

[59] Stephanie Majkut, Timon Idema, Joe Swift, Christine Krieger, Andrea Liu, and Dennis E Discher. Heart-specific stiffening in early embryos parallels matrix and myosin expression to optimize beating. *Current Biology*, 23(23):2434–2439, 2013.

[60] Nils Hersch, Benjamin Wolters, Georg Dreissen, Ronald Springer, Norbert Kirchgeßner, Rudolf Merkel, and Bernd Hoffmann. The constant beat: cardiomyocytes adapt their forces by equal contraction upon environmental stiffening. *Biology open*, page BIO20133830, 2013.

[61] Kinjal Dasbiswas, Shiqiong Hu, Frank Schnorrer, Samuel A Safran, and Alexander D Bershadsky. Ordering of myosin II filaments driven by mechanical forces: experiments and theory. *Philosophical Transactions of the Royal Society B: Biological Sciences*, 373 (1747):20170114, 2018.

[62] Michel Sam, Sameer Shah, Jan Fridén, Derek J Milner, Yassemi Capetanaki, and Richard L Lieber. Desmin knockout muscles generate lower stress and are less vulnerable to injury compared with wild-type muscles. *American Journal of Physiology-Cell Physiology*, 279(4):C1116–C1122, 2000.

[63] Kazuaki Tokunaga, Noriko Saitoh, Ilya G Goldberg, Chiyomi Sakamoto, Yoko Yasuda, Yoshinori Yoshida, Shinya Yamanaka, and Mitsuyoshi Nakao. Computational image analysis of colony and nuclear morphology to evaluate human induced pluripotent stem cells. *Scientific reports*, 4:6996, 2014.

[64] Paola Scaffidi and Tom Misteli. Lamin a-dependent nuclear defects in human aging. *Science*, 312(5776):1059–1063, 2006.

[65] Fuyong Xing and Lin Yang. Robust nucleus/cell detection and segmentation in digital pathology and microscopy images: a comprehensive review. *IEEE reviews in biomedical engineering*, 9:234–263, 2016.

[66] Juan C Caicedo, Jonathan Roth, Allen Goodman, Tim Becker, Kyle W Karhohs, Matthieu Broisin, Csaba Molnar, Claire McQuin, Shantanu Singh, Fabian J Theis, et al. Evaluation of deep learning strategies for nucleus segmentation in fluorescence images. *Cytometry Part A*, 95(9):952–965, 2019.

[67] Juan C Caicedo, Allen Goodman, Kyle W Karhohs, Beth A Cimini, Jeanelle Ackerman, Marzieh Haghighi, CherKeng Heng, Tim Becker, Minh Doan, Claire McQuin, et al. Nucleus segmentation across imaging experiments: the 2018 data science bowl. *Nature methods*, 16(12):1247–1253, 2019.

[68] Massimo Salvi, Umberto Morbiducci, Francesco Amadeo, Rosaria Santoro, Francesco Angelini, Isotta Chimenti, Diana Massai, Elisa Messina, Alessandro Giacomello, Maurizio Pesce, et al. Automated segmentation of fluorescence microscopy images for 3d cell detection in human-derived cardiospheres. *Scientific reports*, 9(1):1–11, 2019.

[69] Jason Q Core, Mehrsa Mehrabi, Zachery R Robinson, Alexander R Ochs, Linda A McCarthy, Michael V Zaragoza, and Anna Grosberg. Age of heart disease presentation and dysmorphic nuclei in patients with LMNA mutations. *PloS one*, 12(11):e0188256, 2017.

[70] Oranit Boonsiri, Kiyotada Washiya, Kota Aoki, and Hiroshi Nagahashi. 3d gray level co-occurrence matrix based classification of favor benign and borderline types in follicular neoplasm images. *Journal of Biosciences and Medicines*, 4(03):51, 2016.

[71] Arkadiusz Gertych, Zhaoxuan Ma, Jian Tajbakhsh, Adriana Velásquez-Vacca, and Beatrice S. Knudsen. Rapid 3-d delineation of cell nuclei for high-content screening platforms. *Computers in Biology and Medicine*, 69:328 – 338, 2016. ISSN 0010-4825. doi: 10.1016/j.compbiomed.2015.04.025. URL `http://www.sciencedirect.com/science/article/pii/S0010482515001432`.

[72] Gang Lin, Umesh Adiga, Kathy Olson, John F Guzowski, Carol A Barnes, and Badrinath Roysam. A hybrid 3d watershed algorithm incorporating gradient cues and object models for automatic segmentation of nuclei in confocal image stacks. *Cytometry Part A: the journal of the International Society for Analytical Cytology*, 56(1):23–36, 2003.

[73] Gang Li, Tianming Liu, Ashley Tarokh, Jingxin Nie, Lei Guo, Andrew Mara, Scott Holley, and Stephen TC Wong. 3d cell nuclei segmentation based on gradient flow tracking. *BMC cell biology*, 8(1):40, 2007.

[74] Benjamin Kesler, Guoliang Li, Alexander Thiemicke, Rohit Venkat, and Gregor Neuert. Automated cell boundary and 3d nuclear segmentation of cells in suspension. *Scientific reports*, 9(1):1–9, 2019.

[75] Anne E Carpenter, Thouis R Jones, Michael R Lamprecht, Colin Clarke, In Han Kang, Ola Friman, David A Guertin, Joo Han Chang, Robert A Lindquist, Jason Moffat, et al. Cellprofiler: image analysis software for identifying and quantifying cell phenotypes. *Genome biology*, 7(10):R100, 2006.

[76] Claire McQuin, Allen Goodman, Vasiliy Chernyshev, Lee Kamentsky, Beth A Cimini, Kyle W Karhohs, Minh Doan, Liya Ding, Susanne M Rafelski, Derek Thirstrup, et al. Cellprofiler 3.0: Next-generation image processing for biology. *PLoS biology*, 16(7), 2018.

[77] Christoph Sommer, Christoph N Straehle, Ullrich Koethe, Fred A Hamprecht, et al. Ilastik: Interactive learning and segmentation toolkit. In *ISBI*, volume 2, page 8, 2011.

[78] Yu Toyoshima, Terumasa Tokunaga, Osamu Hirose, Manami Kanamori, Takayuki Teramoto, Moon Sun Jang, Sayuri Kuge, Takeshi Ishihara, Ryo Yoshida, and Yuichi Iino. Accurate automatic detection of densely distributed cell nuclei in 3d space. *PLoS computational biology*, 12(6):e1004970, 2016.

[79] Marlies Verschuuren, Jonas De Vylder, Hannes Catrysse, Joke Robijns, Wilfried Philips, and Winnok H De Vos. Accurate detection of dysmorphic nuclei using dynamic programming and supervised classification. *PLoS One*, 12(1):e0170688, 2017.

[80] Pin Wang, Xianling Hu, Yongming Li, Qianqian Liu, and Xinjian Zhu. Automatic cell nuclei segmentation and classification of breast cancer histopathology images. *Signal Processing*, 122:1–13, 2016.

[81] Siwon Choi, Wei Wang, Alexandrew JS Ribeiro, Agnieszka Kalinowski, Siobhan Q Gregg, Patricia L Opresko, Laura J Niedernhofer, Gustavo K Rohde, and Kris Noel Dahl. Computational image analysis of nuclear morphology associated with various nuclear-specific aging disorders. *Nucleus*, 2(6):570–579, 2011.

[82] Reka Hollandi, Abel Szkalisity, Timea Toth, Ervin Tasnadi, Csaba Molnar, Botond Mathe, Istvan Grexa, Jozsef Molnar, Arpad Balind, Mate Gorbe, et al. nucleaizer: a parameter-free deep learning framework for nucleus segmentation using image style transfer. *Cell Systems*, 10(5):453–458, 2020.

[83] Ashley J Earle, Tyler J Kirby, Gregory R Fedorchak, Philipp Isermann, Jineet Patel, Sushruta Iruvanti, Steven A Moore, Gisèle Bonne, Lori L Wallrath, and Jan Lammerding. Mutant lamins cause nuclear envelope rupture and dna damage in skeletal muscle cells. *Nature Materials*, 19(4):464–473, 2020.

[84] Eloisa Arbustini, Andrea Pilotto, Alessandra Repetto, Maurizia Grasso, Andrea Negri, Marta Diegoli, Carlo Campana, Laura Scelsi, Elisa Baldini, Antonello Gavazzi, et al. Autosomal dominant dilated cardiomyopathy with atrioventricular block: a lamin a/c defect-related disease. *Journal of the American College of Cardiology*, 39(6):981–990, 2002.

[85] Michael V Zaragoza, Lianna Fung, Ember Jensen, Frances Oh, Katherine Cung, Linda A McCarthy, Christine K Tran, Van Hoang, Simin A Hakim, and Anna Grosberg. Exome sequencing identifies a novel lmna splice-site mutation and multigenic heterozygosity of potential modifiers in a family with sick sinus syndrome, dilated cardiomyopathy, and sudden cardiac death. *PLoS One*, 11(5):e0155421, 2016.

[86] Jonathan T Lu, Antoine Muchir, Peter L Nagy, and Howard J Worman. Lmna cardiomyopathy: cell biology and genetics meet clinical medicine. *Disease models & mechanisms*, 4(5):562–568, 2011.

[87] Masahiko Koda, Genzou Takemura, Hideshi Okada, Motoo Kanoh, Rumi Maruyama, Masayasu Esaki, Yiwen Li, Shusaku Miyata, Hiromitsu Kanamori, Longhu Li, et al. Nuclear hypertrophy reflects increased biosynthetic activities in myocytes of human hypertrophic hearts. *Circulation Journal*, 70(6):710–718, 2006.

[88] Indroneal Banerjee, Jianlin Zhang, Thomas Moore-Morris, Emily Pfeiffer, Kyle S Buchholz, Ao Liu, Kunfu Ouyang, Matthew J Stroud, Larry Gerace, Sylvia M Evans, et al. Targeted ablation of nesprin 1 and nesprin 2 from murine myocardium results in cardiomyopathy, altered nuclear morphology and inhibition of the biomechanical gene response. *PLoS Genet*, 10(2):e1004114, 2014.

[89] Erik Laurini, Valentina Martinelli, Thomas Lanzicher, Luca Puzzi, Daniele Borin, Suet Nee Chen, Carlin S Long, Patrice Lee, Luisa Mestroni, Matthew RG Taylor, et al. Biomechanical defects and rescue of cardiomyocytes expressing pathologic nuclear lamins. *Cardiovascular research*, 114(6):846–857, 2018.

[90] Julie Heffler, Parisha P Shah, Patrick Robison, Sai Phyo, Kimberly Veliz, Keita Uchida, Alexey Bogush, Joshua Rhoades, Rajan Jain, and Benjamin L Prosser. A balance between intermediate filaments and microtubules maintains nuclear architecture in the cardiomyocyte. *Circulation research*, 126(3):e10–e26, 2020.

[91] Virginia G Lockard and Sherman Bloom. Trans-cellular desmin-lamin b intermediate filament network in cardiac myocytes. *Journal of molecular and cellular cardiology*, 25 (3):303–309, 1993.

[92] Ben T Grys, Dara S Lo, Nil Sahin, Oren Z Kraus, Quaid Morris, Charles Boone, and Brenda J Andrews. Machine learning and computer vision approaches for phenotypic profiling. *Journal of Cell Biology*, 216(1):65–71, 2017.

[93] JY Tan, CK Chua, KF Leong, KS Chian, WS Leong, and LP Tan. Esophageal tissue engineering: An in-depth review on scaffold design. *Biotechnology and bioengineering*, 109(1):1–15, 2012.

[94] Patrizia Camelliti, Colin R Green, and Peter Kohl. Structural and functional coupling of cardiac myocytes and fibroblasts. In *Cardiovascular Gap Junctions*, volume 42, pages 132–149. Karger Publishers, 2006.

[95] Colby A Souders, Stephanie LK Bowers, and Troy A Baudino. Cardiac fibroblast: the renaissance cell. *Circulation research*, 105(12):1164–1176, 2009.

[96] Malina J Ivey and Michelle D Tallquist. Defining the cardiac fibroblast. *Circulation Journal*, pages CJ–16, 2016.

[97] Sherri M Biendarra-Tiegs, Frank J Secreto, and Timothy J Nelson. Addressing variability and heterogeneity of induced pluripotent stem cell-derived cardiomyocytes. In *Cell Biology and Translational Medicine, Volume 6*, pages 1–29. Springer, 2019.

[98] Stuart Berg, Dominik Kutra, Thorben Kroeger, Christoph N Straehle, Bernhard X Kausler, Carsten Haubold, Martin Schiegg, Janez Ales, Thorsten Beier, Markus Rudy, et al. Ilastik: interactive machine learning for (bio) image analysis. *Nature Methods*, pages 1–7, 2019.

[99] Juan C Caicedo, Sam Cooper, Florian Heigwer, Scott Warchal, Peng Qiu, Csaba Molnar, Aliaksei S Vasilevich, Joseph D Barry, Harmanjit Singh Bansal, Oren Kraus, et al. Data-analysis strategies for image-based cell profiling. *Nature methods*, 14(9):849–863, 2017.

[100] Robert M Haralick, Karthikeyan Shanmugam, and Its' Hak Dinstein. Textural features for image classification. *IEEE Transactions on systems, man, and cybernetics*, (6):610–621, 1973.

[101] Michael Held, Michael HA Schmitz, Bernd Fischer, Thomas Walter, Beate Neumann, Michael H Olma, Matthias Peter, Jan Ellenberg, and Daniel W Gerlich. Cellcognition: time-resolved phenotype annotation in high-throughput live cell imaging. *Nature methods*, 7(9):747, 2010.

[102] Satwik Rajaram, Benjamin Pavie, Lani F Wu, and Steven J Altschuler. Phenoripper: software for rapidly profiling microscopy images. *Nature methods*, 9(7):635–637, 2012.

[103] Jean Ollion, Julien Cochennec, François Loll, Christophe Escudé, and Thomas Boudier. Tango: a generic tool for high-throughput 3d image analysis for studying nuclear organization. *Bioinformatics*, 29(14):1840–1841, 2013.

[104] Mark-Anthony Bray, Shantanu Singh, Han Han, Chadwick T Davis, Blake Borgeson, Cathy Hartland, Maria Kost-Alimova, Sigrun M Gustafsdottir, Christopher C Gibson, and Anne E Carpenter. Cell painting, a high-content image-based assay for morphological profiling using multiplexed fluorescent dyes. *Nature protocols*, 11(9):1757, 2016.

[105] Jie Zhou, Santosh Lamichhane, Gabriella Sterne, Bing Ye, and Hanchuan Peng. Biocat: a pattern recognition platform for customizable biological image classification and annotation. *BMC bioinformatics*, 14(1):1–14, 2013.

[106] Erik Meijering, Anne E Carpenter, Hanchuan Peng, Fred A Hamprecht, and Jean-Christophe Olivo-Marin. Imagining the future of bioimage analysis. *Nature biotechnology*, 34(12):1250–1255, 2016.

[107] Tessa Altair Morris, Jasmine Naik, Kirby Sinclair Fibben, Xiangduo Kong, Tohru Kiyono, Kyoko Yokomori, and Anna Grosberg. Striated myocyte structural integrity: Automated analysis of sarcomeric z-discs. *PLoS computational biology*, 16(3):e1007676, 2020.

[108] Johanna Balogh, Z Li, D Paulin, and A Arner. Desmin filaments influence myofilament spacing and lateral compliance of slow skeletal muscle fibers. *Biophysical journal*, 88 (2):1156–1165, 2005.

[109] Y Soeno, Y Shimada, and T Obinata. Bdm (2, 3-butanedione monoxime), an inhibitor of myosin-actin interaction, suppresses myofibrillogenesis in skeletal muscle cells in culture. *Cell and tissue research*, 295(2):307–316, 1999.

[110] Anant Chopra, Akash Patel, Adrian C Shieh, Paul A Janmey, and J Yasha Kresh. α-catenin localization and sarcomere self-organization on n-cadherin adhesive patterns are myocyte contractility driven. *PloS one*, 7(10):e47592, 2012.

[111] Sean P Sheehy, Anna Grosberg, Pu Qin, David J Behm, John P Ferrier, Mackenzie A Eagleson, Alexander P Nesmith, David Krull, James G Falls, Patrick H Campbell, et al. Toward improved myocardial maturity in an organ-on-chip platform with immature cardiac myocytes. *Experimental Biology and Medicine*, 242(17):1643–1656, 2017.

[112] Ashutosh Agarwal, Yohan Farouz, Alexander Peyton Nesmith, Leila F Deravi, Megan Laura McCain, and Kevin Kit Parker. Micropatterning alginate substrates for in vitro cardiovascular muscle on a chip. *Advanced functional materials*, 23(30): 3738–3746, 2013.

[113] Aiping Du, Jean M Sanger, and Joseph W Sanger. Cardiac myofibrillogenesis inside intact embryonic hearts. *Developmental biology*, 318(2):236–246, 2008.

[114] Jennifer White, Marietta V Barro, Helen P Makarenkova, Joseph W Sanger, and Jean M Sanger. Localization of sarcomeric proteins during myofibril assembly in cultured mouse primary skeletal myotubes. *The Anatomical Record*, 297(9):1571–1584, 2014.

[115] Punam K Saha, Gunilla Borgefors, and Gabriella Sanniti di Baja. A survey on skeletonization algorithms and their applications. *Pattern Recognition Letters*, 76:3–12, 2016.

[116] John Canny. A computational approach to edge detection. *IEEE Transactions on pattern analysis and machine intelligence*, (6):679–698, 1986.

[117] Raman Maini and Himanshu Aggarwal. Study and comparison of various image edge detection techniques. *International journal of image processing (IJIP)*, 3(1):1–11, 2009.

[118] John L Tan, Wendy Liu, Celeste M Nelson, Srivatsan Raghavan, and Christopher S Chen. Simple approach to micropattern cells on common culture substrates by tuning substrate wettability. *Tissue engineering*, 10(5-6):865–872, 2004.

[119] K Shiomi, T Kiyono, K Okamura, M Uezumi, Yi Goto, S Yasumoto, S Shimizu, and N Hashimoto. CDK4 and cyclin D1 allow human myogenic cells to recapture growth property without compromising differentiation potential. *Gene therapy*, 18(9):857, 2011.

[120] Weihua Zeng, Shan Jiang, Xiangduo Kong, Nicole El-Ali, Alexander R Ball Jr, Christopher I-Hsing Ma, Naohiro Hashimoto, Kyoko Yokomori, and Ali Mortazavi. Single-nucleus RNA-seq of differentiating human myoblasts reveals the extent of fate heterogeneity. *Nucleic acids research*, 44(21):e158–e158, 2016.

[121] TA Morris, J Naik, KS Fibbin, X Kong, T Kiyono, K Yokomori, and A Grosberg. Data from: Striated myocyte structural integrity: automated analysis of sarcomeric z-discs. Dryad Digital Repository. `https://doi.org/10.7280/D12Q2X`, 2020.

[122] Nils E Persson, Michael A McBride, Martha A Grover, and Elsa Reichmanis. Automated analysis of orientational order in images of fibrillar materials. *Chemistry of Materials*, 29(1):3–14, 2016.

[123] Joachim Weickert. Coherence-enhancing diffusion filtering. *International journal of computer vision*, 31(2-3):111–127, 1999.

[124] Pietro Perona and Jitendra Malik. Scale-space and edge detection using anisotropic diffusion. *IEEE Transactions on pattern analysis and machine intelligence*, 12(7):629–639, 1990.

[125] D Kroon and Cornelis H Slump. Coherence filtering to enhance the mandibular canal in cone-beam CT data. In *IEEE-EMBS Benelux Chapter Symposium*, volume 11, pages 40–41, 2009.

[126] Seong-Whan Lee, Louisa Lam, and Ching Y Suen. A systematic evaluation of skeletonization algorithms. *International Journal of Pattern Recognition and Artificial Intelligence*, 7(05):1203–1225, 1993.

[127] Jean Serra and Pierre Soille. *Mathematical morphology and its applications to image processing*, volume 2. Springer Science & Business Media, 2012.

[128] Shimon D Yanowitz and Alfred M Bruckstein. A new method for image segmentation. *Computer Vision, Graphics, and Image Processing*, 46(1):82–95, 1989.

[129] Lin Hong, Yifei Wan, and Anil Jain. Fingerprint image enhancement: Algorithm and performance evaluation. *IEEE transactions on pattern analysis and machine intelligence*, 20(8):777–789, 1998.

[130] P. D. Kovesi. MATLAB and Octave functions for computer vision and image processing, 2000. Available from: <http://www.peterkovesi.com/matlabfns/>.

[131] A. Umeno, H. Kotani, M. Iwasaka, and S. Ueno. Quantification of adherent cell orientation and morphology under strong magnetic fields. *IEEE Transactions on Magnetics*, 37(4):2909–2911, July 2001. ISSN 0018-9464.

[132] Rebecca L Carrier, Maria Papadaki, Maria Rupnick, Frederick J Schoen, Nenad Bursac, Robert Langer, Lisa E Freed, and Gordana Vunjak-Novakovic. Cardiac tissue engineering: cell seeding, cultivation parameters, and tissue construct characterization. *Biotechnology and bioengineering*, 64(5):580–589, 1999.

[133] Peter H Backx, Wei-Dong Gao, Michelle D Azan-Backx, and Eduardo Marban. Mechanism of force inhibition by 2, 3-butanedione monoxime in rat cardiac muscle: roles of [Ca2+] i and cross-bridge kinetics. *The Journal of physiology*, 476(3):487–500, 1994.

[134] Andrea Leonard, Alessandro Bertero, Joseph D Powers, Kevin M Beussman, Shiv Bhandari, Michael Regnier, Charles E Murry, and Nathan J Sniadecki. Afterload promotes maturation of human induced pluripotent stem cell derived cardiomyocytes in engineered heart tissues. *Journal of molecular and cellular cardiology*, 118:147–158, 2018.

[135] Marita Lynn Rodriguez, Kevin M Beussman, Katherine S Chun, Melissa S Walzer, Xiulan Yang, Charles E Murry, and Nathan J Sniadecki. Substrate stiffness, cell anisotropy, and cell-cell contact contribute to enhanced structural and calcium handling properties of human embryonic stem cell derived cardiomyocytes. *ACS Biomaterials Science & Engineering*, 2019.

[136] Sean P Sheehy, Anna Grosberg, and Kevin Kit Parker. The contribution of cellular mechanotransduction to cardiomyocyte form and function. *Biomechanics and modeling in mechanobiology*, 11(8):1227–1239, 2012.

[137] Scott D Lundy, Wei-Zhong Zhu, Michael Regnier, and Michael A Laflamme. Structural and functional maturation of cardiomyocytes derived from human pluripotent stem cells. *Stem cells and development*, 22(14):1991–2002, 2013.

[138] Nazha Hamdani, Viola Kooij, Sabine van Dijk, Daphne Merkus, Walter J Paulus, Cris dos Remedios, Dirk J Duncker, Ger JM Stienen, and Jolanda van der Velden. Sarcomeric dysfunction in heart failure. *Cardiovascular research*, 77(4):649–658, 2007.

[139] Pavel Mrázek and Mirko Navara. Selection of optimal stopping time for nonlinear diffusion filtering. *International Journal of Computer Vision*, 52(2-3):189–203, 2003.

[140] Chourmouzios Tsiotsios and Maria Petrou. On the choice of the parameters for anisotropic diffusion in image processing. *Pattern recognition*, 46(5):1369–1381, 2013.

[141] Tariq M Khan, Mohammad AU Khan, Yinan Kong, and Omar Kittaneh. Stopping criterion for linear anisotropic image diffusion: a fingerprint image enhancement case. *EURASIP Journal on Image and Video Processing*, 2016(1):6, 2016.

[142] Arun Sharma, Christopher N Toepfer, Manuel Schmid, Amanda C Garfinkel, and Christine E Seidman. Differentiation and contractile analysis of gfp-sarcomere reporter hipsc-cardiomyocytes. *Current protocols in human genetics*, 96(1):21–12, 2018.

[143] Stewart I Head. Branched fibres in old dystrophic mdx muscle are associated with mechanical weakening of the sarcolemma, abnormal ca2+ transients and a breakdown of ca2+ homeostasis during fatigue. *Experimental Physiology*, 95(5):641–656, 2010.

[144] O Friedrich, M Both, C Weber, S Schürmann, MDH Teichmann, F Von Wegner, RHA Fink, M Vogel, JS Chamberlain, and C Garbe. Microarchitecture is severely compromised but motor protein function is preserved in dystrophic mdx skeletal muscle. *Biophysical journal*, 98(4):606–616, 2010.

[145] Richard M Lovering, Luke Michaelson, and Christopher W Ward. Malformed mdx myofibers have normal cytoskeletal architecture yet altered ec coupling and stress-induced ca2+ signaling. *American Journal of Physiology-Cell Physiology*, 297(3):C571–C580, 2009.

[146] Andreas Buttgereit, Cornelia Weber, Christoph S Garbe, and Oliver Friedrich. From chaos to split-ups–shg microscopy reveals a specific remodelling mechanism in ageing dystrophic muscle. *The Journal of pathology*, 229(3):477–485, 2013.

[147] Stefanie Diermeier, Andreas Buttgereit, Sebastian Schuermann, Lilli Winter, Hongyang Xu, Robyn M Murphy, Christoph S Clemen, Rolf Schroeder, and Oliver Friedrich. Preaged remodeling of myofibrillar cytoarchitecture in skeletal muscle expressing r349p mutant desmin. *Neurobiology of aging*, 58:77–87, 2017.

[148] Nobuyuki Otsu. A threshold selection method from gray-level histograms. *IEEE transactions on systems, man, and cybernetics*, 9(1):62–66, 1979.

[149] Kazutoshi Takahashi and Shinya Yamanaka. Induction of pluripotent stem cells from mouse embryonic and adult fibroblast cultures by defined factors. *cell*, 126(4):663–676, 2006.

[150] Kazutoshi Takahashi, Koji Tanabe, Mari Ohnuki, Megumi Narita, Tomoko Ichisaka, Kiichiro Tomoda, and Shinya Yamanaka. Induction of pluripotent stem cells from adult human fibroblasts by defined factors. *cell*, 131(5):861–872, 2007.

[151] Alec ST Smith, Jesse Macadangdang, Winnie Leung, Michael A Laflamme, and Deok-Ho Kim. Human ipsc-derived cardiomyocytes and tissue engineering strategies for disease modeling and drug screening. *Biotechnology advances*, 35(1):77–94, 2017.

[152] Kiran Musunuru, Farah Sheikh, Rajat M Gupta, Steven R Houser, Kevin O Maher, David J Milan, Andre Terzic, and Joseph C Wu. Induced pluripotent stem cells for cardiovascular disease modeling and precision medicine: a scientific statement from the american heart association. *Circulation: Genomic and Precision Medicine*, 11(1): e000043, 2018.

[153] Yoshinori Yoshida and Shinya Yamanaka. Induced pluripotent stem cells 10 years later: for cardiac applications. *Circulation research*, 120(12):1958–1968, 2017.

[154] Alessandra Moretti, Milena Bellin, Andrea Welling, Christian Billy Jung, Jason T Lam, Lorenz Bott-Flügel, Tatjana Dorn, Alexander Goedel, Christian Höhnke, Franz Hofmann, et al. Patient-specific induced pluripotent stem-cell models for long-qt syndrome. *New England Journal of Medicine*, 363(15):1397–1409, 2010.

[155] Masayuki Yazawa, Brian Hsueh, Xiaolin Jia, Anca M Pasca, Jonathan A Bernstein, Joachim Hallmayer, and Ricardo E Dolmetsch. Using induced pluripotent stem cells to investigate cardiac phenotypes in timothy syndrome. *Nature*, 471(7337):230–234, 2011.

[156] Saranya P Wyles, Xing Li, Sybil C Hrstka, Santiago Reyes, Saji Oommen, Rosanna Beraldi, Jessica Edwards, Andre Terzic, Timothy M Olson, and Timothy J Nelson. Modeling structural and functional deficiencies of rbm20 familial dilated cardiomyopathy using human induced pluripotent stem cells. *Human molecular genetics*, 25(2): 254–265, 2016.

[157] Christian B Jung, Alessandra Moretti, Michael Mederos y Schnitzler, Laura Iop, Ursula Storch, Milena Bellin, Tatjana Dorn, Sandra Ruppenthal, Sarah Pfeiffer, Alexander Goedel, et al. Dantrolene rescues arrhythmogenic ryr2 defect in a patient-specific stem cell model of catecholaminergic polymorphic ventricular tachycardia. *EMBO molecular medicine*, 4(3):180–191, 2012.

[158] Sybil CL Hrstka, Xing Li, Timothy J Nelson, and Wanek Program Genetics Pipeline Group. Notch1-dependent nitric oxide signaling deficiency in hypoplastic left heart syndrome revealed through patient-specific phenotypes detected in bioengineered cardiogenesis. *Stem Cells*, 35(4):1106–1119, 2017.

[159] Gaetano J Scuderi and Jonathan Butcher. Naturally engineered maturation of cardiomyocytes. *Frontiers in cell and developmental biology*, 5:50, 2017.

[160] Chengyi Tu, Benjamin S Chao, and Joseph C Wu. Strategies for improving the maturity of human induced pluripotent stem cell-derived cardiomyocytes, 2018.

[161] Karel Zuiderveld. Contrast limited adaptive histogram equalization. In *Graphics gems IV*, pages 474–485. Academic Press Professional, Inc., 1994.

[162] Olivier Salvado. ordfilt3d: Perform 3-d order-statistic filtering on 26 neighbors. MATLAB Central File Exchange, 2020.

[163] Calvin R Maurer, Rensheng Qi, and Vijay Raghavan. A linear time algorithm for computing exact euclidean distance transforms of binary images in arbitrary dimensions. *IEEE Transactions on Pattern Analysis and Machine Intelligence*, 25(2):265–270, 2003.

[164] Azriel Rosenfeld and John L Pfaltz. Sequential operations in digital picture processing. *Journal of the ACM (JACM)*, 13(4):471–494, 1966.

[165] David W Paglieroni. Distance transforms: Properties and machine vision applications. *CVGIP: Graphical models and image processing*, 54(1):56–74, 1992.

[166] Fernand Meyer. Topographic distance and watershed lines. *Signal processing*, 38(1): 113–125, 1994.

[167] Jianxu Chen, Liya Ding, Matheus P Viana, Melissa C Hendershott, Ruian Yang, Irina A Mueller, and Susanne M Rafelski. The allen cell structure segmenter: a new open source toolkit for segmenting 3d intracellular structures in fluorescence microscopy images. *bioRxiv*, page 491035, 2018.

[168] Paola Spitalieri, Rosa V Talarico, Silvia Caioli, Michela Murdocca, Annalucia Serafino, Marco Girasole, Simone Dinarelli, Giovanni Longo, Sabina Pucci, Annalisa Botta, et al. Modelling the pathogenesis of myotonic dystrophy type 1 cardiac phenotype through human ipsc-derived cardiomyocytes. *Journal of molecular and cellular cardiology*, 118: 95–109, 2018.

[169] HW Vliegen, A Van der Laarse, CJ Cornelisse, and F Eulderink. Myocardial changes in pressure overload-induced left ventricular hypertrophy: A study on tissue composition, polyploidization and multinucleation. *European heart journal*, 12(4):488–494, 1991.

[170] Richard A Lasher, Aric Q Pahnke, Jeffrey M Johnson, Frank B Sachse, and Robert W Hitchcock. Electrical stimulation directs engineered cardiac tissue to an age-matched native phenotype. *Journal of tissue engineering*, 3(1):2041731412455354, 2012.

[171] Carlo Alberto Beltrami, Nicoletta Finato, Maurizio Rocco, Giorgio A Feruglio, Cesare Puricelli, Elena Cigola, Edmund H Sonnenblick, Giorgio Olivetti, and Piero Anversa. The cellular basis of dilated cardiomyopathy in humans. *Journal of molecular and cellular cardiology*, 27(1):291–305, 1995.

[172] Patrizia Camelliti, Gerard P Devlin, Kenneth G Matthews, Peter Kohl, and Colin R Green. Spatially and temporally distinct expression of fibroblast connexins after sheep ventricular infarction. *Cardiovascular research*, 62(2):415–425, 2004.

[173] Claudio Humeres and Nikolaos G Frangogiannis. Fibroblasts in the infarcted, remodeling, and failing heart. *JACC: Basic to Translational Science*, 4(3):449–467, 2019.

[174] Wei Chen and Nikolaos G Frangogiannis. Fibroblasts in post-infarction inflammation and cardiac repair. *Biochimica et Biophysica Acta (BBA)-Molecular Cell Research*, 1833(4):945–953, 2013.

[175] Ronald B Driesen, Fons K Verheyen, Petra Dijkstra, Fred Thoné, Jack P Cleutjens, Marie-Hélène Lenders, Frans CS Ramaekers, and Marcel Borgers. Structural remodelling of cardiomyocytes in the border zone of infarcted rabbit heart. *Molecular and cellular biochemistry*, 302(1):225–232, 2007.

[176] Eeva Palojoki, Antti Saraste, Anders Eriksson, Kari Pulkki, Markku Kallajoki, Liisa-Maria Voipio-Pulkki, and Ilkka Tikkanen. Cardiomyocyte apoptosis and ventricular remodeling after myocardial infarction in rats. *American Journal of Physiology-Heart and Circulatory Physiology*, 280(6):H2726–H2731, 2001.

[177] Susan Van Noorden, EGJ Olsen, and AGE Pearse. Hypertrophic obstructive cardiomyopathy, a histological, histochemical, and ultrastructural study of biopsy material. *Cardiovascular Research*, 5(1):118–131, 1971.

[178] VICTOR J FERRANS, ANDREW G MORROW, and WILLIAM C ROBERTS. Myocardial ultrastructure in idiopathic hypertrophic subaortic stenosis: a study of operatively excised left ventricular outflow tract muscle in 14 patients. *Circulation*, 45(4): 769–792, 1972.

[179] BARRY J Maron, THOMAS J Anan, and WILLIAM C Roberts. Quantitative analysis of the distribution of cardiac muscle cell disorganization in the left ventricular wall of patients with hypertrophic cardiomyopathy. *Circulation*, 63(4):882–894, 1981.

[180] Anatole Chessel. An overview of data science uses in bioimage informatics. *Methods*, 115:110–118, 2017.

[181] Christoph Sommer and Daniel W Gerlich. Machine learning in cell biology–teaching computers to recognize phenotypes. *Journal of cell science*, 126(24):5529–5539, 2013.

[182] Radhakrishna Achanta, Appu Shaji, Kevin Smith, Aurelien Lucchi, Pascal Fua, and Sabine Süsstrunk. Slic superpixels compared to state-of-the-art superpixel methods. *IEEE transactions on pattern analysis and machine intelligence*, 34(11):2274–2282, 2012.

[183] Uwe Schmidt, Martin Weigert, Coleman Broaddus, and Gene Myers. Cell detection with star-convex polygons. In *International Conference on Medical Image Computing and Computer-Assisted Intervention*, pages 265–273. Springer, 2018.

[184] Gerhard Meier and Alfred Saupe. Dielectric relaxation in nematic liquid crystals. *Molecular Crystals and Liquid Crystals*, 1(4):515–525, 1966.

[185] Paul M Chaikin, Tom C Lubensky, and Thomas A Witten. *Principles of condensed matter physics*, volume 10. Cambridge university press Cambridge, 1995.

[186] Kaytlyn A Gerbin, Tanya Grancharova, Rory Donovan-Maiye, Melissa C Hendershott, Jackson Brown, Stephanie Q Dinh, Jamie L Gehring, Matthew Hirano, Gregory R Johnson, Aditya Nath, et al. Cell states beyond transcriptomics: integrating structural organization and gene expression in hipsc-derived cardiomyocytes. *bioRxiv*, 2020.

[187] Robert M Haralick. Statistical and structural approaches to texture. *Proceedings of the IEEE*, 67(5):786–804, 1979.

[188] Meghan K Driscoll, Jason L Albanese, Zheng-Mei Xiong, Mitch Mailman, Wolfgang Losert, and Kan Cao. Automated image analysis of nuclear shape: What can we learn from a prematurely aged cell? *Aging (Albany NY)*, 4(2):119, 2012.

[189] Robert Mandelkow, Denis Guembel, Hannes Ahrend, Anne Kaul, Uwe Zimmermann, Martin Burchardt, and Matthias B Stope. Detection and quantification of nuclear morphology changes in apoptotic cells by fluorescence microscopy and subsequent analysis of visualized fluorescent signals. *Anticancer research*, 37(5):2239–2244, 2017.

[190] Alexandra M Greiner, Hao Chen, Joachim P Spatz, and Ralf Kemkemer. Cyclic tensile strain controls cell shape and directs actin stress fiber formation and focal adhesion alignment in spreading cells. *PloS one*, 8(10):e77328, 2013.

[191] A Zemel, F Rehfeldt, AEX Brown, DE Discher, and SA Safran. Optimal matrix rigidity for stress-fibre polarization in stem cells. *Nature physics*, 6(6):468–473, 2010.

[192] Alexander Bershadsky, Michael Kozlov, and Benjamin Geiger. Adhesion-mediated mechanosensitivity: a time to experiment, and a time to theorize. *Current opinion in cell biology*, 18(5):472–481, 2006.

[193] Toshiaki Iba and Bauer E Sumpio. Morphological response of human endothelial cells subjected to cyclic strain in vitro. *Microvascular research*, 42(3):245–254, 1991.

[194] J Pablo Rodríguez, Mauricio González, Susana Ríos, and Verónica Cambiazo. Cytoskeletal organization of human mesenchymal stem cells (msc) changes during their osteogenic differentiation. *Journal of cellular biochemistry*, 93(4):721–731, 2004.

[195] Albert Cardona and Pavel Tomancak. Current challenges in open-source bioimage informatics. *Nature methods*, 9(7):661–665, 2012.

[196] Johannes Schindelin, Ignacio Arganda-Carreras, Erwin Frise, Verena Kaynig, Mark Longair, Tobias Pietzsch, Stephan Preibisch, Curtis Rueden, Stephan Saalfeld, Benjamin Schmid, et al. Fiji: an open-source platform for biological-image analysis. *Nature methods*, 9(7):676–682, 2012.

[197] Curtis T Rueden, Johannes Schindelin, Mark C Hiner, Barry E DeZonia, Alison E Walter, Ellen T Arena, and Kevin W Eliceiri. Imagej2: Imagej for the next generation of scientific image data. *BMC bioinformatics*, 18(1):1–26, 2017.

[198] Caroline A Schneider, Wayne S Rasband, and Kevin W Eliceiri. Nih image to imagej: 25 years of image analysis. *Nature methods*, 9(7):671–675, 2012.

[199] Lee Kamentsky, Thouis R Jones, Adam Fraser, Mark-Anthony Bray, David J Logan, Katherine L Madden, Vebjorn Ljosa, Curtis Rueden, Kevin W Eliceiri, and Anne E Carpenter. Improved structure, function and compatibility for cellprofiler: modular high-throughput image analysis software. *Bioinformatics*, 27(8):1179–1180, 2011.

APPENDIX A

Supporting Information for *Striated myocyte structural integrity: Automated analysis of sarcomeric z-discs*
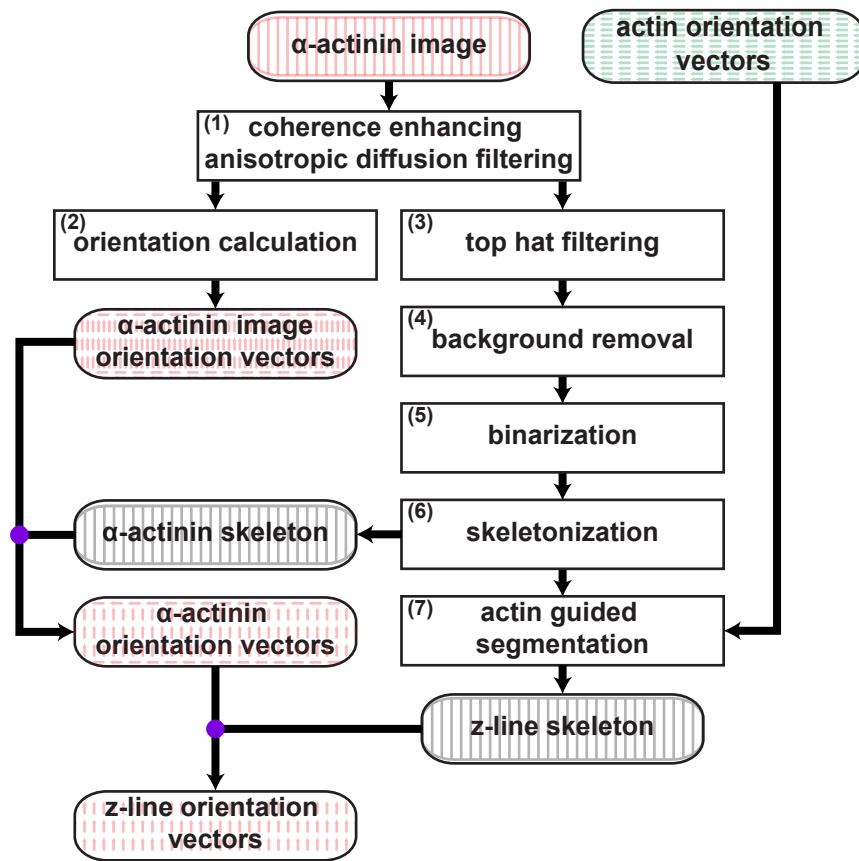

Figure A.1: **Image analysis workflow.** Squared boxed text indicates an image analysis step in `ZlineDetection`. Rounded boxed text indicates an image or matrix, where binary skeletons are shaded gray, matrices containing information about α-actinin stained images are shaded red, and matrices containing information about actin stained images are shaded green. Purple circles indicate matrix multiplication. On a computer with 32 GB of RAM, `ZlineDetection` took ~30 s to analyze a 1024 x 1344 image.

Table A.1: **Description of parameters used by `ZlineDetection`.** Column 1 is the stage of analysis at which a parameter is used, followed by its description in column 2. The third column is the value of the parameters used for analysis of the images, which had the resolution ~6 pixels/µm.

| Analysis Stage	Description	Value
Initialization	Pixel to micron conversion	6.22 pixels/µm
Diffusion Filtering	Diffusion time step	0.15 s
Diffusion Filtering	Standard deviation of Gaussian smoothing before calculation of the image Hessian	1 pixel
Diffusion Filtering	Standard deviation of Gaussian smoothing of the image Hessian	1.4 pixels
Diffusion Filtering	Total diffusion time; Sets number of iterations	1.5 s (11 iterations)
Top Hat Filtering	Radius of the flat disk-shaped structuring element used for the top hat filter	3 pixels ($_\sim$0.5 µm)
Background Removal	Size of blocks to break image into	15 pixels ($_\sim$2.5 µm)
Background Removal	Size of blocks considered noise in the condensed image	8 pixels ($_\sim$25 µm)
Background Removal	Standard deviation of Gaussian smoothing to perform on image	1 pixel
Binarization	Size of small objects to be removed in the binarized image	8 pixels^2 (0.2 µm^2)
Skeletonization	Minimum branch size to be included in analysis	4 pixels
Actin Orientation Calculation	Sigma of the Gaussian weighting used to sum the gradient moments	3 pixels
Actin Orientation Calculation	Sigma of the derivative of Gaussian used to compute image gradients	1 pixel
Actin Orientation Calculation	Size of Gaussian filter kernel to perform on actin image	25 pixels
Actin Orientation Calculation	Sigma of the Gaussian used to smooth the final orientation vector field	3 pixels
Actin Orientation Calculation	Minimum reliability of actin orientation vectors	0.5
Actin Orientation Calculation	Standard deviation of Gaussian smoothing to perform on actin image	3 pixels
Actin Guided Segmentation	Minimum angle between α-actinin and local actin orientation for pixels to be considered perpendicular	0.7 ($>_\sim$45°)
Actin Guided Segmentation	Size of local actin orientation	30 pixels ($_\sim$5 µm)
Continuous Z-line Length	Maximum angle between pixels to be considered parallel and therefore continuous	0.9 ($<_\sim$25°)
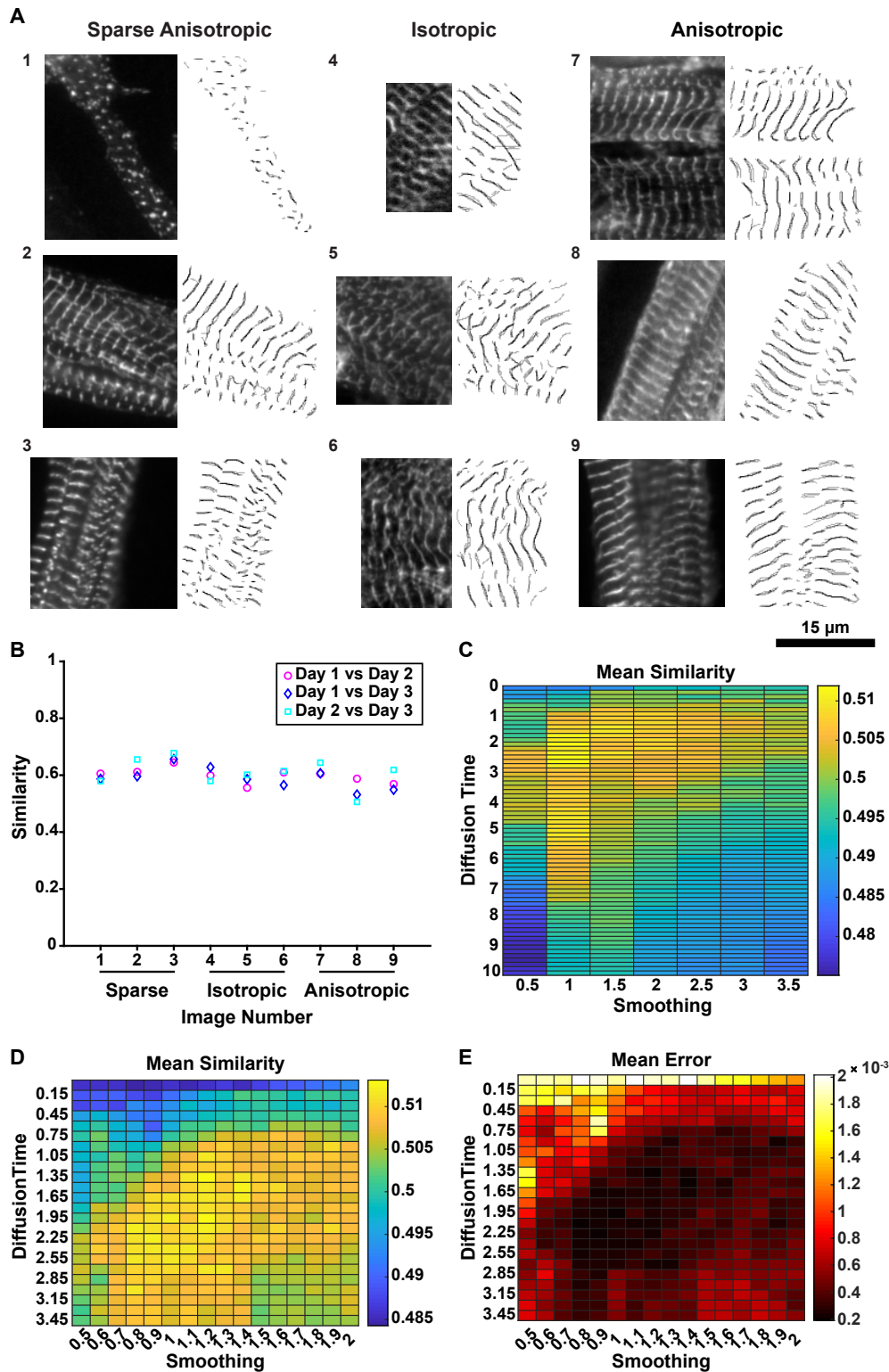
Figure A.2: **Selection of diffusion filter parameters. A**, Sections of anisotropic, isotropic, and sparse anisotropic tissues with manually traced z-lines, which was done three times. **B**, Similarity between the three different manual traces of z-lines. **C**, Average similarity for each set of diffusion filtering parameters. **D**, Average similarity for a more refined range of diffusion filtering parameters. **E**, Error for refined range of diffusion filtering parameters (Eq 2.1).
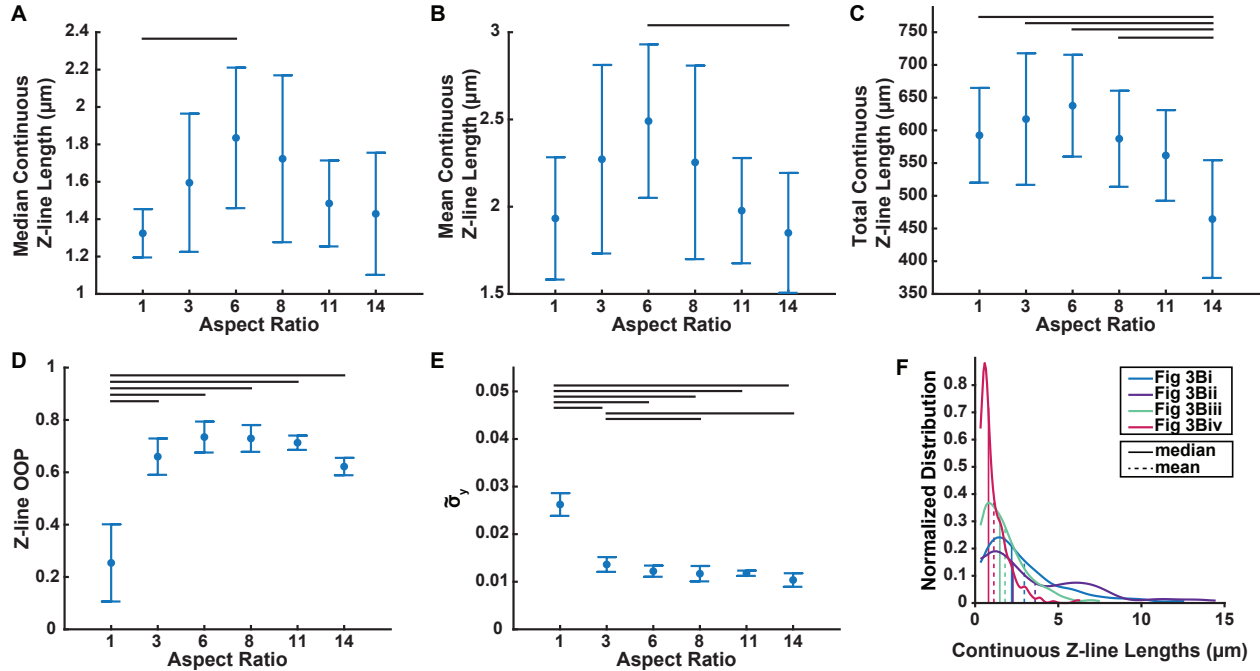
Figure A.3: **Z-line tissue metrics by aspect ratio.** For the good cells of each aspect ratio, the mean and standard deviation are shown for the median continuous z-line length **(A)**, mean continuous z-line length **(B)**, total continuous z-line length **(C)**, z-line OOP **(D)**, and the estimated force along the axis perpendicular to principle axis **(E)**. **F**, Normalized distribution of continuous z-line lengths for the representative cells in Fig 2.3. Groups were compared using ANOVA with Tukey's test p <0.05 (black horizontal bars above data).
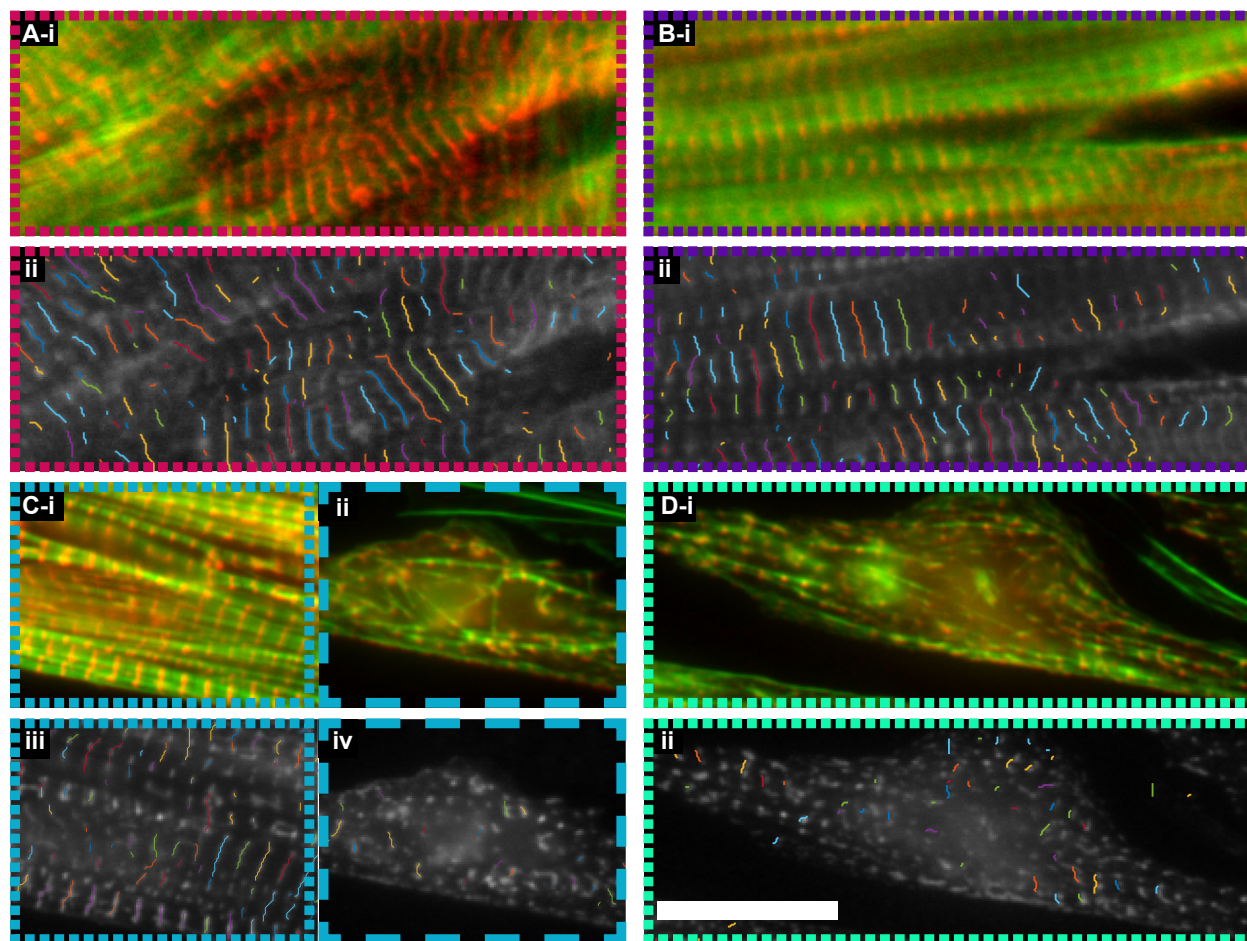
Figure A.4: **Continuous z-lines plotted on tissue segments.** Sections of cardiac tissue shown in Fig 2.4A-D stained for actin (green) and α-actinin (red) on a uniform layer of FN **(Ai)**, FN in lines **(Bi)**, FN in lines with sparsely seeded cardiomyocytes **(Ci)**, and FN in lines with cardiomyocytes treated with BDM **(Di)** and their corresponding continuous z-lines **(A-Dii)**. Scale bar: 15 µm
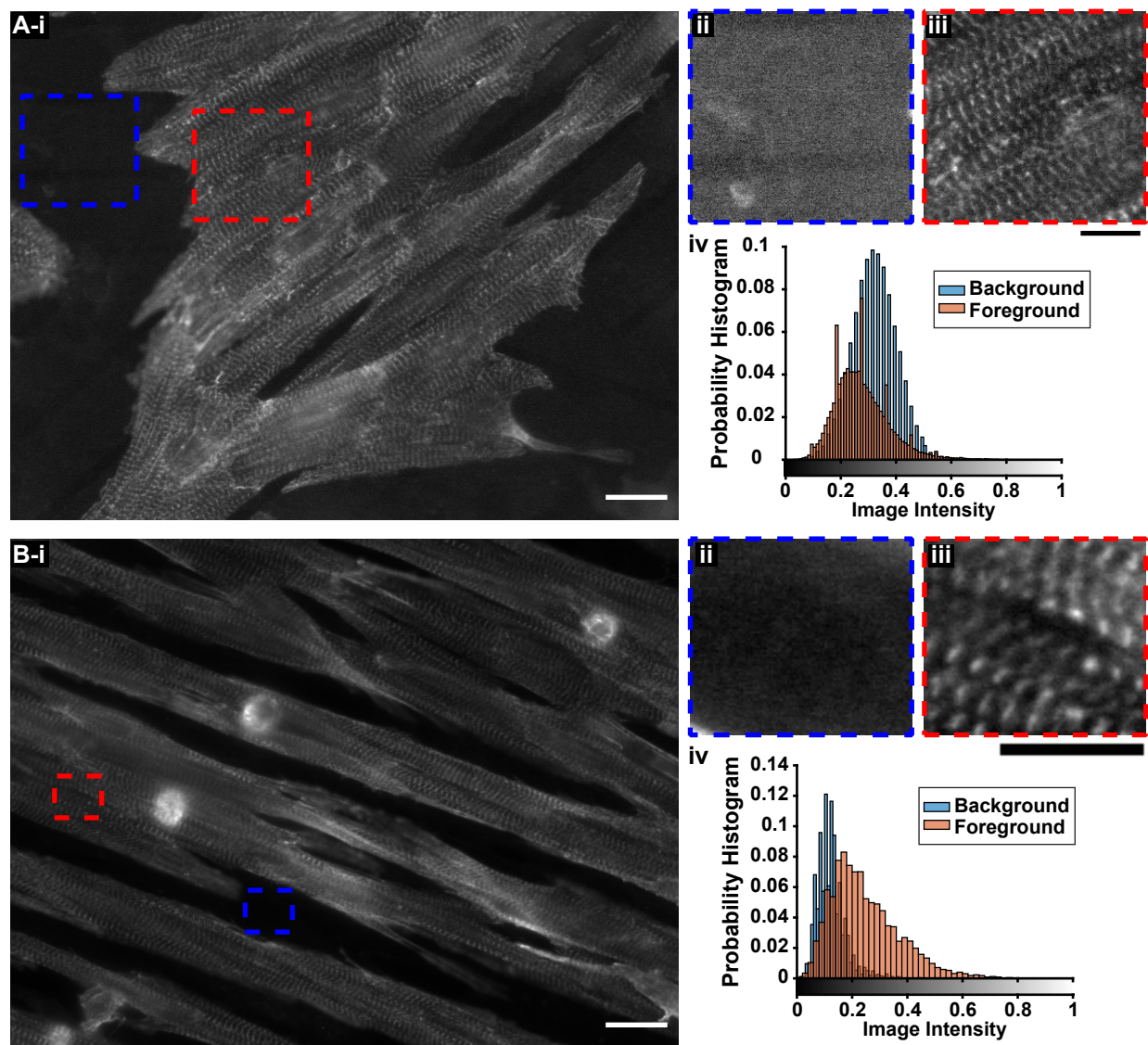
Figure A.5: **Examples of good and poor imaging. A**, α-actinin stained image of poor imaging quality. **B**, Example of good imaging quality. For both **A** and **B**, the background **(i)**, foreground **(ii)**, and distribution of intensities **(iii)** are shown. Scale bars: **(A-B i)** 20 µm; **(A-B ii-iii)** 10 µm.
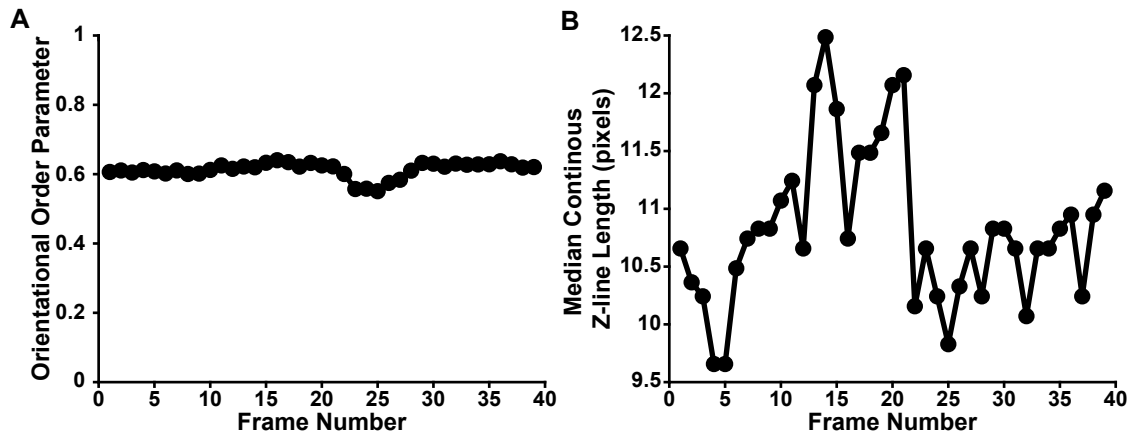
Figure A.6: **Analysis of beating cardiomyocyte.** Results of analyzing titin-GFP sarcomere reporter human induced pluripotent stem cell-derived cardiomyocyte published by Sharma et al.[142]. **(A)** Orientational order parameter and **(B)** median continuous z-line length in pixels as a function of frame number. As expected, the OOP was relatively constant throughout the contraction, while the median continuous z-line length varied due to non-synchronous contractions of neighboring myofibrils.